

Electronic Thesis and Dissertation Repository

12-9-2015 12:00 AM

Morphological, Structural and Spectral Mapping of the Central Uplifts of the Alga and Verlaine Craters, Mars

Bianca D'Aoust
The University of Western Ontario

Supervisor
Dr. Gordon Osinski
The University of Western Ontario Joint Supervisor
Dr. Livio Tornabene
The University of Western Ontario

Graduate Program in Geology
A thesis submitted in partial fulfillment of the requirements for the degree in Master of Science
© Bianca D'Aoust 2015

Follow this and additional works at: <https://ir.lib.uwo.ca/etd>



Part of the [Geology Commons](#)

Recommended Citation

D'Aoust, Bianca, "Morphological, Structural and Spectral Mapping of the Central Uplifts of the Alga and Verlaine Craters, Mars" (2015). *Electronic Thesis and Dissertation Repository*. 3441.
<https://ir.lib.uwo.ca/etd/3441>

This Dissertation/Thesis is brought to you for free and open access by Scholarship@Western. It has been accepted for inclusion in Electronic Thesis and Dissertation Repository by an authorized administrator of Scholarship@Western. For more information, please contact wlsadmin@uwo.ca.

MORPHOLOGICAL, STRUCTURAL, AND SPECTRAL MAPPING OF THE CENTRAL
UPLIFTS OF THE ALGA AND VERLAINE CRATERS, MARS

(Thesis format: Integrated Article)

by

Bianca D'Aoust

Graduate Program in Geology, Specialization in Planetary Science

A thesis submitted in partial fulfillment
of the requirements for the degree of
Master of Science

The School of Graduate and Postdoctoral Studies
The University of Western Ontario
London, Ontario, Canada

© Bianca D'Aoust 2015

Abstract

Impact cratering is a ubiquitous geological process that has shaped planetary bodies of the Solar System and beyond. While the impact cratering record on Earth has been poorly preserved, the Martian surface is characterized by a very old and cratered terrain. Central uplifts within complex impact craters are of particular interest as they expose deep-seated material, some of which may correspond to samples of the early Martian crust. Central uplift formation is, however, still a poorly understood geological process. This research investigated the origin of the exposed bedrock in the central uplifts of two Martian complex craters as well as the emplacement, distribution, and extent of allochthonous crater-fill deposits. This research entailed detailed decametre- to metre-scale mapping of morphological and structural observations with compositional analysis. Two complex craters located within Noachian-aged terrains, Alga (333.3 °E, 24.3 °S; ~19 km in diameter) and Verlaine (64.1 °E, -9.2 °S; ~39 km in diameter) were selected for this study. The exposed massive and fractured bedrock (MFB) in Alga is enriched in olivine and low-calcium pyroxene. Verlaine is characterized by MFB pervasively altered throughout the uplift and mainly enriched in olivine, with some isolated occurrences of alteration to Fe/Mg-rich clays. Both central uplifts are characterized by a diversity of potential impact melt-bearing lithologies that cover a major proportion of the uplifts. Structural mapping revealed that lineaments are oriented radially and concentrically, which corroborate structural assessments of terrestrial impact structures.

Keywords

Mars, Impact cratering, Complex crater, Central uplift, Geological mapping, Spectral analysis

Acknowledgments

Very special acknowledgement to the Richard J. Schmeelk Canada Fellowship for their financial support for the duration of my M.Sc. and Mr. Stephen Dopp, President, for providing me with precious guidance and advice toward my future career plans.

I would like to thank my M.Sc. advisors, Dr. Livio Tornabene and Dr. Gordon Osinski for guiding and supporting me during the past two years and feel immensely privileged to have been a team member of the Centre for Planetary Science and Exploration (CPSX) at Western University. Dr. Livio Tornabene's prior involvement with Mars missions and his expertise of Martian impact cratering made him an excellent mentor and instructor for this project. As my primary resource for getting my science questions answered, I am very grateful for the time and effort Livio dedicated to me towards planetary remote sensing knowledge transfer. Our many insightful discussions, his advice, feedback and comments have been valuable and instrumental in helping me write out my conference papers and thesis, and he has thought me an academic rigor that I have put into practice.

I am especially grateful to Dr. Osinski for helping direct my research. I appreciated his expertise and knowledge of impact cratering process. Thanks to Dr. Osinski, I was able to attend and participate in numerous conferences and fieldwork. Collaborating with Dr. Osinski and Dr. Tornabene for this project was infinitely rewarding. My thanks to Richard Grieve for his expertise and advice on impact cratering and for taking the time to look into the research I conducted. My thanks to Trent Hare from the U.S. Geological Survey for his help in GIS and planetary remote sensing. Furthermore, I would like to thank PhD student Ryan Hopkins for teaching me spectral analysis and for all the help he has given me during the past two years. Last but not least, my most sincere thanks to my family and the friends I made at Western University for their support and encouragement throughout my academic stay at the University of Western Ontario.

We would also like to acknowledge and thank Jack Mustard and Kevin Cannon for providing us with their synthetic basaltic glass spectral endmember parameter, which was used to map the geospatial distribution of putative basaltic quenched glass (at spectral fractions of ~15% or higher) in the central uplift of Alga Crater.

Table of Contents

Abstract.....	ii
Table of Contents.....	iv
List of Tables.....	viii
List of Figures.....	ix
1 Introduction.....	1
1.1 Mars.....	4
1.1.1 Mars in the Solar System.....	4
1.1.2 Equipotential surface and elevation.....	5
1.1.3 Temperature.....	5
1.1.4 Atmospheric Composition.....	5
1.1.5 Wind.....	5
1.1.6 Magnetosphere and the loss of the primordial atmosphere.....	6
1.1.7 Global crustal dichotomy.....	7
1.1.8 Geography of Mars.....	9
1.2 Geological history of Mars.....	11
1.2.1 The Noachian.....	12
1.2.2 The Hesperian.....	13
1.2.3 The Amazonian.....	14
1.3 Mineralogy of Mars.....	17
1.3.1 Orbital detection and identification of mineralogy.....	17
1.3.2 Early weathering history.....	19
1.4 Impact cratering.....	20
1.4.1 Simple craters.....	21
1.4.2 Complex craters.....	22

1.5	Three stages of impact crater formation	24
1.5.1	Contact and compression stage	24
1.5.2	Excavation stage	24
1.5.3	Modification stage	25
1.6	Impactites	27
1.7	References	28
Chapter 2		46
2	Morphological, Structural and Spectral Mapping of the Central Uplift of Alga Crater, Ladon Basin, Mars	46
2.1	Introduction	46
2.2	General Geological Setting: Alga Crater	48
2.2.1	Previous studies on Alga Crater	50
2.3	Methodology	51
2.3.1	Datasets	51
2.3.2	Morphological and structural mapping	53
2.3.3	Spectral analysis	54
2.3.4	THEMIS-derived thermal inertia	55
2.4	Results	56
2.4.1	Massive and fractured bedrock (MFB) unit	58
2.4.2	Dark-toned clast-rich unit	67
2.4.3	Dark-toned clast-poor unit	67
2.4.4	Dark-toned pit-bearing unit	68
2.4.5	Unconsolidated materials	70
2.4.6	Aeolian deposits	70
2.4.7	Lineaments	70
2.5	Discussion	73

2.5.1	Interpretation of morphological units	73
2.5.2	Structure of the central uplift	81
2.5.3	Origin(s) of the exposed bedrock.....	82
2.6	Conclusions.....	84
2.7	References.....	86
3	Morphological, Structural and Spectral Mapping of the Central Uplift of Verlaine Crater, Sabae Terra, Mars	96
3.1	Introduction.....	96
3.2	General Geological setting: Verlaine Crater.....	98
3.3	Methodology.....	100
3.3.1	Datasets.....	100
3.4	Results.....	101
3.4.1	Massive and fractured bedrock (MFB) unit.....	104
3.4.2	Brecciated unit	111
3.4.3	Dark-toned clast-rich unit	111
3.4.4	Dark-toned clast-poor unit	112
3.4.5	Medium-toned clast-poor unit.....	112
3.4.6	Dark-toned pit-bearing unit.....	112
3.4.7	Unconsolidated materials.....	113
3.4.8	Aeolian deposits.....	113
3.4.9	Lineaments	114
3.5	Discussion.....	116
3.5.1	Interpretation of morphological units	116
3.5.2	Structure of the central uplift	123
3.5.3	Geology and mineralogy of the central uplift of Verlaine Crater	123
3.6	Conclusions.....	126

3.7	References.....	127
4	Final discussion and conclusions	136
4.1	Review	136
4.2	Limitations of remotely-based geological mapping	138
4.3	Future work.....	139
4.4	References.....	140
	Curriculum Vitae	143

List of Tables

Table 2.1. Orbital datasets used in this study.....	53
Table 2.2. Properties of each morphological units.	58
Table 2.3. Themis-derived thermal inertia for each morphological units.....	61
Table 2.4. CRISM spectra regions of interest (ROIs) and denominators.	66
Table 3.1. Orbital datasets used in this study.....	100
Table 3.2. Properties of each morphological units.	104
Table 3.3. Themis-derived thermal inertia for each morphological units.....	107
Table 3.4. CRISM spectra regions of interest (ROIs) and denominators.	111

List of Figures

- Figure 1.1. Global mosaics of Mars centered on Valles Marineris (left), Cerberus region (center) and Syrtis Major region (right) (from NSSDCA Photo Gallery Mars). 4
- Figure 1.2. High-resolution topographic shaded relief map of Mars showing the dichotomy between the northern lowlands and the southern heavily cratered highlands. From Neumann et al. (2001); Smith et al. (2001). 8
- Figure 1.3. Geological timeline of Mars. 11
- Figure 1.4. Timeline of major processes in Mars history. From Ehlmann et al. (2011).. 16
- Figure 1.5. Schematic cross-section of a simple impact crater showing apparent crater diameter (D_a), true depth (d_t) and apparent depth (d_a). The bowl-shaped depression is filled with crater-fill deposits and ejecta is found outside the crater rim. From Osinski and Pierazzo (2012). 22
- Figure 1.6. (a) Schematic cross-section showing the principal features of a complex impact crater. Note the structurally complicated rim, the down-faulted annular through, and the uplifted central area. (b) Schematic cross-section showing an eroded version of the fresh complex crater in (a). Note that in this case, only the apparent crater diameter can typically be defined. From Osinski and Pierazzo (2012). 23
- Figure 1.7. Series of schematic cross-section depicting the three main stages in the formation of both simple (left) and complex (right) craters. From Osinski and Pierazzo (2012)... 26
- Figure 1.8. Schematic cross-section illustrating a small central peak based on terrestrial data, and the three types of impactites (autochthonous, parautochthonous, allochthonous). Black areas represent high concentration of either crater-fill impact melt rocks, melt-bearing breccias or lithic breccias. Small triangles represent lithic and melt-bearing breccias part of the ejecta. From Grieve and Therriault (2013). 27
- Figure 2.1. A: MGS MOLA colourized hillshade map showing the geographical setting of the ~19-km diameter Alga Crater and its surrounding region. B: MGS MOLA topography

over THEMIS Day IR delineating the extent of Chekalin and Alga Craters. Dotted line indicates MOLA profile from A to A'. C: MGS MOLA topography data from MEGDR over THEMIS Day IR showing cross-section starting and terminating beyond the rims of Chekalin Crater..... 49

Figure 2.2. A: CTX image P18_007929_1555_XI_24S026W of Alga Crater. B: HiRISE orthoimage PSP_007929_1555 of the central uplift of Alga Crater..... 56

Figure 2.3. Morphological map of the central uplift of Alga Crater over HiRISE orthoimage PSP_007929_1555..... 57

Figure 2.4. Morphological units of HiRISE RED orthoimage PSP_007929_1555 and IRB orthoimage PSP_007573_1555. Refer to Fig. 2.3 to view location of each morphological units indicated by the letter ID. A: MFB in southwestern section showing dark-toned lineaments ranging from ~80–140 m in length of southwest-northeast orientation. B: MFB in the eastern section of the central uplift showing dark-toned lineaments. C: MFB in the southern section of the uplift which appears as a geological window. D: Well-exposed outcrops of MFB in the northwestern section of the uplift. E: Dark-toned clast-rich unit at the eastern crater floor showing coarser light-toned clasts enrichment. F: Dark-toned clast-rich unit at the western crater floor showing finer-grained light-toned clasts enrichment. G: Dark-toned clast-rich unit located at the northern margin of an outcrop of MFB. H: Dark-toned clast-poor unit in the eastern section of the uplift and showing crater-retaining morphology. I: Dark-toned clast-poor unit in the western section of the uplift. J: Dark-toned pit-bearing unit at the southern crater floor showing relatively shallow circular pits. K: Unconsolidated materials located on the northwestern slope of the uplift. L: Aeolian bedforms at the southern crater floor. Images credit: NASA/JPL/University of Arizona.61

Figure 2.5. Themis-derived thermal inertia map overlying CTX image P18_007929_1555_XI_24S026W of Alga Crater (stretch 162 to 614 J m⁻² K⁻¹ s^{-1/2})...... 62

Figure 2.6. Mafic spectral parameter and summary product superposed on HiRISE orthoimage PSP_007929_1555..... 63

Figure 2.7. Ratioed CRISM I/F spectra extracted from FRT00006415_07_IF164. A: OLINDEX spectra from ROIs representing outcrops of MFB in the northwestern and western sections of the uplift. B: LCPINDEX spectra from ROIs representing outcrops of MFB in the northern, western, southwestern and eastern sections of the uplift. C: OLINDEX spectrum from a ROI taken on the dark-toned clast-rich. D: LCPINDEX spectra from ROIs taken on the dark-toned clast-rich unit at the crater floor in the northwestern and western sections of the uplift and on the dark-toned clast-poor unit in the northwestern and southwestern sections of the uplift. E: Laboratory spectrum olivineKI3005 from the USGS digital spectral library splib01. F: Laboratory spectrum enstatiteNMNH128288 from the USGS digital spectral library splib01. 65

Figure 2.8. HiRISE orthoimage PSP_007929_1555. The relationship between 4 morphological units is illustrated here: a high-standing topographic feature overlain by the dark-toned pit-bearing unit is embayed within the dark-toned clast-poor unit. The topographic feature is characterized by clast-rich materials on its north-facing slope and putative flow features on its south-facing slope. 69

Figure 2.9. A: Structural mapping over HiRISE orthoimage showing lineaments cross-cutting the MFB. Dotted lines represent the three sections for which rose diagrams were produced (red: western, blue: eastern and green: southwestern). B: Southwestern section showing lineaments with preferential southwest-northeast trend. C: Eastern section showing lineaments with varying trends. 71

Figure 2.10. Stereonet rose diagrams of lineaments measured from 0 to 180 ° and mirrored in order to form a 360 ° plot for the central uplift of Alga Crater. A: Western section. B: Eastern section. C: Southwestern section. D: Southeastern section. 72

Figure 2.11. A: View from the southwest showing the transition between the clast-poor and clast-rich impact melt rocks, contained within outcrops of MFB. B: View from the northwest showing unconsolidated materials near the top of the uplift, overlying clast-poor impact melt rocks. Clast-poor impact melt is observed on both sides of a well-exposed outcrop of MFB, and grades into the clast-rich facie downward towards the crater floor. 75

Figure 2.12. CRISM glass spectral parameter and summary colour composite (red: OLV_TOT, green : GLASS, blue : LCPINDEX; courtesy of Kevin Cannon and John “Jack” Mustard, Brown University) (see Cannon and Mustard, 2015 for details). Mixtures of glass and olivine are modeled around outcrops of olivine-bearing MFB in the western and northwestern sections of the central uplift. 79

Figure 3.1. A: MOLA MEGDR colourized hillshade showing the geographical setting of the study area. B: A close-up showing the extent of Verlaine Crater and the northeastern section of the rim cross-cut by valley networks. C: A MOLA-derived north-south topographic profile of Verlaine Crater. 100

Figure 3.2. A: HRSC image H6387_0000_ND3 of Verlaine Crater and showing the 5 km crater northwest the central uplift of Verlaine. B: CTX image B09_013213_1707_XN_09S295W of the central uplift and floor of Verlaine Crater. C: HiRISE RED orthoimage ESP_013635_1705 overlying CTX image showing the central uplift of Verlaine Crater..... 102

Figure 3.3. Morphological map of the central uplift of Verlaine Crater over HiRISE RED orthoimage ESP_013635_1705. 103

Figure 3.4. Morphological units. HiRISE RED orthoimage ESP_013635_1705 and IRB image ESP_013635_1705. Refer to Fig. 2.3 to view location of each morphological units indicated by the letter ID. A-B: MFB in the central uplift. C: Dark-toned clast-poor unit (left) contiguous to brecciated unit (centre) and to the MFB (right). Note the sharp contact between the dark-toned clast-poor and brecciated units. D: MFB and brecciated unit coated by the dark-toned clast-poor unit in the central uplift. E: Dark-toned clast-rich unit in the eastern section of the uplift. F: Dark-toned clast-poor unit observed in the central uplift. G: Dark-toned clast-poor unit overlain by the medium-toned clast-poor unit in the northern section of the uplift. H: Dark-toned pit-bearing unit overlain by aeolian deposits. I: Dark-toned pit-bearing unit with clast-rich deposits at the southern crater floor. J: Unconsolidated materials in the southern section of the uplift. K: Aeolian bedforms (network dunes) within the off-centered irregular depression at the south of the uplift. L: Aeolian bedforms (linear dunes) in the southern section of the uplift..... 107

Figure 3.5. Themis-derived thermal inertia map overlying HiRISE RED orthoimage ESP_013635_1705 of Verlaine Crater (stretch 233 to 576 J m ⁻² K ⁻¹ s ^{-1/2}).....	108
Figure 3.6. CRISM colour composite (Red: D2300 0.000-0.035, Green: OLINDEX2 0.000-0.124, Blue: BD1900R 0.000-0.020).....	109
Figure 3.7. Ratioed CRISM I/F spectra extracted from FRT00012CD9_07_IF164. A: OLINDEX spectra taken on a topographic high-standing outcrop in the central uplift. B: Laboratory spectrum olivineKI3188 from the USGS digital spectral library splib01. C: D2300 spectra from the MFB in the southwestern section of the uplift. D: BD1900R from the MFB in the northern section of the uplift. E: Laboratory spectrum nontronite NDJB26 from the CRISM phyllosilicates spectral library.	110
Figure 3.8. Structural mapping over HiRISE with rose diagrams for the southwestern, northwestern, and northeastern sections of the uplift showing orientations of lineaments cross-cutting the MFB. B: Window showing lineaments in the centre of the uplift with preferential south-north trend. C: Window in the centre of the uplift showing lineaments with preferential southwest-northeast and southeast-northwest trends.	114
Figure 3.9. Stereonet rose diagrams of lineaments measured from 0 to 180 ° and mirrored in order to form a 360 ° plot for the southwestern, northwestern and northeastern sections of the central uplift of Verlaine Crater.....	115
Figure 3.10. HiRISE RED perspective based on an orthorectified HiRISE ESP_013635_1705 on the HiRISE-derived DTM DTEED_013213_1705_013635_1705_A01. View from the north of the central uplift showing the morphological units.....	116
Figure 3.11. Megabreccia in the central uplifts of complex craters. A-C: Verlaine megabreccia. D: Toro megabreccia. E: Holden megabreccia. F: Ritchey megabreccia. Images credit: NASA/JPL/University of Arizona.....	119

Chapter 1

1 Introduction

Impact cratering is a ubiquitous geological process that has shaped and modified the surface of the rocky and icy bodies of the Solar System. For a geologically active planet such as Earth, most of the impact cratering record has been eradicated, or is obscured by water and vegetation. However, orbital observations of Mercury, Venus, the Moon and Mars have made it possible to remotely study the impact cratering process. For instance, the Moon has revealed itself to be an excellent natural laboratory for the study of impact cratering for numerous reasons: it is geologically inactive, hence no post-impact aeolian and/or aqueous processes have eroded impact structures; it possess a relatively simple target lithology that has been extensively studied; and the absence of an atmosphere combined with a weak gravitational acceleration results in higher cratering efficiency (Osinski and Pierazzo, 2012). On the other hand, Mars is not only the most Earth-like terrestrial planets of the Solar System, but its surface is marked by widespread evidences of past aqueous alteration. It also exhibits a much better preserved impact cratering record than Earth (Strom et al., 1992).

Impact craters are generally categorized into two main forms: simple and complex. Simple craters consist of bowl-shaped depressions, with depth-to-diameter ratios of approximately 1:5 to 1:7 (Melosh, 1989). Complex craters have a greater diameter than simple craters, but are shallower, with depth-to-diameter ratios of 1:10 to 1:20. Their general morphology can be described by the presence of a centrally uplifted area, the so-called central uplift (Dence, 1968; Pike, 1980a; Melosh, 1989), surrounded by a down-faulted annular through, and a structurally complicated rim (Osinski and Pierazzo, 2012). Lithologies within central uplifts are known to be located stratigraphically above their pre-impact position (Dence, 1968). It is also notable that of the 188 confirmed terrestrial impact craters, only ~40 of them have well-exposed central uplifts, and ~20 of them have been mapped in detail (Kenkmann et al., 2005); hence the study of impact craters on other planetary bodies such as the Moon and Mars.

Based on visible and thermophysical characteristics, Tornabene et al. (2010) compiled a geodatabase of 188 pristine (i.e., young and fresh/least modified) Martian complex craters with fair, good, and very good exposures of bedrock within their central uplifts. These authors recorded and catalogued three main textural types of parautochthonous (i.e., pre-existing crater exposed) bedrock: layered bedrock (LB), massive and fractured bedrock (MFB) and megabrecciated bedrock (MBB) as well as associated impact-related structures (e.g., folds, fractures, faults, and dikes). There has been very little detailed work on these well-exposed Martian impact craters. Skok et al. (2012) conducted detailed spectroscopic analysis, and some morphological mapping of Alga and Ostrov Craters. Marzo et al. (2010) conducted spectroscopic and morphologic analysis of megabrecciated bedrock (MBB) in Toro Crater. Nuhn et al. (2014) conducted detailed decametre-scale morphological and structural mapping of layered bedrock (LB) within the central uplift of Betio, Byala, and Halba Craters. Ding et al. (2015) conducted morphological, structural, and spectral mapping of megabrecciated bedrock (MBB) in Ritchey Crater.

Martian central uplifts expose uplifted deep-seated bedrock, some of which could correspond to the primitive mafic-rich Martian crust (Tornabene et al., 2010, 2014; Quantin et al., 2012; Caudill et al., 2012; Skok et al., 2012; Pan et al., 2015). Exposures of subsurface material have also been known to prevail in outflow channels (Rogers et al., 2005; Loizeau et al., 2010), and tectonic rifts, with Valles Marineris being a prime example on Mars (Flahaut et al., 2011). However, the widespread and random distribution of impact craters across Mars make them optimal environments for the global study of subsurface material. Furthermore, they allow for the remote acquisition of clear spectral signatures as exhumed layers are well-exposed along vertical slopes of the uplift (Melosh, 1989; Tornabene et al., 2015). The complexity behind the study of central uplifts lies in the fact that they expose pre-, syn-, and post-impact units: the pre-impact bedrock is often obscured by post-impact deposits such as dunes and dust, and by impact-related deposits such as impactites (Caudill et al., 2012; L.L. Tornabene et al., 2013; Tornabene et al., 2015). Spectrally, central uplifts may contain exposures of excavated Noachian-aged unaltered mafic units, aqueously formed and/or altered phases (Bibring et

al., 2006; Wray et al., 2008; Mustard et al., 2008; Murchie et al., 2009a; Ehlmann et al., 2009, 2011; Carter et al., 2010; Tornabene et al., 2010, 2015; L.L. Tornabene et al., 2013; Osinski et al., 2013).

The widespread distribution of phyllosilicates, a class of hydrous minerals, appears to be constrained to the heavily cratered ancient terrains of Mars. High water activity and moderate to alkaline pH, two essential conditions for the formation of phyllosilicates, may have been supported during Noachian-aged environments. Phyllosilicates have been detected in rims, walls, ejecta deposits, and central uplifts of complex craters, suggesting that they could have been uplifted and then excavated, or the resulting products of impact-generated hydrothermal activity (Poulet et al., 2005; Bibring et al., 2006; Wray et al., 2008; Mustard et al., 2008; Murchie et al., 2009a; Ehlmann et al., 2009, 2011; Carter et al., 2010; L.L. Tornabene et al., 2013).

This research specifically addresses the massive and fractured bedrock (MFB) class of central uplift on Mars, and aims at combining the morphological, structural, and spectral mapping observations in order to elucidate the origin of the bedrock, the emplacement and extent of impactites, and other deposits in central uplifts in relationship to the surrounding local, regional, and global Martian geology. Ultimately, the goal is to inform on central uplift formation and the impact cratering process.

1.1 Mars

1.1.1 Mars in the Solar System

Named after the Roman god of war, Mars is the fourth terrestrial planet from the Sun. It possesses two natural satellites, Phobos and Deimos, both discovered by American astronomer Asaph Hall III in 1877.

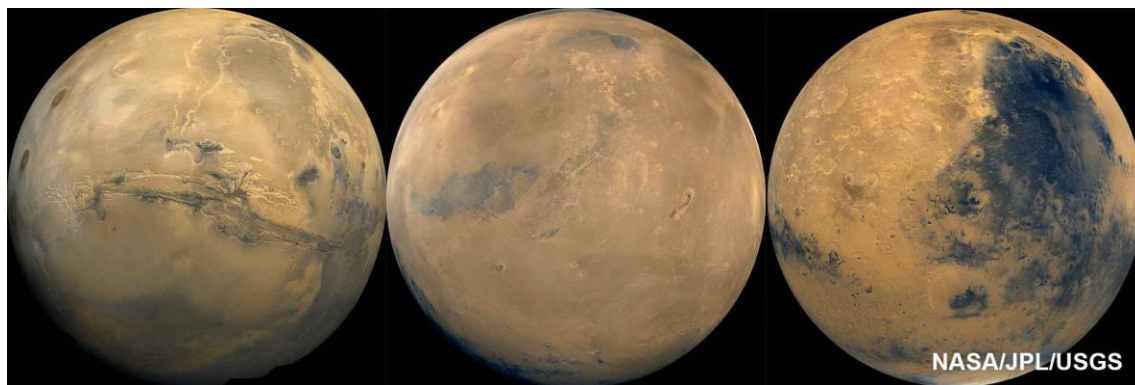


Figure 1.1. Global mosaics of Mars centered on Valles Marineris (left), Cerberus region (center) and Syrtis Major region (right) (from NSSDCA Photo Gallery Mars).

The volumetric mean radius of Mars approximates 3,389.508 km, which corresponds to about half of the radius of Earth. Comparatively, the surface area of Mars corresponds to 28.25% of the Earth's (Hartmann and Neukum, 2001; Carr, 2006).

Gravity on Mars is ratioed to 0.375 of that of Earth. The mean orbital period corresponds to 686.98 Earth days, or 669.60 Mars solar days (sols) (i.e. name for a day on Mars), at an average orbital velocity of 2.4077×10^4 m/s. The mean solar day is equivalent to 24h 39m 35.2s on Earth (Hartmann and Neukum, 2001; Carr, 2006).

The orbit of Mars is the second most eccentric ($\epsilon=0.0934$ A.U. (Astronomical Unit)) among all the other planets of the Solar System, with the exception of Mercury ($\epsilon=0.2056$ A.U.). At perihelion, or its nearest distance to the Sun, Mars receives 45% more sunlight than at aphelion, its farthest distance to the Sun (Hartmann and Neukum, 2001; Carr, 2006).

1.1.2 Equipotential surface and elevation

Elevation on Mars is referenced to an equipotential surface with an average radius value of 3,396 km at the equator (Smith et al., 1999). The southern highlands stand above this equipotential surface, whereas the northern lowlands stand below it (Carr, 2006).

Elevation range from -8,200 km at the base of Hellas Planitia to +21,229 km at the summit of Olympus Mons (Carr, 2006).

1.1.3 Temperature

Although Mars is thought to have possessed a much thicker atmosphere in its early history, the present atmosphere is approximately 100 times thinner than Earth's (Owen, 1992; Carr, 2006). Low atmospheric density results in surface temperatures strictly controlled by solar heating and infrared cooling. Mean diurnal temperatures can reach values as low as -153 °C/150K at the poles, or -33 °C/240K on a warm day in the southern hemisphere. At the mid-southern latitudes in the summer, daily maxima can reach +27 °C/300K (Kieffer et al., 1977) if thermal inertia is at its lowest.

1.1.4 Atmospheric Composition

The atmosphere of Mars is composed of 95.3% carbon dioxide (CO₂), 2.7% nitrogen (N₂), 1.6% argon (Ar), 0.13% oxygen (O₂), and 0.07% carbon monoxide (CO) (Kieffer et al., 1992; Carr, 2006). The remaining components consist of water vapour (H₂O), and suspended dust particles that are responsible for the characteristic butterscotch tint to the atmosphere, which is explained by the absorption of blue light, and the scattering of the remaining wavelengths. If the atmosphere was free of dust particles, Rayleigh scattering by CO₂ molecules would result in a tinted dark blue atmosphere, similar to the shade of blue of the Earth's upper atmosphere (Owen, 1992).

1.1.5 Wind

Aeolian activity remains the most dynamic geological process occurring on Mars today. A variety of depositional and erosional landforms can be attributed to the present action of wind at the surface. From orbit, dunes, ripples, yardangs, wind tails/streaks, and dust

devil tracks are visible, whereas rovers and landers have recorded drifts, erosional moats, wind tails, ripples, and ventifacts. Global dust storms are another manifestation of the wide-scale wind activity on Mars. In 1971, Mariner 9, which became the first spacecraft to orbit Mars, was unable to catch a single glimpse of the Martian surface for weeks as the entire surface was obscured by a thick haze of red dust, with the sole exception of Olympus Mons, peeked above the widespread clouds of dust.

1.1.6 Magnetosphere and the loss of the primordial atmosphere

The very weak magnetic field around Mars exposes the planet to the harsh incoming solar wind. The magnitude of the magnetic field at the equator has been estimated to be <0.5 nT (Acuña et al., 2001), which corresponds to $\sim 10^{-6}$ of that of Earth's. Global remotely-sensed magnetic field measurements obtained in 1998 from the Mars Global Surveyor (MGS) revealed strong remanent crustal magnetic anomalies (Acuña et al., 1998; Acuña et al., 1999), indicating that the planet once possessed an appreciable global magnetosphere (Acuña et al., 2001). The crustal magnetization appears to be dichotomized as it is confined to the ancient southern highlands of Mars (Acuña et al., 1999, 2001; Connerney et al., 2001).

Prevailing surface temperatures and atmospheric pressure do not allow for water to exist in its liquid state. Yet, the surface of Mars is marked by extensive valley networks, and chaotic flood plains, thought to have been carved by large quantities of flowing liquid water that would have required a much thicker atmosphere protected by a magnetosphere. Several processes may explain the primordial removal of the upper Martian atmosphere: its ejection due to impact cratering/erosion, its lost in space due to pick-up-ion sputtering, or the absorption of CO₂ gas in the regolith as well as its sequestration in the polar caps as ice and/or clathrate (Brain and Jakosky, 1998). Still, it is the weakening and eventual decay of the magnetic field that facilitated the total depletion of the Martian atmosphere. The Mars Atmosphere and Volatile Evolution mission (MAVEN), launched in November 2013, will elucidate some of the mysteries surrounding the loss of this primordial atmosphere (Jakosky, 2011).

1.1.7 Global crustal dichotomy

The surface of Mars reveals a striking global dichotomy, known as the highland-lowland boundary (HLB), and centered at latitude $\sim 50^\circ\text{N}$, that separates the heavily cratered southern highlands from the smooth and flat northern lowlands (Fig. 1.2). This crustal dichotomy, of which the origin still remains an unsolved matter, has been resurfaced and modified by erosional processes from the action of liquid water, water-ice interactions, and wind, as well as from gravity-driven processes (McGill, 2002, 2005; Tanaka et al., 2005; Baker et al., 2007; Dickson et al., 2008; Chuang and Crown, 2009; Fairén et al., 2011; Davila et al., 2013), and deformations of endogenic origin (Phillips et al., 2001). One leading hypothesis for the formation of the highland-lowland dichotomy is from one giant impact basin (the Borealis Basin) or multiple large impact basins, known as the exogenic tectonic model (Wilhelms and Squyres, 1984; Frey and Schultz, 1988). A formation induced by endogenic tectonic processes (Wise et al., 1979; McGill and Dimitriou, 1990; Sleep, 1994; Zhong and Zuber, 2001; Lenardic et al., 2004; Roberts and Zhong, 2004) or from the erosional retreat of the southern highland plateau (Scott, 1978; Hiller, 1979) have also been proposed.

The southern heavily cratered highlands of Mars are very ancient. In fact, basin-rim material at the periphery of major impact basins (i.e., Hellas, Argyre, and Isidis) and around isolated hilly or mountainous landforms represent the oldest exposed material on Mars, with the exception of the basement complex (Scott and King, 1984) recognized in the western Martian hemisphere. Intercrater plains emplaced at a later time may represent lava flows, flood-plain and/or aeolian fill deposits that have partly resurfaced the ancient cratered terrains (Scott and Carr, 1976; Tanaka, 1986; Tanaka and Scott, 1987; Tanaka et al., 2014).

Past studies on the Martian northern lowlands have suggested that they are ancient degraded cratered terrains that have been widely resurfaced by plain materials of volcanic, and/or sedimentary origin that now constitute the Vastitas Borealis Formation (Tanaka, 1986; Tanaka and Scott, 1987; Tanaka et al., 1988). However, recent studies by Tanaka et al. (2003, 2005) indicate that the northern lowlands may have experienced

episodic local to regional volcanic and sedimentary infilling, as well as episodic widespread erosion of volatile-rich material.

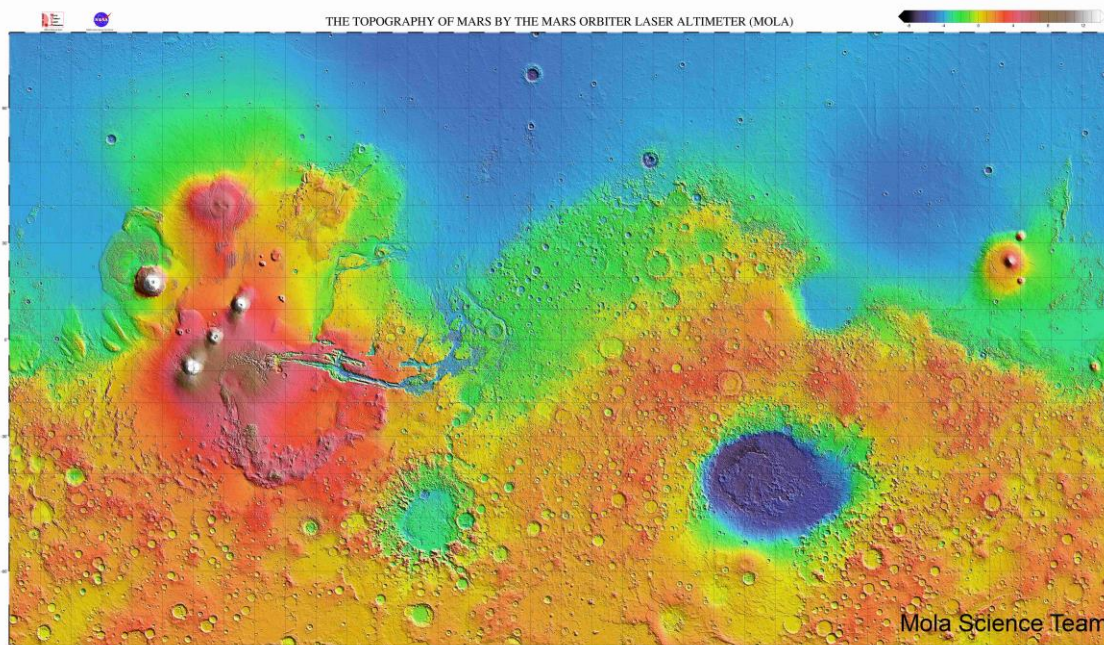


Figure 1.2. High-resolution topographic shaded relief map of Mars showing the dichotomy between the northern lowlands and the southern heavily cratered highlands. From Neumann et al. (2001); Smith et al. (2001).

1.1.8 Geography of Mars

1.1.8.1 Impact basins

The major impact basins on Mars are the Hellas (45 °S, 70 °E), Argyre (50 °S, 320 °E), Isidis (12 °N, 88 °E) and Utopia (45 °N, 110 °E) basins. The largest infilled basin is Hellas Planitia (~2,400 km diameter) (Smith et al., 1999). The floor of Hellas Planitia corresponds to the lowest elevation on Mars (~-8,200 km). Libya Montes, located south of Isidis Planitia, consists of rugged mountainous relief associated to the degraded rims of the Isidis Basin (Tanaka, 1986; Greeley and Guest, 1987).

1.1.8.2 Volcanic provinces

The volcanic province of Tharsis dominates the western hemisphere. It consists of the shield volcanoes Ascreus, Pavonis, and Arsia Montes, also collectively known as the Tharsis Montes, with Olympus Mons located along the northwestern flank of the Tharsis bulge. Olympus Mons is the largest shield volcano on Mars, with a diameter of ~640 km, and a peak that rises close to ~22 km above the surrounding terrain, making it the tallest observed mountain in the Solar System (Plescia, 2004). In contrast, the eastern hemisphere is dominated by the volcanic province of Elysium in the lowlands, which is composed of the shield volcanoes Hecates Tholus, Elysium Mons, and Albor Tholus. Syrtis Major Planum is a broad volcanic plain located southwest of Isidis Planitia, near the highland-lowland boundary.

1.1.8.3 Valley networks

Valley networks extensively dissect the southern heavily cratered highlands of Mars, mainly at low to mid (<60 °) latitudes. Their occurrences have been observed within large impact basins (e.g., Hellas Basin), crater walls, volcanoes, sides of massifs, intercrater plains, and across the highland-lowland boundary (Hynek et al., 2010). Carr (1995) previously identified 10,748 valleys on Mars, but the new study conducted by Hynek et al. (2010) detected 82,217 valleys.

1.1.8.4 Outflow channels

Outflow channels occur north of Valles Marineris. They consist of very long and wide channels thought to have been carved by outburst floods. Oppositely to valley networks, outflow channels branch downstream, beginning within the Martian highlands, with most of them debouching into the northern lowlands such as in the topographic depression of Chryse Planitia. Some channels may be more than 2,000 km long and 100 km wide.

They emanate from chaotic terrains and produce characteristic features such as streamlined tear-dropped islands and mesa channels. The six largest outflow channels are the Kasei, Maja, Simud, Tiu, Ares, and Mawrth Vallis (Carr and Clow, 1981).

1.1.8.5 Valles Marineris

Valles Marineris, or Mariner Valley, is a ~4,000 km long canyon system east of the Tharsis bulge, extending from Noctis Labyrinthus in the west to the chaotic terrain in the east. Horizontal layered deposits, some of which can be as thick as ~8 km, are exposed along the canyon walls, and considered as some of the best exposures of the upper Martian crust (McEwen et al., 1999). Some of the major sub-canyons are Melas, Ophir and Candor Chasmata. The study of these layered deposits can inform on the cratering and volcanism rates as well as the erosional, depositional and structural history of the planet.

1.1.8.6 Polar caps

The southern ~350 km diameter polar cap consists of permanent layered strata of ice and dust, overlain by a residual water-ice cap (Tanaka and Scott, 1987), which is in turn covered by a thin veneer of seasonal dry carbon dioxide-ice (Kieffer, 1979). The northern ~1,000 km diameter polar cap is mainly composed of H₂O ice (Kieffer et al., 1976) and covers almost the entire underlying layered terrain, whereas the southern cap exposes a greater area of layered terrain. Both the northern and southern polar caps are covered by dust deposits and surrounded by extensive dune fields.

1.2 Geological history of Mars

The study of the geological history of Mars has been revolutionized by the availability of remotely-sensed and ground-based data collected by successful orbiter and lander missions (Kieffer et al., 1992), complemented by the study of Martian meteorites (McSween and Treiman, 1998; Nyquist et al., 2001).

Based on rock sequences, a first time-stratigraphic Viking-based classification was established by Scott and Carr (1976) in which three systems were defined: the Noachian, characterized by heavily cratered degraded highlands; the Hesperian, marked by widespread ridged plains materials; the Amazonian, composed of smooth plains and polar deposits (Fig. 1.3). From the work on the western region of Mars conducted by Scott and Tanaka (1986), each stratigraphic system was later subdivided by Tanaka (1986) into "Upper" (late), "Middle", and "Lower" (early) epochs based on crater-size density frequency distribution, crater-flux models, and stratigraphic relationships. Hartmann and Neukum (2001) followed with age assignments for each stratigraphic system and their associated epochs (eight in total) based on a crater production function established by Ivanov (2001).

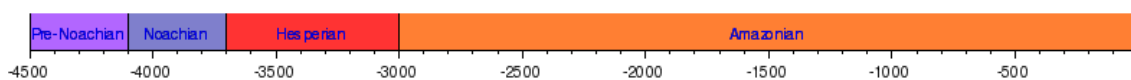


Figure 1.3. Geological timeline of Mars.

1.2.1 The Noachian

The Noachian is the oldest geological time period for Mars, and dates prior to ~3.5 Gyr. It takes its name from *Noachis Terra*, lit. "Land of Noah", a region to which are associated the oldest terrains on Mars (Scott and Carr, 1976; Scott and Tanaka, 1986; Tanaka, 1986; Tanaka and Scott, 1987; Hartmann and Neukum, 2001; Tanaka et al., 2014).

The Pre-Noachian refers to the time of accretion and differentiation of the planet (~4.5 Gyr) to the onset of the Late Heavy Bombardment (LHB), a violent period in the history of the Solar System when the early terrestrial planets were being battered by large-scale impactors (i.e., asteroids and comets) (Frey and Schultz, 1988; Hartmann and Neukum, 2001; Nimmo and Tanaka, 2005; Fassett and Head, 2011). A cratering model by Ivanov (2001) hypothesized that ~4 Gyr ago, a 100 km diameter crater would have formed every million years (Carr, 2006). Approximately 300 craters of this diameter may have formed on the Martian surface during the time scale allocated to the Noachian system. The Noachian crater size distribution by Strom et al. (1992) and model by Segura et al. (2002) hypothesized that a 300 m layer of ejecta deposits cover the surface of Mars as a result of cratering by impactors with diameters between 500 and 1,000 km.

The formation of the Hellas impact basin at the beginning of the LHB introduces the Early Noachian Epoch, also marked by the formation of the other major impact basins on Mars (Isidis, Argyre, south polar), and of the northern lowlands (Tanaka, 1986; Tanaka et al., 2003, 2005). The global crater database compiled by Robbins and Hynek (2012a, 2012b) estimate that at least 65 impact basins (diameters >150 km) date to the Early Noachian Epoch, with 18 of them being either deeply buried or heavily degraded. In contrast, the formation of the southern heavily cratered highlands is generally associated to the Middle Noachian Epoch, which also experienced the highest resurfacing rates (from impacts; ~0.3 km²/yr) (Tanaka et al., 1988; Hartmann and Neukum, 2001). In terms of volcanism, the majority of the activity was centered around Tharsis. In fact, by the late Noachian, the Tharsis bulge is hypothesized to have already been in place (Phillips et al., 2001).

In comparison to the pristine appearance of Hesperian-aged craters, the ones formed in the Noachian generally feature highly eroded rims and sediment-filled interiors. In fact, erosion rates during the Noachian have been estimated to be 1,000 times greater than present day Mars (Craddock and Maxwell, 1993; Hynek and Phillips, 2001; Craddock and Howard, 2002; Golombek et al., 2006). Furthermore, widespread cratered highlands are dissected by valley networks, of which most of the activity is thought to have peaked near the Noachian/Hesperian boundary, more or so towards the late Noachian (Baker et al., 1992; Howard et al., 2005; Irwin et al., 2005; Fassett and Head, 2008; Hoke and Hynek, 2009; Hynek et al., 2010; Tanaka et al., 2014).

1.2.2 The Hesperian

The Hesperian period is named after Hesperia Planum (from *Hesperia*, lit. "Lands of the West"), a type locale on Mars for the Hesperian-aged ridged plains materials, considered as the referent for the Early Hesperian Epoch. The Vastitas Borealis Formation, which can be accounted for resurfacing most of the northern lowlands, is the referent for the Late Hesperian Epoch (Scott and Carr, 1976; Scott and Tanaka, 1986; Tanaka, 1986; Tanaka et al., 2003, 2005).

The transition from the Noachian to the Hesperian period is characterized by a declining rate in impact cratering and erosion (Hartmann and Neukum, 2001; Golombek et al., 2006). At least four impact craters with diameters between 150 and 200 km have been dated to the Hesperian: Gale, Holden, Lowell, and Bakhuisen (Tanaka et al., 2014). On the other hand, the formation of "chaos" terrain and outflow channels in the late Hesperian (Tanaka et al., 2005) reflect pronounced episodes of erosion, although average rates of erosion have been estimated to be 2 to 5 orders of magnitude lower than during the Noachian (Golombek et al., 2006). On that matter, the formation of valley networks is reduced to localized and constrained carving in the Early Hesperian Epoch (Fassett and Head, 2008).

With a major geological shift away from impacts, volcanic activity predominates in the Hesperian, with an estimated eruption rate of $\sim 1 \text{ km}^3/\text{yr}$ (Greeley and Schneid, 1991). In fact, volcanism centered around Tharsis combined with catastrophic flooding may have been the major contributors to local and potentially global resurfacing of the planet in the Hesperian (Hynek, 2003; Baker et al., 2007; Dohm et al., 2009). The construction of extensive lava plains and paterae (i.e., shield-like central edifices) (Greeley and Spudis, 1981) alone resulted in 30% of the resurfacing of the planet (Head et al., 2002; Carr and Head, 2010), if we account for Hesperian-aged volcanic plains under the Amazonian-aged deposits in central Tharsis and Elysium (Tanaka et al., 1988). Because the rim of Valles Marineris is comprised of early Hesperian ridged plains materials (Greeley and Guest, 1987), the opening of the canyon is thought to postdate the early Hesperian (Webb and Head III, 2002a, 2002b; Montgomery et al., 2009). The opening of Valles Marineris may or may not have played a role in the major outburst floods that took place in the Hesperian. Nonetheless, it is thought that most of the water could have accumulated as ice deposits within low-lying depressions (Kargel et al., 1995; Kreslavsky, 2002). For instance, the Dorsa Argentea Formation may represent the remnant of an ancient circumpolar ice cap that formed in the Hesperian (Tanaka and Scott, 1987; Head and Pratt, 2001). The end of the Hesperian system has been estimated by Hartmann and Neukum (2001) to oscillate between ~ 3.3 and ~ 2.9 Gyr.

1.2.3 The Amazonian

The Amazonian is the youngest geological time period, encompassing two thirds of the history of Mars until present day. It is named after Amazonis Planitia, a smooth and widespread volcanic plain in the northern lowlands. The Amazonian is characterized by cold, hyperarid conditions as well as low erosion and weathering rates (Golombek et al., 2006).

The impact flux had significantly decreased by the early Amazonian, while volcanism remained prevalent, with most of the activity peripheral to the Tharsis and Elysium volcanic plateaus (Carr and Head, 2010; Hauber et al., 2011; Platz and Michael, 2011). Estimated average eruption rates dropped from $\sim 1 \text{ km}^3/\text{yr}$ in the Hesperian to $\sim 0.1 \text{ km}^3/\text{yr}$

in the Amazonian (Greeley and Schneid, 1991). Moreover, Amazonian volcanic eruptions may have been highly episodic (Neukum et al., 2004, 2010; Werner, 2009).

Fluvial activity during the Amazonian rarefied. However, young valley networks at Melas and Echus Chasmas (Mangold et al., 2004) have been hypothesized to have formed in the Amazonian (Fassett and Head, 2008) as well as outflow channels in Tharsis and southeast Elysium. Yet, gullies remain the main characteristic fluvial features associated with the Amazonian. They occur on steep slopes preferentially in the southern highlands at mid-latitudes (30–60 °) (Balme et al., 2006; Bridges and Lackner, 2006; Dickson et al., 2007; Dickson and Head, 2009).

The Amazonian period is characterized by the prevalence of erosive and depositional surficial processes resulting from the action of wind and ice. In fact, ice was a major agent of landscape modification during the Amazonian (Lucchitta, 1981; Kargel and Strom, 1992). This is manifested by the extensive northern and southern polar layered deposits, which yield an upper estimate of 3.2 to 4.7 million km³ of surface water (Smith et al., 1999). Both polar caps appear to have accumulated in the late Amazonian. (Herkenhoff and Plaut, 2000). On the other hand, the pervasive action of wind resulted in the accumulation of extensive dune fields all across the northern and southern polar caps (Langevin et al., 2005).

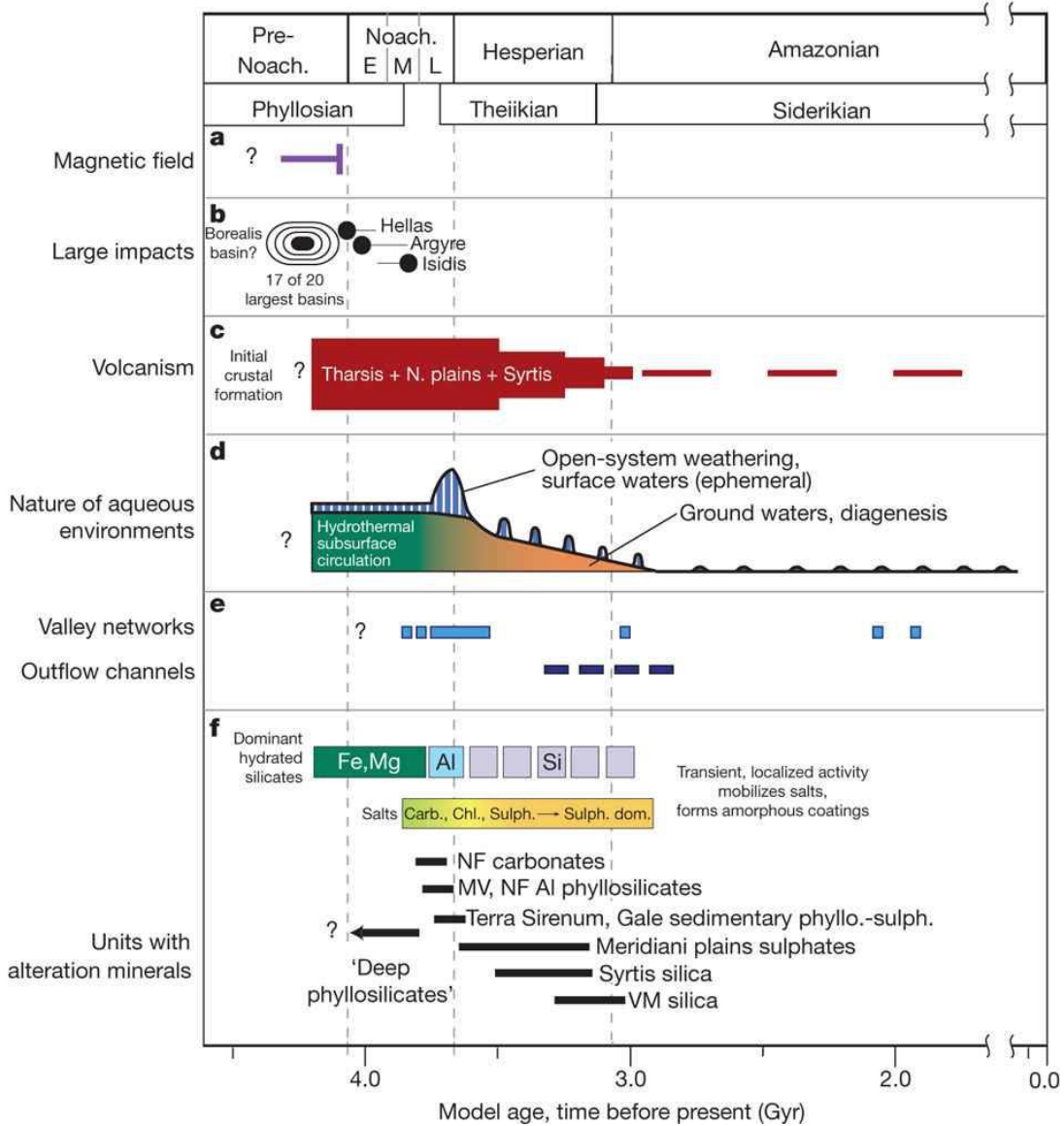


Figure 1.4. Timeline of major processes in Mars history. From Ehlmann et al. (2011).

1.3 Mineralogy of Mars

Orbital infrared spectroscopy combined with ground-based point spectroscopy have greatly contributed to our current understanding of the chemical history and composition of the planet. Starting in the late 1990s, the Thermal Emission Spectrometer (TES) (Christensen et al., 2001) onboard Mars Global Surveyor (MGS) provided the first thermal infrared (TIR) spectroscopic data of the Martian surface. It was followed in 2001 by the Thermal Emission Imaging System (THEMIS) (Christensen et al., 2004), a multispectral TIR imager onboard Mars Odyssey (MO). Visible to near-infrared orbital spectroscopy became possible with the Observatoire pour la Minéralogie, l'Eau, les Glaces, et l'Activité (OMEGA) camera (Bibring et al., 2005) onboard the European Space Agency (ESA)'s Mars Express (MEX) and at even greater resolution with the Compact Reconnaissance Imaging Spectrometer for Mars (CRISM) (Murchie et al., 2007) onboard Mars Reconnaissance Orbiter (MRO).

1.3.1 Orbital detection and identification of mineralogy

First of all, TES (Christensen et al., 2001) identified plagioclase, clinopyroxene, and "high-silica" as the three dominant primary mineral phases of low albedo regions of Mars (Bandfield et al., 2000; Christensen et al., 2000). The mineral olivine was also detected (Christensen et al., 2000), especially northeast of Syrtis Major (Hoefen et al., 2003). In summary, the southern highlands have a basaltic composition, dominated by plagioclase feldspar and clinopyroxene. In contrast, the northern lowlands differ with a more andesitic composition, dominated by plagioclase feldspar and volcanic (high-silica) glass (Christensen et al., 2001).

From 2004 up to present day, OMEGA (Bibring et al., 2005) primarily detected and mapped mafic iron-bearing silicates (olivines and pyroxenes). High-calcium pyroxenes such as clinopyroxenes were found to dominate in low albedo volcanic regions of Hesperian age, dark sands, and crater ejecta, and low-calcium pyroxenes such as orthopyroxenes were observed in the ancient Noachian-aged cratered terrains. Olivine was detected in the southern highlands, especially within the floor and rim of craters, in the vicinity of major impact basins, and has been associated to volcanic rocks in and

around Syrtis Major (Bibring et al., 2006). Furthermore, anhydrous nanophase iron oxides were found to be widespread across the Martian surface, especially within (bright) regions of high albedo. OMEGA detected for the first time the presence of two distinct classes of hydrated minerals, phyllosilicates and sulfates, which provide a record of water-rock interactions on Mars (Gendrin et al., 2005; Bibring et al., 2005, 2006; Poulet et al., 2005). Phyllosilicates were detected in ancient Noachian cratered terrains at Mawrth Vallis, Nili Fossae, and north of the Syrtis Major volcanic plateau, whereas sulfates were detected in light-toned layered deposits at Valles Marineris, Aram Chaos, Terra Meridiani, and within dark dunes adjacent to the northern polar cap (Arvidson et al., 2005; Bibring et al., 2005, 2006; Poulet et al., 2005). Phyllosilicates detected by OMEGA are consistent with smectite clays. For instance, nontronite, the iron-rich end member of the smectite clays, is the most abundant phyllosilicate detected by OMEGA. Al-rich smectite clays such as montmorillonite were also found to be locally dominant. Sulfates detected by OMEGA include magnesium sulfates, such as kieserite, and calcium sulfates such as gypsum. Although trace amounts of carbonates were detected in silicate-rich dust from TES data (Bandfield et al., 2003), OMEGA did not detect any carbonate-rich deposits (Bibring et al., 2005, 2006).

Since 2006, CRISM (Murchie et al., 2007) has revealed unprecedented mineralogical diversity across the Martian surface. CRISM has distinguished two classes of phyllosilicates: Fe/Mg smectites (e.g., nontronite, saponite), constrained to the ancient heavily cratered terrains of Mars, more specifically in crater rims, ejecta, and central peaks of complex craters, and Al smectites (e.g., montmorillonite, beidellite) (Mustard et al., 2008). CRISM also identified a wide new range of hydrated silicate minerals such as kaolinite, chlorite, potassium micas such as illite or muscovite, and hydrated (opaline) silica as well as magnesium carbonate and prehnite (Ehlmann et al., 2008; Milliken et al., 2008; Mustard et al., 2008, 2009). Furthermore, serpentine and the sodium zeolite analcime were first detected by Ehlmann et al. (2009) in Nili Fossae.

1.3.2 Early weathering history

The weathering history of Mars has been categorized into three distinct periods of chemical alteration defined and described by Bibring et al. (2005, 2006). The "Phyllosian", associated with the Early and Middle Noachian, is described as a period of neutral to basic acidity, with aqueous alteration producing phyllosilicates. The "Theiikian", associated from the Late Noachian up until the Middle/Late Hesperian, is described as an acidic period of aqueous alteration producing sulfates. Finally, the "Siderikian", associated with the Late Hesperian up to the present day, is an atmospheric period free of aqueous alteration, where recent weathering has resulted in the formation of anhydrous ferric oxides. However, in the context of this study, the conventional terms (i.e., Noachian, Hesperian, and Amazonian) established by Tanaka (1986) will be employed.

Chemical alteration of unstable primary mineral phases (i.e., olivines, pyroxenes, feldspars) to secondary stable altered phases (i.e., phyllosilicates, oxides, salts, amorphous phases) (Ehlmann et al., 2011) accounts for the mineralogical diversity of the Martian surface. Global bedrock exposures of hydrated silicates, particularly clays and amorphous phases, have been recorded all across the heavily-cratered Noachian highlands. Climate-driven formation of smectite clays at the surface of Mars would have necessitated neutral to alkaline pH, relatively high water activity and a significant water reservoir. However, the formation of smectite clays appear to have occurred mostly in the subsurface, and hydrothermal groundwater circulation has been proposed as one mechanism (Griffith and Shock, 1997; Michalski and Niles, 2010; Ehlmann et al., 2011; Loizeau et al., 2012). Impact-generated hydrothermal activity has also been suggested as a driving mechanism for the formation of hydrated silicates on Earth and Mars (L.L. Tornabene et al., 2013; Osinski et al., 2013).

Other scenarios for the *in situ* formation of phyllosilicates have been proposed. Deposition of sediments in an aqueous environment and the alteration of volcanic ash deposits by the action of liquid water have been suggested by Loizeau et al. (2007). A recent study of candidate open-basin lakes by Goudge et al. (2012) suggested that

aqueously altered minerals could have originated from their transport within lacustrine deposits. Newly published work on the catchment and delta deposits at Jezero Crater also argues for a transported origin of the alteration minerals, of which the formation is disassociated to the fluvial activity that initially formed the Jezero Crater paleolake (Goudge et al., 2014).

1.4 Impact cratering

Impact craters, known to exhume subsurface material that may otherwise be buried, can be classified into two main types: simple and complex (Pike, 1980b; Melosh, 1989; French, 1998; Grieve, 2012). Simple craters are described as bowl-shaped depressions with diameters less than a few kilometres across, whereas complex craters are larger structures that display a centrally uplifted region, a down-faulted annular through, and terraced walls. With increasing crater diameter, complex craters may be further categorized into central-peak basin (i.e., a fragmentary ring of peaks surrounding a central uplift), peak-ring basin (i.e., absence of central uplift, but well-developed ring of peaks), and multi-ring basins (i.e., at least two concentric rings inside the crater), the latter being the largest recorded impact structure in the Solar System.

On Earth, the transition is estimated to occur at approximately 4 km for massive crystalline targets and 2 km for sedimentary targets. On Mars, gravity is 38% that of Earth, and the transition occurs from 5 to 10 km. On the Moon, gravity is 17% that of Earth, and transition occurs from 15 to 27 km. Therein, the transition diameter is an inverse function of the planet's gravitational acceleration. However, the target lithology as well as the composition and angle of the impactor/projectile are also factors to be considered (Pike, 1980b; Melosh, 1989; Garvin and Frawley, 1998; Stewart and Valiant, 2006; Boyce and Garbeil, 2007; Robbins and Hynek, 2012b).

The formation of hypervelocity impact structures can be divided into three stages: (1) contact and compression, (2) excavation, and (3) modification. Hypervelocity refers to a projectile/bolide striking the surface at its original cosmic velocity, resulting in high-pressure shock waves propagation through the target material. The projectile must be

large enough to enter the atmosphere with little or no deceleration, which usually requires mean sizes of >50 m for a stony object, and >20m for an iron body (Osinski and Pierazzo, 2012).

The lack of an atmosphere on the Moon has allowed for a better preservation of the original morphology of impact structures. As for Mars, high erosion rates during the Noachian and resurfacing in the Hesperian have contributed to the present degraded state of impact structures, whereas wind acts as an ongoing dominant agent of erosion. Still, impact structures on Mars are better preserved than the ones on Earth. In fact, high weathering and erosion rates on Earth over long periods of time have quickly altered the once pristine appearance of impact structures. Furthermore, obstruction by vegetation, water (e.g., lakes, rivers, oceans) and/or ice makes it harder to recognize impact structures or capture them from space.

1.4.1 Simple craters

A simple crater can be defined as a hollow bowl-shaped depression in the ground. When relatively fresh, a simple crater will possess an uplifted rim, and an interior filled with allochthonous breccia lens comprising unshocked target material and/or impact-melt bearing lithologies. These crater-fill deposits most likely resulted from the inward collapse of the transient cavity walls. A theoretical cross-section of a simple crater (Fig. 1.5) distinguishes the final crater (rim-to-rim) diameter (D), the apparent crater diameter (D_a), in a context where crater rims have been eroded away, the true depth (d_t), and the apparent depth (d_a). The final crater diameter is usually 10% to 20% greater than the original crater diameter prior to the inward collapse of the transient cavity walls. The true depth (d_t) corresponds to the depth of the original transient cavity, from the crater rim to the base of the crater-fill deposits, and the apparent depth (d_a) is measured from the rim to the top of the crater-fill deposits. Simple craters have depth-to-diameter ratios of 1:5 to 1:7 (Melosh, 1989). On Earth, the best preserved simple crater is the 1.2 km Meteor or Barringer Meteor Crater in Arizona that formed ~50,000 years ago (Shoemaker, 1960). On Mars, Zumba Crater is another classic representation of a simple crater.

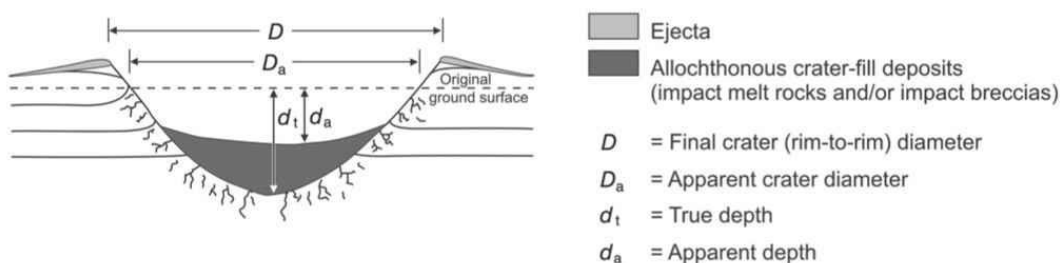


Figure 1.5. Schematic cross-section of a simple impact crater showing apparent crater diameter (D_a), true depth (d_t) and apparent depth (d_a). The bowl-shaped depression is filled with crater-fill deposits and ejecta is found outside the crater rim. From Osinski and Pierazzo (2012).

1.4.2 Complex craters

A complex crater possess a structurally complicated rim and a centrally uplifted area (i.e., central peak, central uplift), which is surrounded by a down-faulted annular through (Fig. 1.6). Complex craters are of particular interest as they expose deep-seated bedrock that was uplifted during the impact process. Since complex craters are shallower than simple craters, the depth-to-diameter ratio is usually 1:10 to 1:20 (Melosh, 1989). As for the central uplift, it usually corresponds to 1/10 of the diameter for craters on Earth; it is defined by the empirical relationship $SU=0.086D^{1.03}$, where D is the final diameter (Grieve and Pilkington, 1996). Hence, a complex crater on Earth with a diameter of 20 to 30 km would have a centrally uplifted area of 2 to 3 km. The 29 km Tooting Crater on Mars and the 27 km diameter Euler Crater on the Moon are classic examples of complex craters. On Earth, the Ries impact structure in Germany and the Vredefort impact structure in South Africa are famous and well-studied examples complex craters.

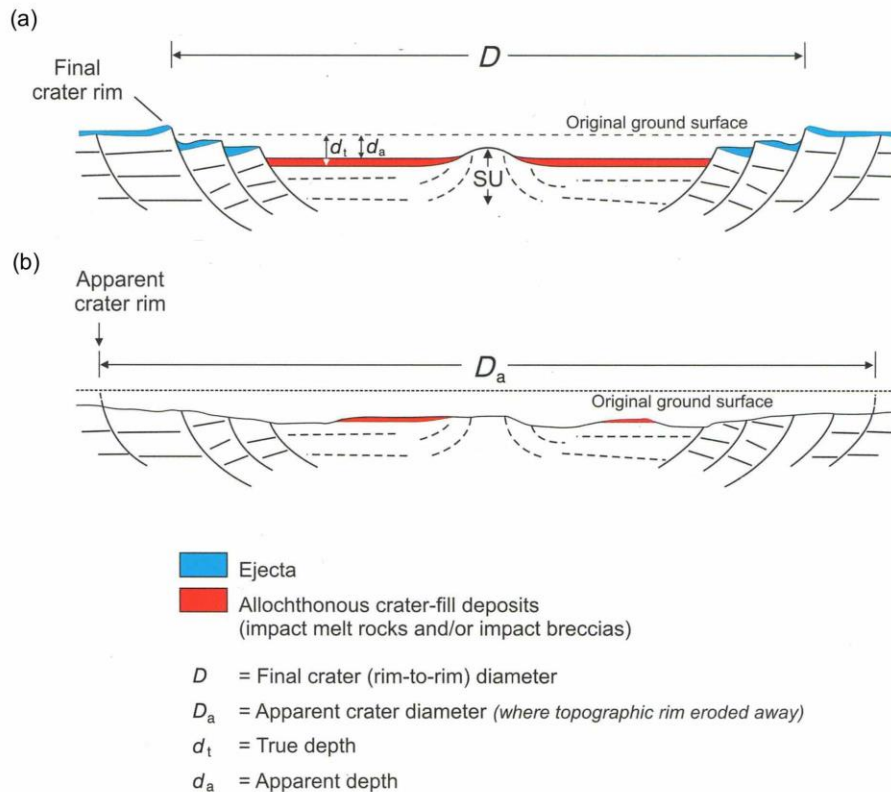


Figure 1.6. (a) Schematic cross-section showing the principal features of a complex impact crater. Note the structurally complicated rim, the down-faulted annular through, and the uplifted central area. (b) Schematic cross-section showing an eroded version of the fresh complex crater in (a). Note that in this case, only the apparent crater diameter can typically be defined. From Osinski and Pierazzo (2012).

1.5 Three stages of impact crater formation

1.5.1 Contact and compression stage

The contact and compression is the first stage of an impact event (Fig. 1.7). It begins with the impact of the target surface by a projectile (i.e., asteroid, comet) at supersonic speed, inducing pressures greater than 100 GPa (Shoemaker, 1960). The intense kinetic energy from the impact generates the propagation of compressional shock waves into the target sequence. Simultaneously, a concomitant series of shock waves propagate back into the projectile, and once the projectile's upper surface is reached, shock waves are reflected as rarefaction (tensional) waves (Ahrens and O'Keefe, 1972; Melosh, 1989). This results in the complete melting/vaporization of the projectile (Gault et al., 1968; Melosh, 1989). The combined kinetic energy of compressional and tensional waves induce shock metamorphism, melting and/or vaporization of the material located at the contact point of impact. The complete unloading of the projectile marks the end of this first stage of crater formation (Melosh, 1989).

1.5.2 Excavation stage

The contact and compression stage turns into the excavation stage as the interaction between the expanding shock waves and the original target surface leads to the opening of the impact crater (Fig. 1.7). It is important to note that the crater cavity is not excavated by the projectile itself, which has already been completely vaporized during the contact and compression stage (Melosh, 1989).

The propagation of hemispherical shock waves into the target sequence initiate the motion of material in an outward, radial trajectory. Furthermore, the interaction between the compressional outward-directed shock waves and the tensional downward-directed rarefaction waves create an "interference zone", within which the pressure peaks to its highest value (Melosh, 1989). This interference zone produces an "excavation flow-field", which generates the transient crater cavity (Dence, 1968; Grieve and Cintala, 1981). The latter is subdivided into an upper "excavated zone", and a lower "displaced zone". The excavated zone represents the upper one-third to one-half of the depth of the

transient crater cavity (Stöffler et al., 1975), and ejected material will comprise a range of shock levels. The displaced zone comprises the material that remains in the transient crater cavity, although some melt-rich material can be transported outside the cavity during a secondary episode of ejecta emplacement (Osinski et al., 2011). On the other hand, some of the melt and rock debris that were initially located stratigraphically below the contact point of impact remain in the transient crater cavity (Grieve et al., 1977) forming the crater-fill impactites.

1.5.3 Modification stage

The modification stage of crater formation is driven by two factors: the size of the transient crater cavity and the properties of the target rock lithologies (Melosh and Ivanov, 1999). For complex craters, the uplift of the crater floor, which induces the rise of the central uplift, and followed by the collapse of the crater walls, all occur during the modification stage (Fig. 1.7). No specific event marks the end of the modification stage (French, 1998). In fact, this stage is viewed as a continually perpetuating geological process, characterized by mass wasting movements, erosion, and other endogenous processes.

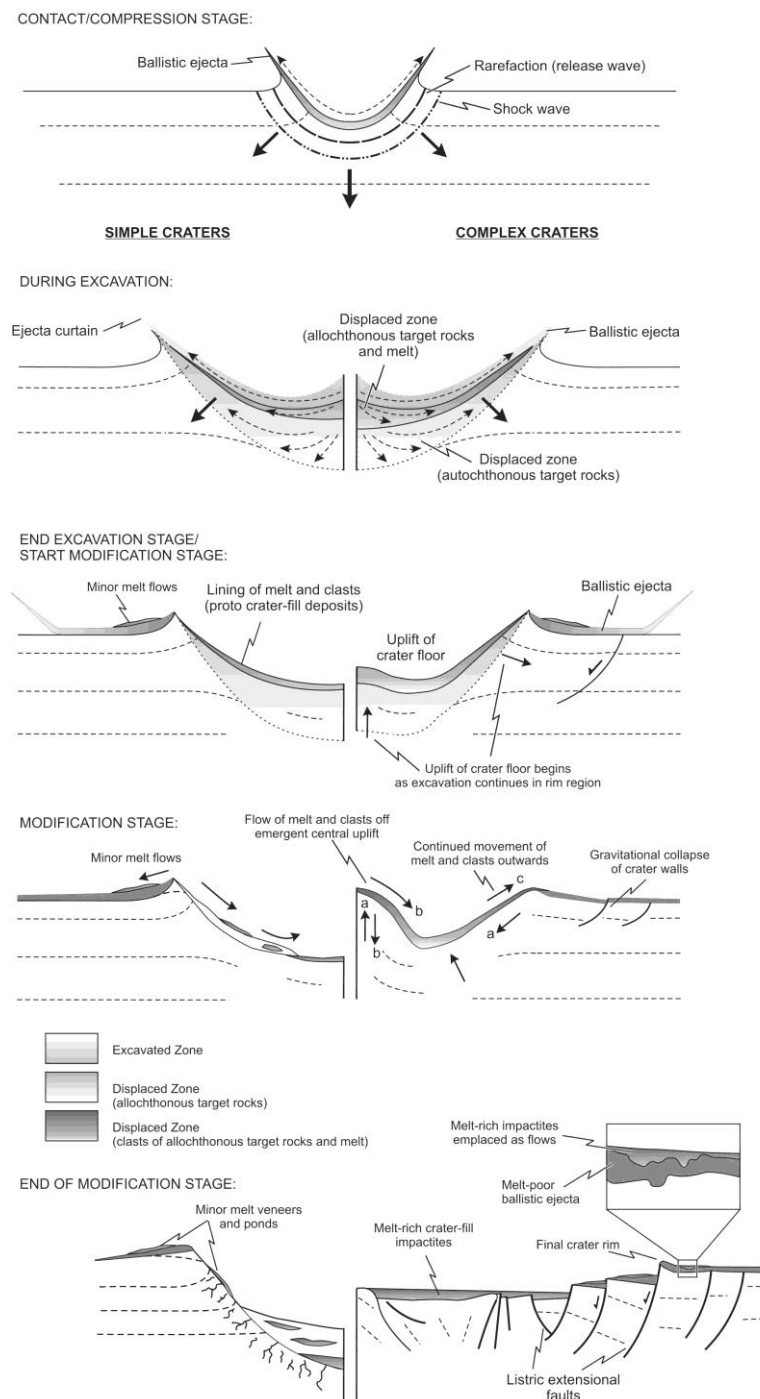


Figure 1.7. Series of schematic cross-section depicting the three main stages in the formation of both simple (left) and complex (right) craters. From Osinski and Pierazzo (2012).

1.6 Impactites

Impactites is the designation for rocks affected by, or produced by hypervelocity meteorite impact events (Stöffler and Grieve, 2007). Impactites can be classified into three main categories: shocked rocks, impact melt rocks, and impact breccias (Stöffler and Grieve, 2007). Shocked rocks are melt-free, have not been brecciated, and are the sole produce of shock metamorphism. Impact melt rocks are subclassified based on their clast content (i.e., clast-free, clast-poor, clast-rich) and/or degree of crystallinity (i.e., glassy, hypocrystalline or holocrystalline). Impact breccias vary depending on the incorporation of melt, and by the degree of mixing.

Impactites are also subdivided based on their displacement from their original pre-impact target location: autochthonous (formed in place), parautochthonous (moved but appear to be in place) and allochthonous (formed elsewhere and clearly moved to their current location) (Grieve and Therriault, 2004) (Fig. 1.8).

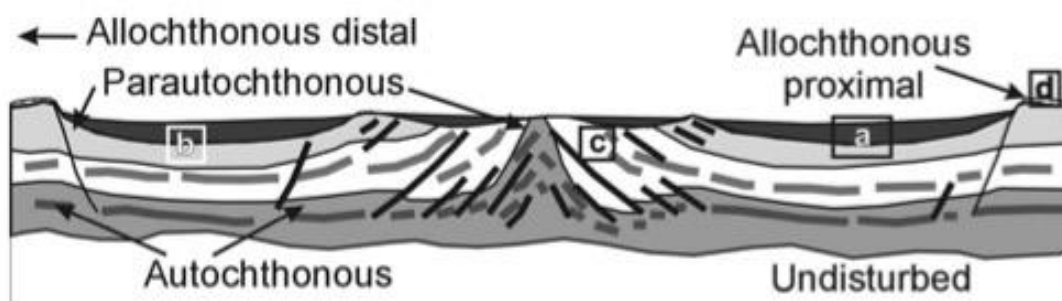


Figure 1.8. Schematic cross-section illustrating a small central peak based on terrestrial data, and the three types of impactites (autochthonous, parautochthonous, allochthonous). Black areas represent high concentration of either crater-fill impact melt rocks, melt-bearing breccias or lithic breccias. Small triangles represent lithic and melt-bearing breccias part of the ejecta. From Grieve and Therriault (2013).

1.7 References

- Acuña, M.H., Connerney, J.E.P., Ness, N.F., Lin, R.P., Mitchell, D., Carlson, C.W., McFadden, J., Anderson, K.A., Reme, H., Mazelle, C., Vignes, D., Wasilewski, P., Cloutier, P., 1999. Global Distribution of Crustal Magnetization Discovered by the Mars Global Surveyor MAG/ER Experiment. *Science*. 284, 790–793.
- Acuna, M.H., Connerney, J.E.P., Wasilewski, P., Lin, R.P., Anderson, K.A., Carlson, C.W., Mcfadden, J., Curtis, D.W., Mitchell, D., Reme, H., Mazelle, C., Sauvaud, J.A., Uston, C., Cros, A., Medale, J.L., Bauer, S.J., Cloutier, P., Mayhew, M., Winterhalter, D., Ness, N.F., 1998. Magnetic Field and Plasma Observations at Mars : Initial Results of the Mars Global Surveyor Mission. *Science*. 279, 1676–1680.
- Acuña, M.H., Connerney, J.E.P., Wasilewski, P., Lin, R.P., Mitchell, D., Anderson, K.A., Carlson, C.W., McFadden, J., Rème, H., Mazelle, C., Vignes, D., Bauer, S.J., Cloutier, P., Ness, N.F., 2001. Magnetic field of Mars: Summary of results from the aerobraking and mapping orbits. *J. Geophys. Res.* 106, 23,403–23,417.
- Ahrens, T.J., O’Keefe, J.D., 1972. Shock melting and vaporization of lunar rocks and minerals, *The Moon*. 214-219.
- Arvidson, R.E., Poulet, F., Bibring, J.-P., Wolff, M., Gendrin, A., Morris, R.V., Freeman, J.J., Langevin, Y., Mangold, N., Bellucci, G., 2005. Spectral Reflectance and Morphologic Correlations in Eastern Terra Meridiani, Mars. *Science*. 307, 1591–1594.
- Baker, V.R., Carr, M.H., Gulick, V.C., Williams, C.R., Marley, M.S., 1992. Channels and valley networks, in: *Mars*. 493–522.
- Baker, V.R., Maruyama, S., Dohm, J.M., 2007. Tharsis Superplume and the Geological Evolution of Early Mars, in: *Superplumes: Beyond Plate Tectonics*. 507–522.

- Balme, M., Mangold, N., Baratoux, D., Costard, F., Gosselin, M., Masson, P., Pinet, P., Neukum, G., 2006. Orientation and distribution of recent gullies in the southern hemisphere of Mars: Observations from High Resolution Stereo Camera/Mars Express (HRSC/MEX) and Mars Orbiter Camera/Mars Global Surveyor (MOC/MGS) data. *J. Geophys. Res.* 111, 1–20.
- Bandfield, J.L., Glotch, T.D., Christensen, P.R., 2003. Spectroscopic identification of carbonates in the Martian dust. *Science*. 301, 1084-1087.
- Bandfield, J.L., Hamilton, V.E., Christensen, P.R., 2000. A Global View of Martian Surface Compositions from MGS-TES. *Science*. 287, 1626–1630.
- Bibring, J.-P., Langevin, Y., Gendrin, A., Gondet, B., Poulet, F., Berthé, M., Soufflot, A., Arvidson, R.E., Mangold, N., Mustard, J.F., Drossart, P., Team, O., 2005. Mars Surface Diversity as Revealed by the OMEGA/Mars Express Observations. *Science*. 307, 1576–1581.
- Bibring, J.-P., Langevin, Y., Mustard, J.F., Poulet, F., Arvidson, R.E., Gendrin, A., Gondet, B., Mangold, N., Pinet, P., Forget, F., Berthé, M., Gomez, C., Jouglet, D., Soufflot, A., Vincendon, M., Combes, M., Drossart, P., Encrenaz, T., Fouchet, T., Merchiorri, R., Belluci, G., Altieri, F., Formisano, V., Capaccioni, F., Cerroni, P., Coradini, A., Fonti, S., Korablev, O., Kottsov, V., Ignatiev, N., Moroz, V., Titov, D., Zasova, L., Loiseau, D., Pinet, P., Douté, S., Schmitt, B., Sotin, C., Hauber, E., Hoffmann, H., Jaumann, R., Keller, H.U., Arvidson, R.E., Duxbury, T.C., Forget, F., Neukum, G., Team, O., 2006. Global Mineralogical and Aqueous Mars History Derived from OMEGA/Mars Express Data. *Science*. 312, 400–404.
- Boyce, J.M., Garbeil, H., 2007. Geometric relationships of pristine Martian complex impact craters, and their implications to Mars geologic history. *Geophys. Res. Lett.* 34, 1–5.

- Brain, D.A., Jakosky, B.M., 1998. Atmospheric loss since the onset of the Martian geologic record: Combined role of impact erosion and sputtering. *J. Geophys. Res.* 103, 22,689–22,694.
- Bridges, N.T., Lackner, C.N., 2006. Northern hemisphere Martian gullies and mantled terrain: Implications for near-surface water migration in Mars' recent past. *J. Geophys. Res.* 111, 1–10.
- Carr, M.H., 1995. The Martian drainage system and the origin of valley networks and fretted channels. *J. Geophys. Res.* 100, 7479–7507.
- Carr, M.H., 2006. *The Surface of Mars*. Cambridge University Press. 322 pp.
- Carr, M.H., Clow, G.D., 1981. Martian channels and valleys: Their characteristics, distribution, and age. *Icarus*. 48, 91–117.
- Carr, M.H., Head, J.W., 2010. Geologic history of Mars. *Earth Planet. Sci. Lett.* 294, 185–203.
- Carter, J., Poulet, F., Bibring, J.-P., Murchie, S.L., 2010. Detection of hydrated silicates in crustal outcrops in the northern plains of Mars. *Science*. 328, 1682–1686.
- Caudill, C.M., Tornabene, L.L., McEwen, A.S., Byrne, S., Ojha, L., Mattson, S., 2012. Layered MegaBlocks in the central uplifts of impact craters. *Icarus*. 221, 710–720.
- Christensen, P.R., Bandfield, J.L., Hamilton, V.E., Ruff, S.W., Kieffer, H.H., Titus, T.N., Malin, M.C., Morris, R.V., Lane, M.D., Clark, R.L., Jakosky, B.M., Mellon, M.T., Pearl, J.C., Conrath, B.J., Smith, M.D., Clancy, R.T., Kuzmin, R.O., Roush, T., Mehall, G.L., Gorelick, N., Bender, K., Murray, K., Dason, S., Greene, E., Silverman, S., Greenfield, M., 2001. Mars Global Surveyor Thermal Emission Spectrometer experiment: Investigation description and surface science results. *J. Geophys. Res.* 106, 23,823–23,871.

- Christensen, P.R., Bandfield, J.L., Smith, M.D., Hamilton, V.E., Clark, R.N., 2000. Identification of a basaltic component on the Martian surface from Thermal Emission Spectrometer data. *J. Geophys. Res.* 105, 9609–9621.
- Christensen, P.R., Jakosky, B.M., Kieffer, H.H., Malin, M.C., McSween, H.Y., Nealon, K., Mehall, G.L., Silverman, S.H., Ferry, S., Caplinger, M.A., Ravine, M.A., 2004. The thermal emission imaging system (THEMIS) for the Mars 2001 Odyssey mission. *Space Sci. Rev.* 110, 85–130.
- Chuang, F.C., Crown, D.A., 2009. Geologic map of MTM 35337, 40337, and 45337 quadrangles, Deuteronilus Mensae region of Mars. *US Dep. Inter. Geol. Surv.*
- Connerney, J.E.P., Acuña, M.H., Wasilewski, P.J., Kletetschka, G., Ness, N.F., Rème, H., Lin, R.P., Mitchell, D.L., 2001. The Global Magnetic Field of Mars and Implications for Crustal Evolution. *Geophys. Res. Lett.* 28, 4015–4018.
- Craddock, R.A., Howard, A.D., 2002. The case for rainfall on a warm, wet early Mars. *J. Geophys. Res.* 107, 21–36.
- Craddock, R.A., Maxwell, T.A., 1993. Geomorphic Evolution of the Martian Highlands through Ancient Fluvial Processes. *J. Geophys. Res.* 98, 3453–3468.
- Davila, A.F., Fairén, A.G., Stokes, C.R., Platz, T., Rodriguez, A.P., Lacelle, D., Dohm, J., Pollard, W., 2013. Evidence for Hesperian glaciation along the Martian dichotomy boundary. *Geology.* 41, 755–758.
- Dence, M.R., 1968. Shock zoning at Canadian craters: Petrography and structural implications. *Contrib. from Dom. Astrophys. Obs. Victoria* 8.
- Dickson, J.L., Head, J., Marchant, D.R., 2008. Late Amazonian glaciation at the dichotomy boundary on Mars: Evidence for glacial thickness maxima and multiple glacial phases. *Geology.* 36, 411–414.

- Dickson, J.L., Head, J.W., 2009. The formation and evolution of youthful gullies on Mars: Gullies as the late-stage phase of Mars' most recent ice age. *Icarus*. 204, 63–86.
- Dickson, J.L., Head, J.W., Kreslavsky, M., 2007. Martian gullies in the southern mid-latitudes of Mars: Evidence for climate-controlled formation of young fluvial features based upon local and global topography. *Icarus*. 188, 315–323.
- Ding, N., Bray, V.J., McEwen, A.S., Mattson, S.S., Okubo, C.H., Chojnacki, M., Tornabene, L.L., 2015. The central uplift of Ritchey crater, Mars. *Icarus*. 252, 255–270.
- Dohm, J.M., Baker, V.R., Boynton, W. V., Fairén, A.G., Ferris, J.C., Finch, M., Furfaro, R., Hare, T.M., Janes, D.M., Kargel, J.S., Karunatillake, S., Keller, J., Kerry, K., Kim, K.J., Komatsu, G., Mahaney, W.C., Schulze-Makuch, D., Marinangeli, L., Ori, G.G., Ruiz, J., Wheelock, S.J., 2009. GRS evidence and the possibility of paleooceans on Mars. *Planet. Space Sci.* 57. 664–684.
- Ehlmann, B., Mustard, J.F., Swayze, G. a., Clark, R.N., Bishop, J.L., Poulet, F., Des Marais, D.J., Roach, L.H., Milliken, R.E., Wray, J.J., Barnouin-Jha, O., Murchie, S.L., 2009. Identification of hydrated silicate minerals on Mars using MRO-CRISM: Geologic context near Nili Fossae and implications for aqueous alteration. *J. Geophys. Res. E Planets*. 114, 1–33.
- Ehlmann, B.L., Mustard, J.F., Murchie, S.L., Bibring, J.-P., Meunier, A., Fraeman, A.A., Langevin, Y., 2011. Subsurface water and clay mineral formation during the early history of Mars. *Nature*. 479, 53–60.
- Ehlmann, B.L., Mustard, J.F., Murchie, S.L., Poulet, F., Bishop, J.L., Brown, A.J., Calvin, W.M., Clark, R.N., Des Marais, D.J., Milliken, R.E., Roach, L.H., Roush, T.L., Swayze, G.A., Wray, J.J., 2008. Orbital identification of carbonate-bearing rocks on Mars. *Science*. 322, 1828–1832.

- Fairén, A.G., Davila, A.F., Gago-Duport, L., Haqq-Misra, J.D., Gil, C., McKay, C.P., Kasting, J.F., 2011. Cold glacial oceans would have inhibited phyllosilicate sedimentation on early Mars. *Nat. Geosci.* 4, 667–670.
- Fassett, C.I., Head, J.W., 2008. The timing of martian valley network activity: Constraints from buffered crater counting. *Icarus.* 195, 61–89.
- Fassett, C.I., Head, J.W., 2011. Sequence and timing of conditions on early Mars. *Icarus.* 211, 1204–1214.
- Flahaut, J., Mustard, J.F., Quantin, C., Clenet, H., Allemand, P., Thomas, P., 2011. Dikes of distinct composition intruded into Noachian-aged crust exposed in the walls of Valles Marineris. *Geophys. Res. Lett.* 38, 1–7.
- French, B.M., 1998. *Traces of Catastrophe A Handbook of Shock-Metamorphic Effects in Terrestrial Meteorite Impact Structures.* Lunar and Planetary Institute, Houston. 120 pp.
- Frey, H., Schultz, R.A., 1988. Large impact basins and the mega-impact origin for the crustal dichotomy on Mars. *Geophys. Res. Lett.* 15, 229–232.
- Garvin, J.B., Frawley, J.J., 1998. Geometric properties of Martian impact craters: Preliminary results from the Mars Orbiter Laser Altimeter. *Geophys. Res. Lett.* 25, 4405–4408.
- Gault, D.E., Quaide, W.L., Oberbeck, V.R., 1968. Impact cratering mechanics and structures. *A Prim. Lunar Geol.* 1, 177–189.
- Gendrin, A., Mangold, N., Bibring, J.-P., Langevin, Y., Gondet, B., Poulet, F., Bonello, G., Quantin, C., Mustard, J., Arvidson, R., LeMouélic, S., 2005. Sulfates in Martian layered terrains: the OMEGA/Mars Express view. *Science.* 307, 1587–1591.
- Golombek, M.P., Grant, J. A., Crumpler, L.S., Greeley, R., Arvidson, R.E., Bell, J.F., Weitz, C.M., Sullivan, R.J., Christensen, P.R., Soderblom, L. A., Squyres, S.W.,

2006. Erosion rates at the Mars Exploration Rover landing sites and long-term climate change on Mars. *J. Geophys. Res.* 111, 1–14.
- Gouge, T.A., Head, J.W., Mustard, J.F., Fassett, C.I., 2012. An analysis of open-basin lake deposits on Mars: Evidence for the nature of associated lacustrine deposits and post-lacustrine modification processes. *Icarus*. 219, 211–229.
- Gouge, T.A., Head, J.W., Mustard, J.F., Fassett, C.I., 2014. A transported origin for alteration minerals within the Jezero Crater, Mars paleolake basin: evidence from catchment and delta mineralogy, in: 45th Lunar Planet. Sci. Conf. Abstract #1164.
- Greeley, R., Guest, J., 1987. Geologic map of the eastern equatorial region of Mars. US Geological Survey.
- Greeley, R., Schneid, B.D., 1991. Magma generation on Mars: amounts, rates, and comparisons with Earth, moon, and venus. *Science*. 254, 996–998.
- Greeley, R., Spudis, P.D., 1981. Volcanism on Mars. *Rev. Geophys. Sp. Phys.* 19, 13–41.
- Grieve, R.A.F., Therriault, A., 2004. Observations at terrestrial impact structures: Their utility in constraining crater formation. *Meteorit. Planet. Sci.* 39, 199–216.
- Grieve, R.A.F., 2012. Economic deposits at terrestrial impact structures, in *Impact Cratering: Processes and Products*. John Wiley & Sons, Chichester.
- Grieve, R.A.F., Cintala, M.J., 1981. A method for estimating the initial impact conditions of terrestrial cratering events, exemplified by its application to Brent crater, Ontario, in: 12th Lunar Planet. Sci. Conf. 1607–1621.
- Grieve, R.A.F., Dence, M.R., Robertson, P.B., 1977. Cratering processes: As interpreted from the occurrences of impact melts. *Impact Explos. Cratering Planet. Terr. Implic.* 1, 791–814.
- Grieve, R.A.F., Pilkington, M., 1996. The signature of terrestrial impacts. *AGSO J. Aust. Geol. Geophys.* 16, 399–420.

- Grieve, R.A.F., Therriault, A.M., 2013. Impactites: Their characteristics and spatial distribution. *Impact cratering Process. Prod.* 90–105.
- Griffith, L.L., Shock, E.L., 1997. Hydrothermal hydration of Martian crust: illustration via geochemical model calculations. *J. Geophys. Res.* 102, 9135–9143.
- Hartmann, W.K., Neukum, G., 2001. Cratering chronology and the evolution of Mars. *Spcae Sci. Rev.* 96, 165–194.
- Hauber, E., Brož, P., Jagert, F., Jodowski, P., Platz, T., 2011. Very recent and widespread basaltic volcanism on Mars. *Geophys. Res. Lett.* 38, 1–5.
- Head, J.W., Kreslavsky, M.A., Pratt, S., 2002. Northern lowlands of Mars: Evidence for widespread volcanic flooding and tectonic deformation in the Hesperian Period. *J. Geophys. Res.* 107, 3–1.
- Head, J.W., Pratt, S., 2001. Extensive Hesperian-aged south polar ice sheet on Mars: Evidence for massive melting and retreat, and lateral flow and ponding of meltwater. *J. Geophys. Res.* 106, 12,275–12,299.
- Herkenhoff, K.E., Plaut, J.J., 2000. Surface Ages and Resurfacing Rates of the Polar Layered Deposits on Mars. *Icarus.* 144, 243–253.
- Hiller, K.H., 1979. Geologic map of the Amenthes quadrangle of Mars.
- Hoefen, T.M., Clark, R.N., Bandfield, J.L., Smith, M.D., Pearl, J.C., Christensen, P.R., 2003. Discovery of Olivine in the Nili Fossae Region of Mars. *Science.* 302, 627–630.
- Hoke, M.R.T., Hynek, B.M., 2009. Roaming zones of precipitation on ancient Mars as recorded in valley networks. *J. Geophys. Res.* 114, 1–22.
- Howard, A.D., Moore, J.M., Irwin, R.P., 2005. An intense terminal epoch of widespread fluvial activity on early Mars: 1. Valley network incision and associated deposits. *J. Geophys. Res.* 110, 1–20.

- Hynek, B.M., 2003. Explosive volcanism in the Tharsis region: Global evidence in the Martian geologic record. *J. Geophys. Res.* 108, 1–16.
- Hynek, B.M., Beach, M., Hoke, M.R.T., 2010. Updated global map of Martian valley networks and implications for climate and hydrologic processes. *J. Geophys. Res.* 115, 1–14.
- Hynek, B.M., Phillips, R.J., 2001. Evidence for extensive denudation of the Martian highlands. *Geology*. 29, 407–410.
- Irwin, R.P., Craddock, R.A., Howard, A.D., 2005. Interior channels in Martian valley networks: Discharge and runoff production. *Geology*. 33, 489–492.
- Ivanov, B.A., 2001. Mars/Moon cratering rate ratio estimates, in: *Chronology and Evolution of Mars*. Springer, 87–104.
- Jakosky, B.M., 2011. The 2013 Mars atmosphere and volatile evolution (MAVEN) mission to Mars, in: *AGU Fall Meeting Abstracts*. p. 1.
- Kargel, J.S., Baker, V.R., Beget, J.E., Lockwood, J.F., Pewe, T.L., Shaw, J., Strom, R.G., 1995. Evidence of ancient continental glaciation in the Martian northern plains. *J. Geophys. Res.* 100, 5351–5368.
- Kargel, J.S., Strom, R.G., 1992. Ancient glaciation on Mars. *Geology*. 20, 3–7.
- Kenkmann, T., Jahn, A., Scherler, D., Ivanov, B.A., 2005. Structure and formation of a central uplift: A case study at the Upheaval Dome impact crater, Utah. *Geol. Soc. Am. Spec. Pap.* 384, 85–115.
- Kieffer, H.H., 1979. Mars south polar spring and summer temperatures : A residual CO₂ frost. *J. Geophys. Res.* 84, 8263–8288.
- Kieffer, H.H., Chase, S.C., Martin, T.Z., Miner, E.D., Palluconi, F.D., 1976. Martian North Pole Summer Temperatures: Dirty Water Ice. *Science*. 194, 1341–1344.

- Kieffer, H.H., Jakosky, B.M., Snyder, C.W., 1992. The planet Mars-From antiquity to the present, in: Mars. 1-33.
- Kieffer, H.H., Martin, T.Z., Peterfreund, A.R., Jakosky, B.M., 1977. Thermal and Albedo Mapping of Mars During the Viking Primary Mission. *J. Geophys. Res.* 82, 4249–4291.
- Kreslavsky, M. A., 2002. Fate of outflow channel effluents in the northern lowlands of Mars: The Vastitas Borealis Formation as a sublimation residue from frozen ponded bodies of water. *J. Geophys. Res.* 107, 5121.
- Langevin, Y., Poulet, F., Bibring, J.-P., Gondet, B., 2005. Sulfates in the north polar region of Mars detected by OMEGA/Mars Express. *Science.* 307, 1584–1586.
- Lenardic, A., Nimmo, F., Moresi, L., 2004. Growth of the hemispheric dichotomy and the cessation of plate tectonics on Mars. *J. Geophys. Res.* 109, 1–14.
- Loizeau, D., Carter, J., Bouley, S., Mangold, N., Poulet, F., Bibring, J.-P., Costard, F., Langevin, Y., Gondet, B., Murchie, S.L., 2012. Characterization of hydrated silicate-bearing outcrops in Tyrrhena Terra, Mars: Implications to the alteration history of Mars. *Icarus.* 219, 476–497.
- Loizeau, D., Mangold, N., Poulet, F., Ansan, V., Hauber, E., Bibring, J.-P., Gondet, B., Langevin, Y., Masson, P., Neukum, G., 2010. Stratigraphy in the Mawrth Vallis region through OMEGA, HRSC color imagery and DTM. *Icarus.* 205, 396–418.
- Loizeau, D., Mangold, N., Poulet, F., Bibring, J.-P., Gendrin, A., Ansan, V., Gomez, C., Gondet, B., Langevin, Y., Masson, P., Neukum, G., 2007. Phyllosilicates in the Mawrth Vallis region of Mars. *J. Geophys. Res.* 112, 1–20.
- Lucchitta, B., 1981. Mars and Earth: Comparison of cold-climate features. *Icarus.* 45, 264–303.

- Mangold, N., Quantin, C., Ansan, V., Delacourt, C., Allemand, P., 2004. Evidence for precipitation on Mars from dendritic valleys in the Valles Marineris area. *Science*. 305, 78–81.
- Marzo, G.A., Davila, A.F., Tornabene, L.L., Dohm, J.M., Fairén, A.G., Gross, C., Kneissl, T., Bishop, J.L., Roush, T.L., McKay, C.P., 2010. Evidence for Hesperian impact-induced hydrothermalism on Mars. *Icarus*. 208, 667–683.
- McEwen, A.S., Malin, M.C., Carr, M.H., Hartmann, W.K., 1999. Voluminous volcanism on early Mars revealed in Valles Marineris. *Nature*. 397, 584–586.
- McGill, G.E., 2002. Geologic map transecting the highland/lowland boundary zone, Arabia Terra, Mars; quadrangles 30332, 35332, 40332, and 45332. US Geol. Surv.
- McGill, G.E., 2005. Geologic Map of Cydonia Mensae-Southern Acidalia Planitia, Mars, Quadrangles MTM 40007, 40012, 40017, 45007, 45012, and 45017. US Dep. Inter. US Geol. Surv.
- McGill, G.E., Dimitriou, A.M., 1990. Origin of the Martian Global Dichotomy by Crustal Thinning in the Late Noachian or Early Hesperian. *J. Geophys. Res.* 95, 12,595–12,605.
- McSween, H.Y., Treiman, A.H., 1998. Martian meteorites. *Rev. Mineral. Geochemistry* 36, 1–6.
- Melosh, H.J., 1989. *Impact Cratering A Geologic Process*. Oxford University Press, New York. 245 pp.
- Melosh, H.J., Ivanov, B.A., 1999. Impact Crater Collapse. *Annu. Rev. Earth Planet. Sci.* 27, 385–415.
- Michalski, J.R., Niles, P.B., 2010. Deep crustal carbonate rocks exposed by meteor impact on Mars. *Nat. Geosci.* 3, 751–755.

- Milliken, R.E., Swayze, G.A., Arvidson, R.E., Bishop, J.L., Clark, R.N., Ehlmann, B.L., Green, R.O., Grotzinger, J.P., Morris, R.V., Murchie, S.L., Mustard, J.F., Weitz, C., 2008. Opaline silica in young deposits on Mars. *Geology*. 36, 847–850.
- Montgomery, D.R., Som, S.M., Jackson, M.P.A., Schreiber, B.C., Gillespie, A.R., Adams, J.B., 2009. Continental-scale salt tectonics on Mars and the origin of Valles Marineris and associated outflow channels. *Geol. Soc. Am. Bull.* 121, 117–133.
- Murchie, S., Arvidson, R., Bedini, P., Beisser, K., Bibring, J.-P., Bishop, J., Boldt, J., Cavender, P., Choo, T., Clancy, R.T., Darlington, E.H., Des Marais, D., Espiritu, R., Fort, D., Green, R., Guinness, E., Hayes, J., Hash, C., Heffernan, K., Hemmler, J., Heyler, G., Humm, D., Hutcheson, J., Izenberg, N., Lee, R., Lees, J., Lohr, D., Malaret, E., Martin, T., McGovern, J.A., McGuire, P., Morris, R., Mustard, J., Pelkey, S., Rhodes, E., Robinson, M., Roush, T., Schaefer, E., Seagrave, G., Seelos, F., Silverglate, P., Slavney, S., Smith, M., Shyong, W.-J., Strohhahn, K., Taylor, H., Thompson, P., Tossman, B., Wirzburger, M., Wolff, M., 2007. Compact Reconnaissance Imaging Spectrometer for Mars (CRISM) on Mars Reconnaissance Orbiter (MRO). *J. Geophys. Res.* 112, 1–57.
- Murchie, S.L., Mustard, J.F., Ehlmann, B.L., Milliken, R.E., Bishop, J.L., McKeown, N.K., Noe Dobrea, E.Z., Seelos, F.P., Buczkowski, D.L., Wiseman, S.M., Arvidson, R.E., Wray, J.J., Swayze, G., Clark, R.N., Des Marais, D.J., McEwen, A.S., Bibring, J.-P., 2009. A synthesis of Martian aqueous mineralogy after 1 Mars year of observations from the Mars Reconnaissance Orbiter. *J. Geophys. Res.* 114, 1–30.
- Mustard, J.F., Ehlmann, B.L., Murchie, S.L., Poulet, F., Mangold, N., Head, J.W., Bibring, J.-P., Roach, L.H., 2009. Composition, Morphology, and Stratigraphy of Noachian Crust around the Isidis basin. *J. Geophys. Res.* 114, 1–18.
- Mustard, J.F., Murchie, S.L., Pelkey, S.M., Ehlmann, B.L., Milliken, R.E., Grant, J.A., Bibring, J.-P., Poulet, F., Bishop, J., Dobrea, E.N., Roach, L., Seelos, F., Arvidson, R.E., Wiseman, S., Green, R., Hash, C., Humm, D., Malaret, E., McGovern, J.A., Seelos, K., Clancy, T., Clark, R., Marais, D.D., Izenberg, N., Knudson, A.,

- Langevin, Y., Martin, T., McGuire, P., Morris, R., Robinson, M., Roush, T., Smith, M., Swayze, G., Taylor, H., Titus, T., Wolff, M., 2008. Hydrated silicate minerals on Mars observed by the Mars Reconnaissance Orbiter CRISM instrument. *Nature*. 454, 305–309.
- Neukum, G., Basilevsky, A.T., Kneissl, T., Chapman, M.G., van Gasselt, S., Michael, G., Jaumann, R., Hoffmann, H., Lanz, J.K., 2010. The geologic evolution of Mars: Episodicity of resurfacing events and ages from cratering analysis of image data and correlation with radiometric ages of Martian meteorites. *Earth Planet. Sci. Lett.* 294, 204–222.
- Neukum, G., Jaumann, R., Team, H.C.-I. and E., 2004. HRSC : the High Resolution Stereo Camera of Mars Express. *Mars Express Sci. payload* 17–35.
- Neumann, G.A., Rowlands, D.D., Lemoine, F.G., Smith, D.E., Zuber, M.T., 2001. Crossover analysis of Mars Orbiter Laser Altimeter data. *J. Geophys. Res.* 106, 23,753–23,768.
- Nimmo, F., Tanaka, K.L., 2005. Early Crustal Evolution of Mars. *Annu. Rev. Earth Planet. Sci.* 33, 133–161.
- Nyquist, L.E., Bogard, D.D., Shih, C.-Y., Greshake, A., Stöffler, D., Eugster, O., 2001. Ages and geologic histories of Martian meteorites, in: *Chronology and Evolution of Mars*. Springer, 105–164.
- Osinski, G.R., Pierazzo, E., 2012. *Impact cratering: Processes and products*. John Wiley & Sons. 330 pp.
- Osinski, G.R., Tornabene, L.L., Banerjee, N.R., Cockell, C.S., Flemming, R., Izawa, R.M., McCutcheon, J., Parnell, J., Preston, L.J., Pickersgill, A.E., Pontefract, A., Sapers, H.M., Southam, G., 2013. Impact-generated hydrothermal systems on Earth and Mars. *Icarus*. 224, 347–363.

- Osinski, G.R., Tornabene, L.L., Grieve, R.A.F., 2011. Impact ejecta emplacement on terrestrial planets. *Earth Planet. Sci. Lett.* 310, 167–181.
- Owen, T., 1992. The composition and early history of the atmosphere of Mars. *Mars* 1, 818–834.
- Pan, C., Rogers, A.D., Michalski, J.R., 2015. Thermal and near-infrared analyses of central peaks of Martian impact craters: Evidence for a heterogeneous Martian crust. *J. Geophys. Res.* 120, 662–688.
- Phillips, R.J., Zuber, M.T., Solomon, S.C., Golombek, M.P., Jakosky, B.M., Banerdt, W.B., Smith, D.E., Williams, R.M., Hynes, B.M., Aharonson, O., Hauck, S.A., 2001. Ancient geodynamics and global-scale hydrology on Mars. *Science*. 291, 2587–2591.
- Pike, R.J., 1980a. Formation of Complex Impact Craters : Evidence from Mars and Other Planets. *Icarus*. 43, 1–19.
- Pike, R.J., 1980b. Control of crater morphology by gravity and target type: Mars, Earth, Moon. *Proc. 11th Lunar Planet. Sci. Conf.* 11, 2159–2189.
- Platz, T., Michael, G., 2011. Eruption history of the Elysium Volcanic Province, Mars. *Earth Planet. Sci. Lett.* 312, 140–151.
- Plescia, J.B., 2004. Morphometric properties of Martian volcanoes. *J. Geophys. Res.* 109, 1–26.
- Poulet, F., Bibring, J.-P., Mustard, J.F., Gendrin, A., Mangold, N., Langevin, Y., Arvidson, R.E., Gondet, B., Gomez, C., Berthé, M., Erard, S., Forni, O., Manaud, N., Poulleau, G., Soufflot, A., Combes, M., Drossart, P., Encrenaz, T., Fouchet, T., Melchiorri, R., Bellucci, G., Altieri, F., Formisano, V., Fonti, S., Capaccioni, F., Cerroni, P., Coradini, A., Korablev, O., Kottsov, V., Ignatiev, N., Titov, D., Zasova, L., Pinet, P., Schmitt, B., Sotin, C., Hauber, E., Hoffmann, H., Jaumann, R., Keller, H.U., Forget, F., 2005. Phyllosilicates on Mars and implications for early martian

- climate. *Nature*. 438, 623–627.
- Quantin, C., Flahaut, J., Clenet, H., Allemand, P., Thomas, P., 2012. Composition and structures of the subsurface in the vicinity of Valles Marineris as revealed by central uplifts of impact craters. *Icarus*. 221, 436–452.
- Robbins, S.J., Hynek, B.M., 2012a. A new global database of Mars impact craters ≥ 1 km: 1. Database creation, properties, and parameters. *J. Geophys. Res. E Planets*. 117, 1–18.
- Robbins, S.J., Hynek, B.M., 2012b. A new global database of Mars impact craters ≥ 1 km: 2. Global crater properties and regional variations of the simple-to-complex transition diameter. *J. Geophys. Res.* 117, 1–21.
- Roberts, J.H., Zhong, S., 2004. Plume-induced topography and geoid anomalies and their implications for the Tharsis rise on Mars. *J. Geophys. Res.* 109, 1–7.
- Rogers, D.A., Christensen, P.R., Bandfield, J.L., 2005. Compositional heterogeneity of the ancient Martian crust: Analysis of Ares Vallis bedrock with THEMIS and TES data. *J. Geophys. Res.* 110, 1–26.
- Scott, D.H., 1978. Mars, Highlands-Lowlands : Viking Contributions to Mariner Relative Age Studies. *Icarus*. 34, 479–485.
- Scott, D.H., Carr, M.H., 1976. Geologic Map of Mars.
- Scott, D.H., King, J.S., 1984. Ancient surfaces of Mars: The basement complex, in: 15th Lunar Planet. Sci. Conf. 736–737.
- Scott, D.H., Tanaka, K.L., 1986. Geologic map of the western equatorial region of Mars. U.S. Geol. Surv.
- Segura, T.L., Toon, O.B., Colaprete, A., Zahnle, K., 2002. Environmental effects of large impacts on Mars. *Science*. 298, 1977–1980.

- Shoemaker, E.M., 1960. Penetration mechanics of high velocity meteorites, illustrated by Meteor Crater, Arizona, International Geological Congress. 21st Sess. part 18, 418–434.
- Skok, J.R., Mustard, J.F., Tornabene, L.L., Pan, C., Rogers, D.A., Murchie, S.L., 2012. A spectroscopic analysis of Martian crater central peaks: Formation of the ancient crust. *J. Geophys. Res.* 117, 1–33.
- Sleep, N.H., 1994. Martian plate tectonics. *J. Geophys. Res.* 99, 5639–5655.
- Smith, D.E., Zuber, M.T., Frey, H.V., Garvin, J.B., Head, J.W., Muhleman, D.O., Pettengill, G.H., Phillips, R.J., Solomon, S.C., Zwally, H.J., Banerdt, W.B., Duxbury, T.C., Golombek, M.P., Lemoine, F.G., Neumann, G.A., Rowlands, D.D., Aharonson, O., Ford, P.G., Ivanov, A.B., Johnson, C.L., McGovern, P.J., Abshire, J.B., Afzal, R.S., Sun, X., 2001. Mars Orbiter Laser Altimeter: Experiment summary after the first year of global mapping of Mars. *J. Geophys. Res.* 106, 23,689–23,722.
- Smith, D.E., Zuber, M.T., Solomon, S.C., Phillips, R.J., Head, J.W., Garvin, J.B., Banerdt, W.B., Muhleman, D.O., Pettengill, G.H., Neumann, G.A., Lemoine, F.G., Abshire, J.B., Aharonson, O., Brown, C.D., Hauck, S.A., Ivanov, A.B., McGovern, P.J., Zwally, H.J., Duxbury, T.C., 1999. The Global Topography of Mars and Implications for Surface Evolution. *Science.* 284, 1495–1503.
- Stewart, S.T., Valiant, G.J., 2006. Martian subsurface properties and crater formation processes inferred from fresh impact crater geometries. *Meteorit. Planet. Sci.* 41, 1509–1537.
- Stöffler, D., Gault, D.E., Wedekind, J., Polkowski, G., 1975. Experimental hypervelocity impact into quartz sand: Distribution and shock metamorphism of ejecta. *J. Geophys. Res.* 80, 4062–4077.
- Stöffler, D., Grieve, R.A.F., 2007. Impactites, Chapter 2.11 in Fettes D., Desmons., J. (eds.) *Metamorphic Rocks: A Classification and Glossary of Terms.*

- Recommendations of the International Union of Geological Sciences
Subcommission on the Systematics of Metamorphic Rocks. Cambridge University
Press, Cambridge. 82-92, 111-125, and 126-142.
- Strom, R., Croft, S., Barlow, N., 1992. The Martian impact cratering record, in Mars,
University of Arizona Press. Mars. pp. 383-423.
- Tanaka, K.L., 1986. The Stratigraphy of Mars. *J. Geophys. Res.* 91, 139–158.
- Tanaka, K.L., Isbell, N.K., Scott, D.H., Greeley, R., Guest, J.E., 1988. The resurfacing
history of Mars-A synthesis of digitized, viking-based geology, in: 18th Lunar
Planet. Sci. Conf. pp. 665–678.
- Tanaka, K.L., Robbins, S.J., Fortezzo, C.M., Skinner, J.A., Hare, T.M., 2014. The digital
global geologic map of Mars: Chronostratigraphic ages, topographic and crater
morphologic characteristics, and updated resurfacing history. *Planet. Space Sci.* 95,
11–24.
- Tanaka, K.L., Scott, D.H., 1987. Geologic map of the polar regions of Mars. *Surv.*
- Tanaka, K.L., Skinner, J.A., Hare, T.M., 2005. Geologic Map of the Northern Plains of
Mars.
- Tanaka, K.L., Skinner, J.A., Hare, T.M., Joyal, T., Wenker, A., 2003. Resurfacing history
of the northern plains of Mars based on geologic mapping of Mars Global Surveyor
data. *J. Geophys. Res.* 108, 1–32.
- Tornabene, L., Osinski, G.R., Barlow, N.G., Bray, V.J., Caudill, C.M., D'Aoust, B.,
Ding, N., Hopkins, R., Nuhn, A.M., Mayne, A., McEwen, A.S., 2015. Meter- to
decameter-scale characteristics of central uplifts revealed by the Mars
Reconnaissance Orbiter. *Bridg. Gap III.* 5–6.
- Tornabene, L.L., McEwen, A.S., Caudill, C., Osinski, G.R., Wray, J.J., Marzo, G.A.,
Mustard, J.F., Skok, J.R., 2010. A Crater-Exposed Bedrock Database for Mars With

Applications for Determining the Composition and Structure of the Upper Crust. in: 41st Lunar Planet. Sci. Conf. Abstract #1737.

Tornabene, L.L., Osinski, G.R., McEwen, A.S., Ling, V., Caudill, C.M., Nuhn, A., Hopkins, R., D'Aoust, B., Kasmai, B., Mattson, S., 2014. A Global Synthesis of the Meter- to Decameter-Scale Morphology and Structure of Complex Crater Central Uplifts. in: Eighth Int. Conf. Mars Abstract #1379.

Tornabene, L.L., Osinski, G.R., McEwen, A.S., Wray, J.J., Craig, M.A., Sapers, H.M., Christensen, P.R., 2013. An impact origin for hydrated silicates on Mars: A synthesis. *J. Geophys. Res. Planets.* 118, 994–1012.

Webb, B.M., Head III, J.W., 2002a. Terrestrial analogs for Noachian tectonics of the Tharsis rise and Thaumasia plateau, Mars, in: 33th Lunar Planet. Sci. Conf. Abstract # 1825.

Webb, B.M., Head III, J.W., 2002b. Noachian tectonics of Syria Planum and the Thaumasia Plateau, in: 33th Lunar Planet. Sci. Conf. Abstract # 1358.

Werner, S.C., 2009. The global martian volcanic evolutionary history. *Icarus.* 201, 44–68.

Wilhelms, D., Squyres, S., 1984. The martian hemispheric dichotomy may be due to a giant impact. *Nature.* 309, 138–140.

Wise, D.U., Golombek, M.P., McGill, G.E., 1979. Tectonic Evolution of Mars. *J. Geophys. Res.* 84, 7934–7939.

Wray, J.J., Ehlmann, B.L., Squyres, S.W., Mustard, J.F., Kirk, R.L., 2008. Compositional stratigraphy of clay-bearing layered deposits at Mawrth Vallis, Mars. *Geophys. Res. Lett.* 35, 1–6.

Zhong, S., Zuber, M.T., 2001. Degree-1 mantle convection and the crustal dichotomy on Mars. *Earth Planet. Sci. Lett.* 189, 75–84.

Chapter 2

2 Morphological, Structural and Spectral Mapping of the Central Uplift of Alga Crater, Ladon Basin, Mars

2.1 Introduction

Impact cratering is a ubiquitous geological process affecting and shaping the planetary bodies of the Solar System and beyond. Subsurface materials are exhumed and redistributed across the entire Martian surface due to impact cratering (Chapman and Jones, 1977; Barlow and Bradley, 1990). Central uplifts of complex craters hold a particular interest as they expose uplifted deep-seated bedrock, some of which may correspond to the oldest exposures of the early Martian crust (Tornabene et al., 2010, 2015; L.L. Tornabene et al., 2013).

Tornabene et al. (2010) compiled a global crater-exposed geodatabase using derived data from the Mars Reconnaissance Orbiter (MRO) and Mars Odyssey (MO) spacecrafts. Three distinct textural types of exposed bedrock have been documented at the metre- to decametre-scale High Resolution Imaging Science Experiment (HiRISE) images of ~200 complex craters on Mars (Tornabene et al., 2015): layered bedrock (LB), massive and fractured bedrock (MFB) and megabrecciated bedrock (MBB). From the observations by Tornabene et al. (2010), the bedrock in most central uplifts is generally not well-exposed due to obscuration by syn-impact deposits (e.g., impact melt rocks), post-impact deposits (e.g., dust, mass wasting deposits), and regionally derived materials (Tornabene et al., 2010, 2015; L.L. Tornabene et al., 2013; Osinski et al., 2013). Therefore, it is critical to recognize and distinguish pre-impact target rocks from impact-related and post-impact deposits by correlating morphological observations with composition. On the other hand, structural mapping can inform on pre-existing structures and pre-impact target properties (Tornabene et al., 2010). Thus, a synthesis of detailed mapping of impact craters using high-resolution imagery and spectral reflectance data within the context of the local and regional geology are key towards constraining the geological history of the various pre-, syn- and post-impact materials within the uplifts of Martian complex craters. In addition, it is important to note that central uplifts may be comprised of materials that resulted

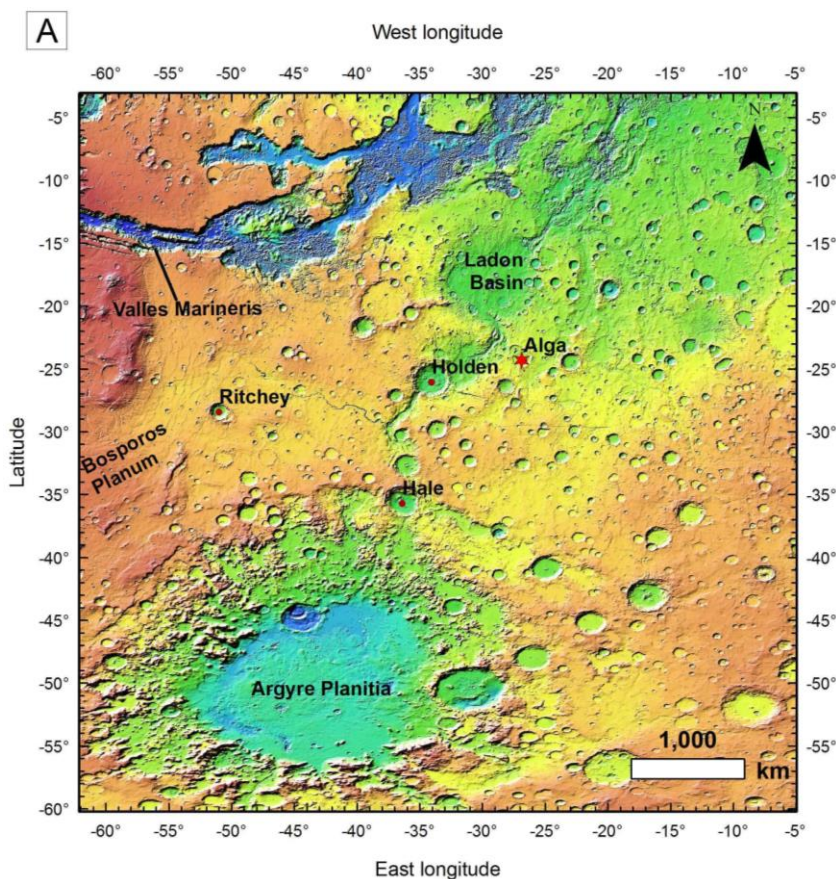
from multiple episodes of excavation and redistribution due to previous impact events (i.e., pre-impact events).

Field studies at terrestrial impact structures have provided many insights into the mechanics of central uplift formation (Osinski et al., 2005a; Kenkmann et al., 2014). However, the exposures of terrestrial central uplifts are sparse, particularly in the largest complex impact structures. Thus, a detailed study of well-exposed Martian central uplifts can provide a more complete view of their morphology and structure, and contribute to a better understanding of the impact cratering process and central uplift formation specifically.

This study focuses on the massive and fractured bedrock (MFB) exposed in the central uplift of the ~19 km diameter Alga Crater, which is located in the heavily cratered Southern Highlands of Mars almost equidistant between the Argyre Basin and Valles Marineris. We conducted detailed morphological, structural, and spectral mapping of Alga using HiRISE and CRISM datasets. Alga is a very well-exposed complex impact crater that was selected from the crater-exposed bedrock geodatabase compiled by Tornabene et al. (2010). By correlating detailed metre- to decametre-scale morphological and structural mapping with the compositional information from spectral reflectance data (in addition to supplemental datasets such as topography and thermophysical characteristics from thermal inertia data), we aim at better constraining the origin of the surface materials that can be observed in association with the central uplift of Alga Crater; this includes providing insights into: 1) the nature of the exposed bedrock (i.e., the massive and fractured bedrock class), 2) the type(s) and timing of emplacement of impactites, and 3) the formation of central uplifts in massive target rocks.

2.2 General Geological Setting: Alga Crater

Alga Crater (333.3 °E, 24.3 °S) is a ~19 km diameter well-exposed nearly circular complex impact crater situated in western Noachis Terra (Fig. 2.1A). It occurs within the Middle Noachian highland unit (mNh), which is interpreted as undifferentiated impact, volcanic, fluvial and basin materials that are moderately to heavily degraded (Tanaka et al., 2014). Alga occurs in an area of Noachis Terra that is bound to the northwest by Valles Marineris and by the multi-ringed Argyre Basin to the southwest (Fig. 2.1A). Regionally, Alga is located within the ~88 km diameter Chekalin Crater, which in turn is superposed on the outer rings of the ancient Ladon Basin (Fig. 2.1B).



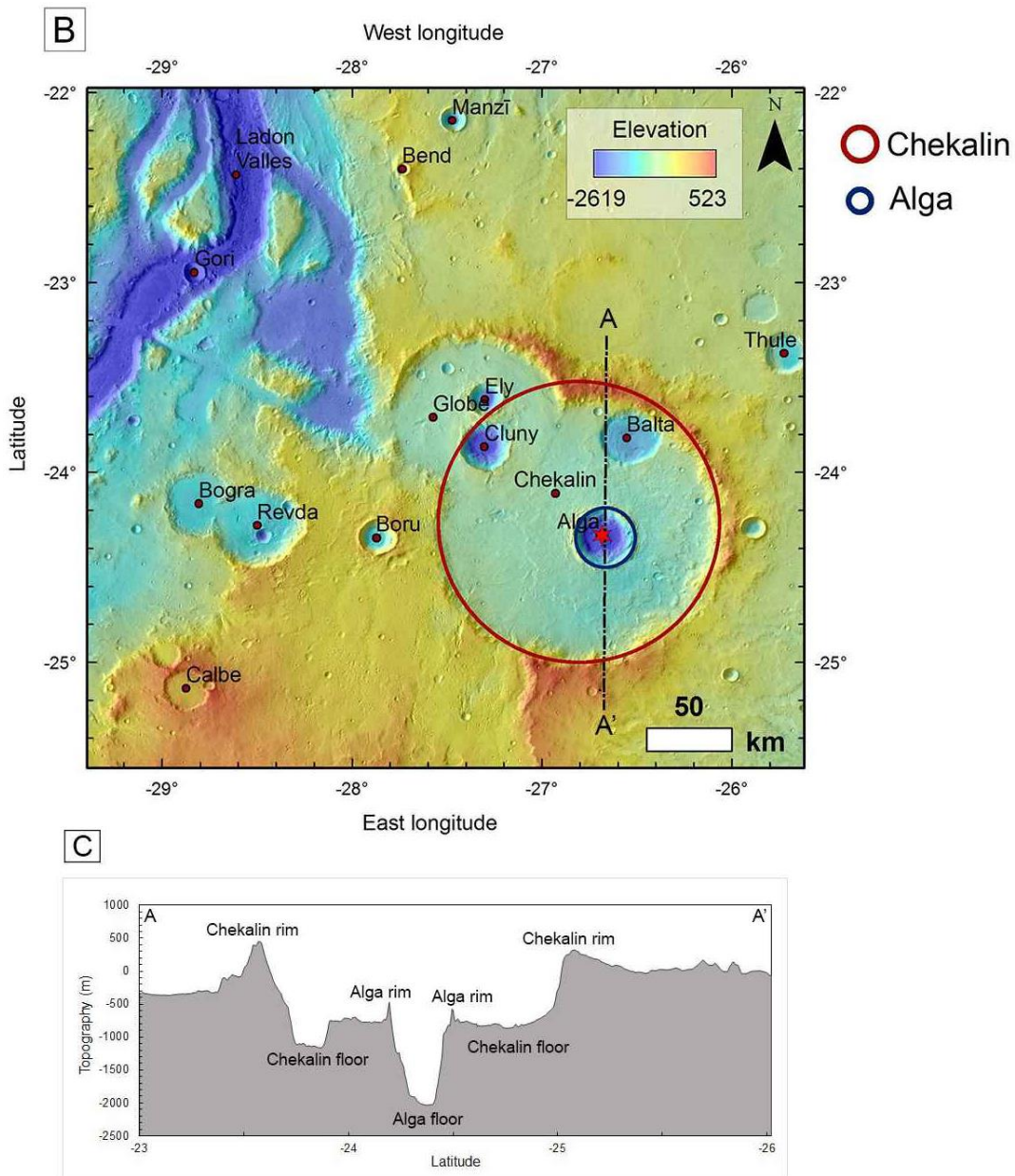


Figure 2.1. A: MGS MOLA colored hillshade map showing the geographical setting of the ~19-km diameter Alga Crater and its surrounding region. B: MGS MOLA topography over THEMIS Day IR delineating the extent of Chekalin and Alga Craters. Dotted line indicates MOLA profile from A to A'. C: MGS MOLA topography data from MEGDR over THEMIS Day IR showing cross-section starting and terminating beyond the rims of Chekalin Crater.

2.2.1 Previous studies on Alga Crater

Skok et al. (2012) conducted a spectral study of 23 well-exposed Martian crater central uplifts. For Alga Crater, they divided the central uplift into four units based on texture and composition: a light-toned olivine-bearing unit (northwestern section), a pyroxene-bearing bedrock unit (southern section), a light-toned pyroxene unit observed at the crater floor (eastern section), and a dark-toned deposit they interpreted as impact melt. CRISM spectral analysis revealed low-calcium pyroxene and fayalitic to moderately forsteritic olivine (F_{O9-43}) as the dominant mineral phases. No evidence of mineral mixing was detected in the VNIR. Skok et al. (2012) also recorded a secondary absorption feature centered at 2.2 μm , superimposed on the pyroxene absorption, and analogous to the Si-OH feature (Anderson and Wickersheim, 1964), which has been suggested to be the result of impact-induced hydrothermal activity or the mixture of silica-rich impact melt with pyroxene. Skok et al. (2012) also distinguished three units from THEMIS spectral analysis. The first spectral unit is described as a 60:40 mixture of olivine with a palagonite-like high-silica poorly crystalline phase. The second unit is consistent with TES Surface Type 1, and the third unit consists of a mixture of TES Surface Type 1 and 2 (Bandfield et al., 2000). TES Surface Type 1 is described as basaltic in nature, whereas TES Surface Type 2 is interpreted as altered basaltic materials (Wyatt and McSween, 2002), or could represent a high-silica phase as a result of the combination of a mafic and glassy high-silica impact melt component. Skok et al. (2012) concluded that most of the central uplift of Alga is dominated by the spectral unit identified as Surface Type 1 (basalt), whereas the crater floor and rim possess the combined spectral signatures of TES Surface Type 1 and 2. Although some correlations between morphological and spectral units were made, it is important to note that Skok et al. (2012) did not include any detailed morphological mapping of Alga in their study.

A thermal and near-infrared study recently published by Pan et al. (2015) looked at a total of 336 craters based on the crater database from Barlow et al. (2000) with both THEMIS and CRISM data. Alga was one of six craters in west Noachis Terra that contained more than one spectrally distinct unit in its central uplift, one being olivine-bearing and the other one pyroxene-bearing (Skok et al., 2012). A combination of olivine-poor and

pyroxene basaltic units was also recorded for Ostrov Crater (southwest of Alga) and Jones Crater (northeast of Alga). Pan et al. (2015) argued that because those three craters are not restricted to a particular diameter range, the possible existence of a continuous subsurface target lithology comprising a single olivine-bearing or pyroxene-bearing unit should be ruled out.

Finally, a recent spectral-based study by Cannon and Mustard (2015) has suggested the presence of basaltic quenched glass in well-preserved impact craters, including Alga, which they interpreted to contain impact melt glasses. Although their basaltic quenched glass spectrum is characterized by similar absorption features in the VNIR to that of low spectral contrast mafic phases (i.e., olivines, pyroxenes), Cannon and Mustard (2015) suggested that glass-bearing impactites in Alga are detected at the margins of impact melt flows. This spectral interpretation is clearly non-unique, but given the context of how the basaltic glass spectral signature often correlates with what is morphologically consistent and interpreted as impact melt flows (Tornabene et al., 2010; Skok et al., 2012), an impact melt-glass interpretation is therefore plausible. Here, we carefully re-assess the relationship between their spectral signatures for melt-glass in Alga with the detailed morphological map provided through this study.

2.3 Methodology

2.3.1 Datasets

The High Resolution Imaging Science Experiment (HiRISE) (McEwen et al., 2007) is a visible near-infrared camera aboard Mars Reconnaissance Orbiter (MRO) (Zurek and Smrekar, 2007) with a resolution of 0.25–1.3 m/pixel with swath widths of 5.0–6.4 km. HiRISE image products were reprojected using a script, "fix_jp2", created by Trent Hare from the United States Geological Survey (USGS). The script generates a .jp2.aux.xml projection auxiliary file, which overrides the internal JP2 projection of the HiRISE image by updating the .lbl label file. HiRISE-derived digital terrain models (DTMs) were also used and created by the HiRISE team using the methods described by Kirk et al. (2008).

CTX (Malin et al., 2007) is a visible camera, also onboard MRO, that images the Martian surface at ~5 m/pixel along with HiRISE. CTX images were processed with the Planetary Image Locator Tool (PILOT) of the NASA/USGS Planetary Data System (PDS).

The Compact Reconnaissance Imaging Spectrometer for Mars (CRISM) (Murchie et al., 2007) is a hyperspectral imager aboard MRO. The high-resolution or "targeted" mode uses the full capability of the spectrometer; data is collected at 15–19 m/pixel spatial sampling with 544 bands covering visible to near-infrared wavelengths (362-3920 nm) at a sampling of 6.55 nm/channel (Murchie et al., 2007). These include full resolution targeted (FRT) observations at ~18 m/pixel, half-resolution short (HRS) and long (HRL) targeted observations at ~36 m/pixel (Murchie et al., 2009). We downloaded Targeted Reduced Data Records (TRDRs) I/F products in the near-infrared (NIR; 362-1063 nm) and infrared (IR; 1002-3920 nm) wavelengths from the Planetary Data System (PDS) Geoscience Node (Guinness et al., 1996). The I/F image corresponds to a division of radiance (I) observed by the CRISM instrument by the reflectance or solar irradiance (F) incident at the top of the Martian atmosphere.

For our morphological and structural mapping, all the MRO datasets (i.e., HiRISE, CTX and CRISM) are tied to Mars Orbiter Laser Altimeter (MOLA) topography (Zuber et al., 1992). We acquired the MGS MOLA Global Colourized Hillshade (128 ppd) in the Equirectangular (Simple Cylindrical) projection from the PDS Geosciences Node (Guinness et al., 1996).

Thermal Emission Imaging System (THEMIS) (Christensen et al., 2004) data provide significant insights into the thermophysical properties of the surface. In particular, thermal inertia represents the resistance to changes in temperature (Ferguson et al., 2006), and can be used to identify exposed bedrock, which has high thermal inertia values, whereas unconsolidated fine-grained particles have lower values (Mellon et al., 2000).

THEMIS is a multi-spectral thermal infrared imager aboard the 2001 Mars Odyssey (MO) spacecraft. We acquired the THEMIS daytime infrared (IR) and nighttime IR images for the Margaritifer Sinus controlled mosaic as well as the associated qualitative (8-bit) THEMIS-derived Thermal Inertia (TI) (Fergason et al., 2006).

Table 2.1. Orbital datasets used in this study.

Instruments	Data product ID	Resolution
HiRISE	PSP_007929_1555_RED_A_01_ORTHO	25 cm/pixel
	PSP_007573_1555_IRB_A_01_ORTHO	25 cm/pixel
	DTEEC_007573_1555_007929_1555_A01	1.00 m/pixel
CTX	B09_013213_1707_XN_09S295W	5.24 m/pixel
	B10_013635_1707_XN_09S295W	5.71 m/pixel
	B17_016114_1712_XN_08S295W	5.24 m/pixel
	D13_032465_1727_XI_07S296W	5.27 m/pixel
CRISM	FRT00006415_07_IF164	18 m/pixel
MOLA	Global Colourized Hillshade 90Nto90S	463 m/pixel
THEMIS	Controlled Mosaic Day and Night IR Margaritifer Sinus 30S-315E	100 m/pixel
	THEMIS-derived thermal inertia I07872013	100 m/pixel

2.3.2 Morphological and structural mapping

Detailed decametre- to sub-metre scale morphological and structural mapping was performed in ArcGIS using HiRISE (McEwen et al., 2007) and CTX (Malin et al., 2007) visible imagery. The "DigSym" ArcGIS add-on tool provided by David Viljoen from the Geological Survey of Canada (GSC) at Natural Resources Canada (NRCan) was used for mapping the orientation (trend) of structural features. Digital mapping was performed at a general scale of 1:2000 up to 1:700. Textural differences, relative tonality and stratigraphic relationships were the main criteria considered for the characterization of morphological units which were manually traced out from a Wacom tablet in ArcMap. Slopes and elevation contours were generated from the HiRISE-derived DTM with the contour lines set to 100 metre intervals. 3D perspectives were created in ArcScene by draping the HiRISE orthoimage over the DTM.

2.3.3 Spectral analysis

Spectral analysis is based on the interpretation of spectral reflectance data. It was conducted using the CRISM Analysis Tool (CAT) v.7.2.1 developed for Exelis ENVI based on procedures outlined by Murchie et al. (2007, 2009). First, the calibrated Targeted Reduced Data Record (TRDR) Version 3 (v3) products were converted to an ENVI-readable format. TRDR data processing included a basic photometric correction for Lambertian scattering that corrected variations in illumination, an atmospheric correction that accounted for CO₂ opacity effects, and data filtering, including striping and spiking corrections. These corrections are always essential to perform prior to the interpretation of mineralogical features from CRISM data. The photometric correction divided the CRISM reflectance (I/F) image by the cosine of the incidence angle. A volcano-scan atmospheric correction also divided the IR (L) image by a scaled ratio transmission spectrum derived from observations over Olympus Mons (Bibring et al., 2005; Mustard et al., 2008; Murchie et al., 2009b; McGuire et al., 2009). This was followed by a denoising algorithm that removed vertical stripes and spectral spikes in data (Parente, 2008). Once the photometric and atmospheric corrections were applied as well as data filtering performed, spectral parameter and summary products were generated for the VNIR (S) and IR (L) images (Pelkey et al., 2007; Murchie et al., 2009b), and hyperspectral summary products were derived for the L image. In addition to the standard summary products, a synthetic basaltic glass spectral endmember parameter created by Cannon and Mustard (2015) was used to map the geospatial distribution of putative basaltic quenched glass at spectral fractions of ~15% or higher, and to compare with our mapped morphological units.

A CRISM spectral parameter and summary colour composite (red: OLINDEX, green: LCPINDEX, blue: HCPINDEX) was derived from the spectral summary products for both the S and L images. A linear stretch was applied to each channel (OLINDEX, stretched 0.000-0.150; LCPINDEX, stretched 0.00-0.500; HCPINDEX, stretched 0.000-0.400). Regions of interest (ROIs) were constructed by defining spectral parameter thresholds. We ratioed ROIs to nearby spectrally bland or "dusty" regions of similar pixel size located in the same column to cancel out systematic artifacts along the same

detectors and enhance spectral signatures (Murchie et al., 2009). Spectra were collected for several ROIs created from band thresholds and with the highest OLINDEX and LCPINDEX, which is indicative of either a greater concentration of the mineral or a larger particle size (Pelkey et al., 2007). Band threshold ROIs were intersected with ROIs drawn based on morphological features (e.g., outcrops of bedrock). Finally, these CRISM-extracted ratioed spectra were compared with laboratory spectra of the CRISM and USGS spectral libraries (Clark et al., 2007; <http://speclab.cr.usgs.gov/spectral.lib06>) to determine the best-match for mineral identification and verify spectral units highlighted by the various spectral parameter and summary products used in this study.

In order to tie the morphological and structural mapping to the inferred mineralogical composition, we used the methods provided by Delamere et al. (2010) to register the CRISM Full-Resolution Targeted (FRT) observation FRT00012CD9_07_IF164 onto the HiRISE Red orthoimage PSP_007929_1555. Band parameters OLINDEX, LCPINDEX, and HCPINDEX were chosen for the CRISM RGB composite in order to highlight the unaltered mafic-rich materials characterizing the various units of the central uplift of Alga Crater as previously observed by Skok et al. (2012). The first step was to establish a network of Ground Control Points (GCPs) between the CRISM colour composite and the HiRISE RED orthoimage. The CRISM colour composite was warped and then overlain onto the HiRISE orthoimage using a Hue Saturation and Value (HSV) transform, which retains the colour information of the CRISM RGB composite and effectively combines it with the high-resolution tonal and morphological information from the HiRISE orthoimage. In addition, a three-dimensional (3D) surface view of the HSV transformed composite was generated using elevation data from the HiRISE-derived DTM.

2.3.4 THEMIS-derived thermal inertia

We computed thermal inertia in ENVI for each morphological units by selecting regions of interest that best represented each morphological units, and recorded the average thermal inertia and standard deviation values.

2.4 Results

The central uplift of Alga consists of one dominant topographic peak (Fig. 2.2) that occupies an area of $\sim 16 \text{ km}^2$, with a north-south maximum length of $\sim 5 \text{ km}$ and east-west length of $\sim 4.8 \text{ km}$. DTM-derived average slope measurements range from between $\sim 12\text{--}22^\circ$, and elevation ranges from $-1,900 \text{ m}$ at the crater floor to $-1,500 \text{ m}$ at the top of the uplift. Below we describe the mapped units based on the results of our morphological, structural, and spectral mapping. A summary of various physical attributes for each morphological unit is provided in Table 2.2. Figure 2.3 is a simplified morphological map of the central uplift of Alga Crater. Morphological units are defined based on texture, tonality, and stratigraphic relationships.

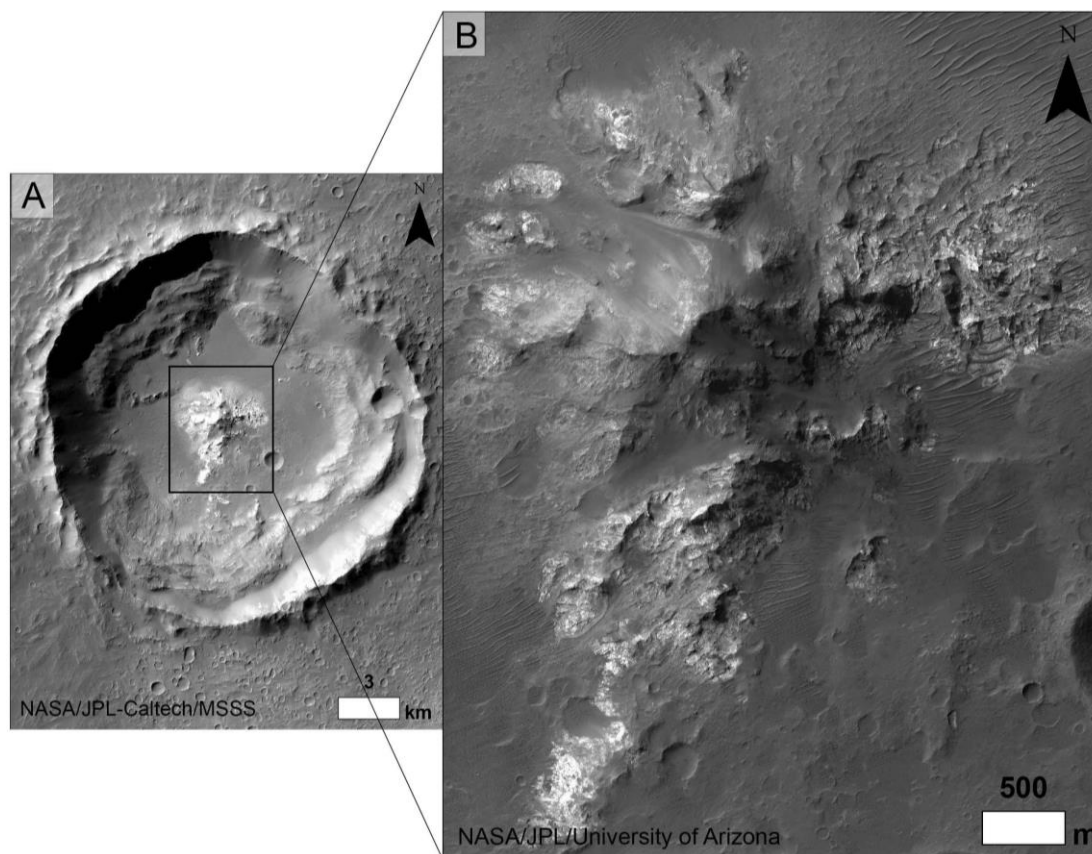


Figure 2.2. A: CTX image P18_007929_1555_XI_24S026W of Alga Crater. B: HiRISE orthoimage PSP_007929_1555 of the central uplift of Alga Crater.

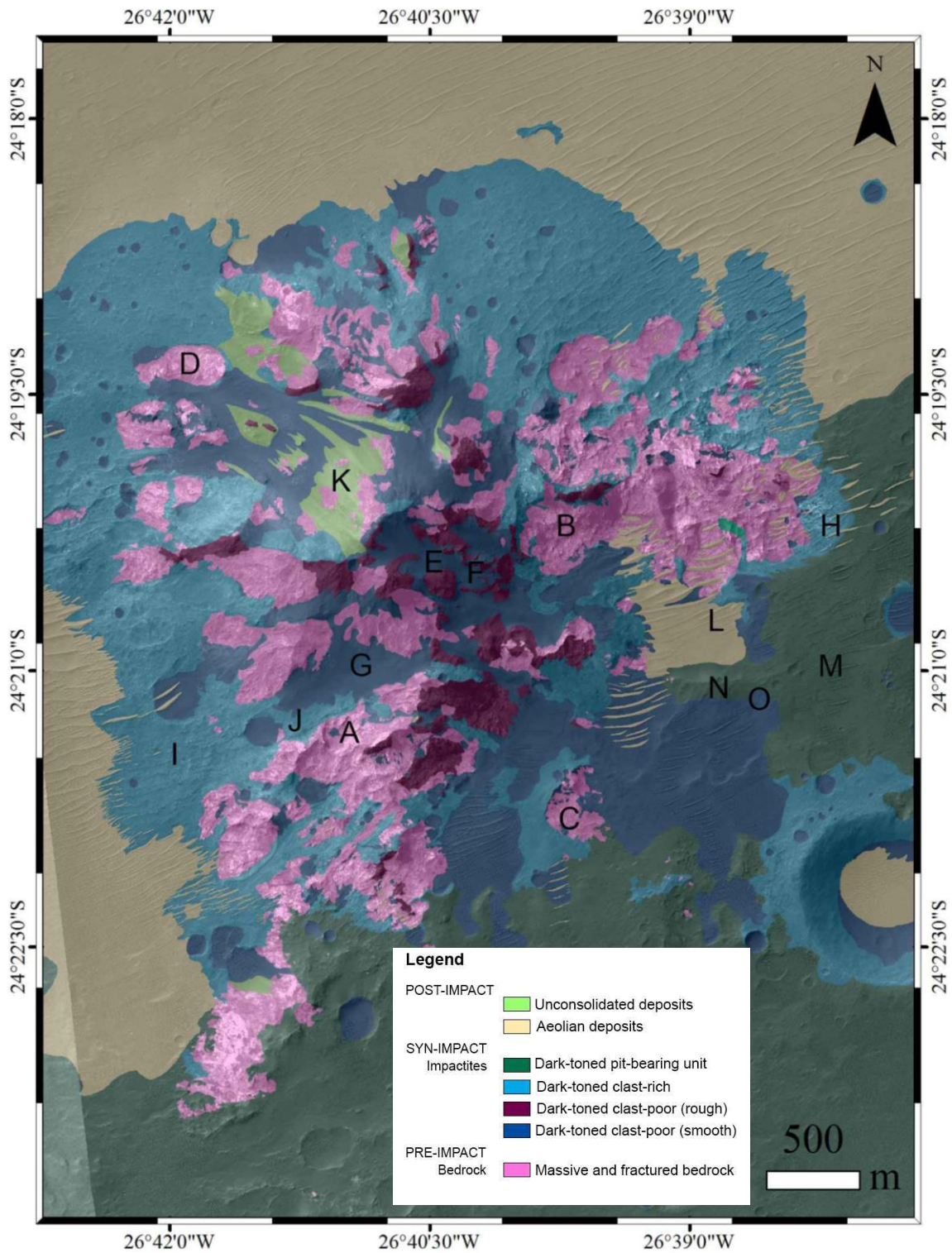


Figure 2.3. Morphological map of the central uplift of Alga Crater over HiRISE orthoimage PSP_007929_1555.

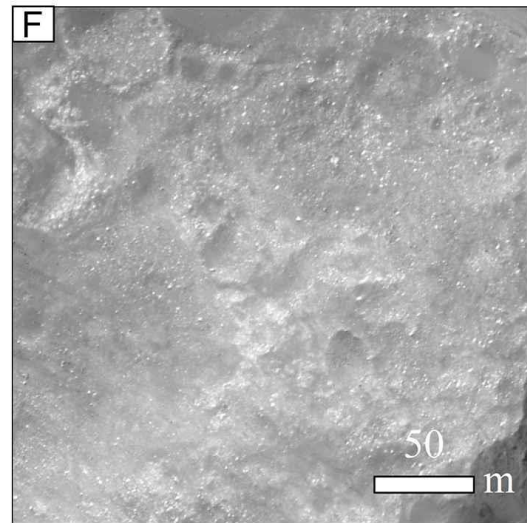
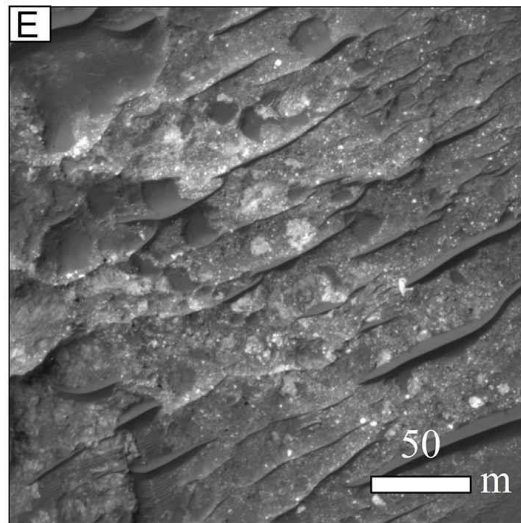
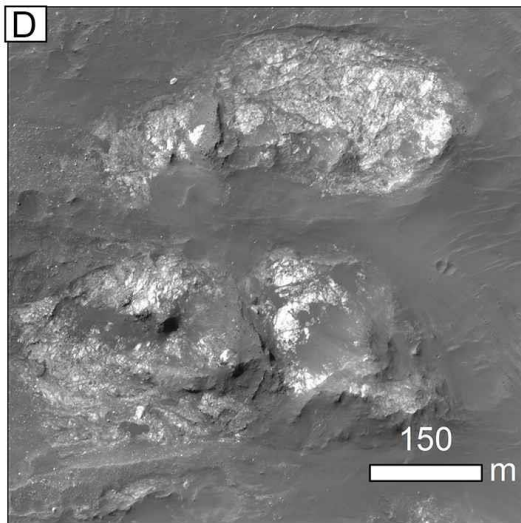
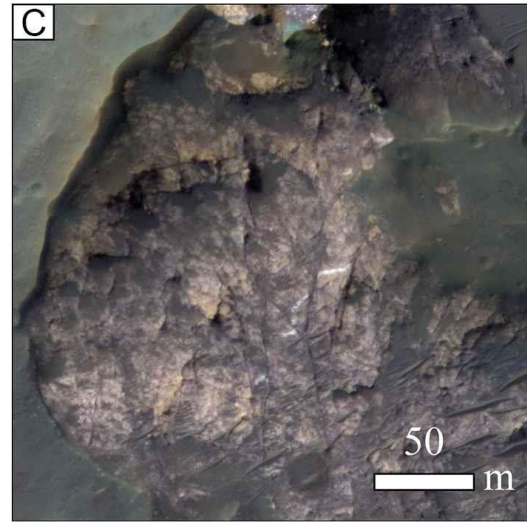
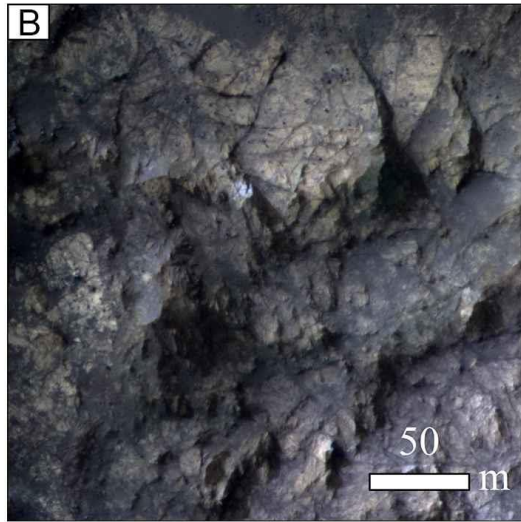
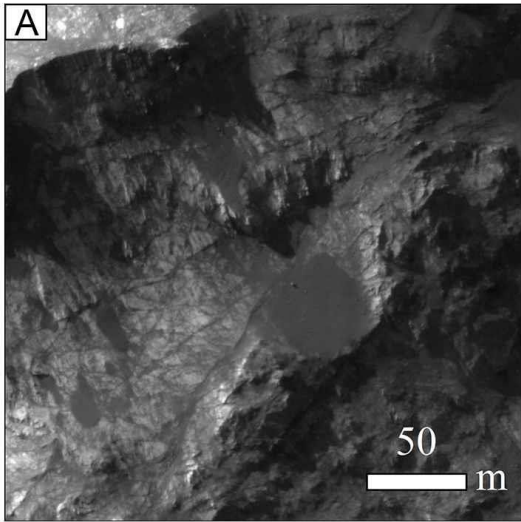
2.4.1 Massive and fractured bedrock (MFB) unit

The massive and fractured bedrock (MFB) unit occurs as relatively light-toned massive textured bedrock that is cross-cut by pervasive dark-toned linear and quasi-linear features that are fractures, faults, and/or dikes (Figs. 2.4A, B, C, D). Fractures are surfaces along which rocks have broken; faults are fractures that have been offset, whereas joints have undergone little or no displacement. On the other hand, dikes represent the material that fills an open fracture. However, it is difficult to observe offsets in the massive and fractured bedrock from orbital data only. In general, MFB is the lightest-toned materials that can be observed in CTX and HiRISE images of the uplift (Fig. 2.2B). Overall, MFB accounts for $\sim 3.5 \text{ km}^2$ ($\sim 22\%$) of the total area ($\sim 16 \text{ km}^2$) of the uplift, and occurs over a range of slopes (avg. $\sim 18^\circ$, std. dev. ~ 9) (Table 2.2).

Table 2.2. Properties of each morphological units.

Unit Name	HiRISE-derived DTM Slope				Area (km ²)	Percentage of uplift (%)
	Max.	Min.	Avg.	Std. Dev.		
Massive and fractured bedrock	79.8	0.0	17.6	8.8	3.5	21.9
Dark-toned clast-rich unit	76.9	0.0	12.3	7.4	6.5	40.2
Dark-toned clast-poor unit (smooth)	50.2	0.4	12.9	6.5	3.9	23.8
Dark-toned clast-poor unit (rough)	72.5	0.0	22.0	8.9	0.6	3.9
Dark-toned pit-bearing unit	79.2	0.0	12.3	8.7	0.9	5.3
Unconsolidated materials	60.5	0.1	17.2	6.4	0.4	2.2
Aeolian deposits	78.5	0.0	11.2	8.7	0.4	2.7

Discrete exposures of the MFB unit occur in the northwestern and western sections of the uplift (Fig 2.4D) and correspond to particularly well-exposed outcrops that possess a sharp and distinct boundary with the adjacent morphological units. These exposures correlate with the highest values of thermal inertia (TI) associated with Alga Crater (avg. $\sim 547 \text{ J m}^{-2} \text{ K}^{-1} \text{ s}^{-1/2}$, std. dev. ~ 16) (Table 2.3, Fig. 2.5). The southwestern and eastern sections of the uplift are occupied by lighter-toned outcrops of this unit that does not appear as resistant as outcrops in the northwestern and western sections, and that exhibit intermediate values of TI (avg. ~ 420 (SW), ~ 443 (E) $\text{J m}^{-2} \text{ K}^{-1} \text{ s}^{-1/2}$, std. dev. ~ 8).



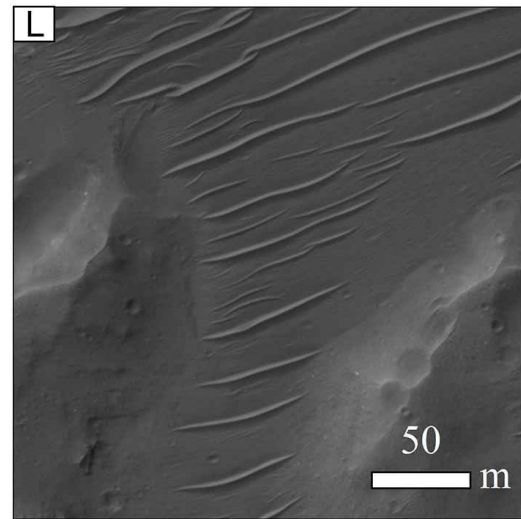
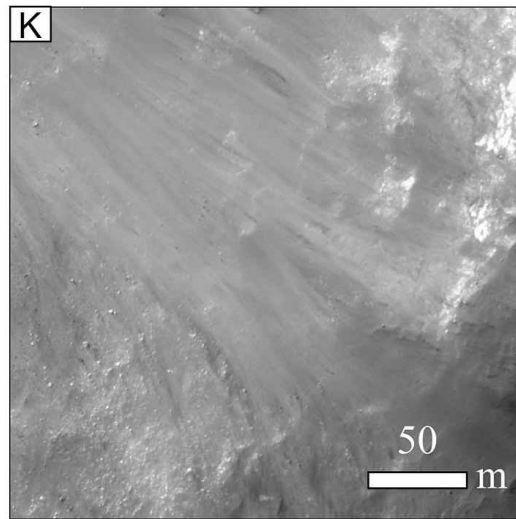
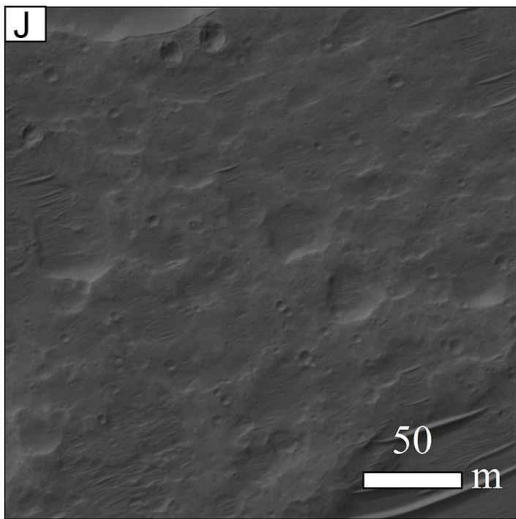
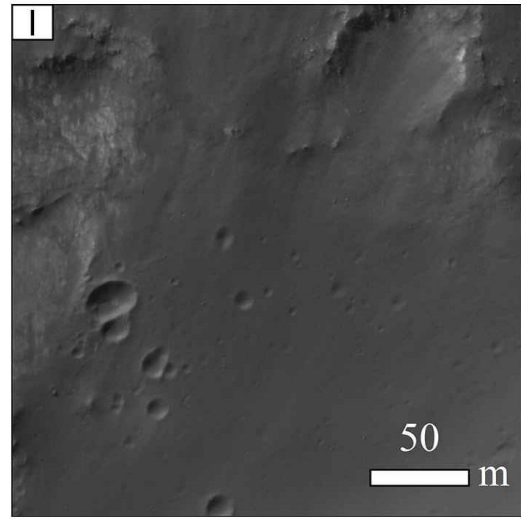
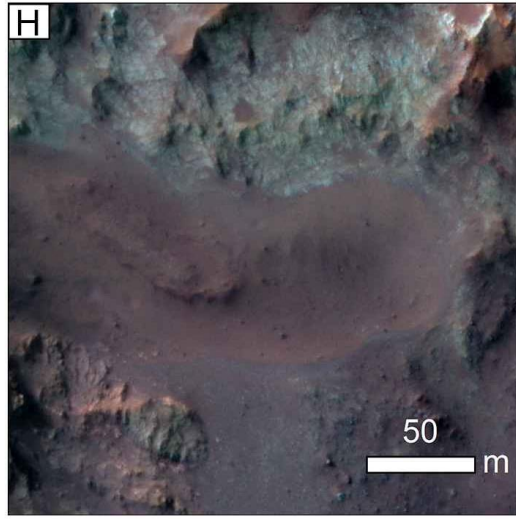
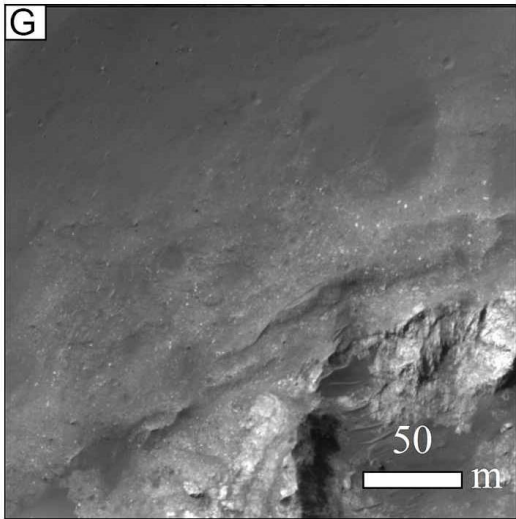


Figure 2.4. Morphological units of HiRISE RED orthoimage PSP_007929_1555 and IRB orthoimage PSP_007573_1555. Refer to Fig. 2.3 to view location of each morphological units indicated by the letter ID. A: MFB in southwestern section showing dark-toned lineaments ranging from ~80–140 m in length of southwest-northeast orientation. B: MFB in the eastern section of the central uplift showing dark-toned lineaments. C: MFB in the southern section of the uplift which appears as a geological window. D: Well-exposed outcrops of MFB in the northwestern section of the uplift. E: Dark-toned clast-rich unit at the eastern crater floor showing coarser light-toned clasts enrichment. F: Dark-toned clast-rich unit at the western crater floor showing finer-grained light-toned clasts enrichment. G: Dark-toned clast-rich unit located at the northern margin of an outcrop of MFB. H: Dark-toned clast-poor unit in the eastern section of the uplift and showing crater-retaining morphology. I: Dark-toned clast-poor unit in the western section of the uplift. J: Dark-toned pit-bearing unit at the southern crater floor showing relatively shallow circular pits. K: Unconsolidated materials located on the northwestern slope of the uplift. L: Aeolian bedforms at the southern crater floor. Images credit: NASA/JPL/University of Arizona.

Table 2.3. Themis-derived thermal inertia for each morphological units.

Unit Name	Thermal inertia	
	Avg.	Std. Dev.
Massive and fractured bedrock (NW)	547	16
Massive and fractured bedrock (SW)	420	8
Massive and fractured bedrock (E)	443	8
Dark-toned clast-rich unit	376	5
Dark-toned clast-poor unit	292	11
Dark-toned pit-bearing unit	338	7
Unconsolidated materials	425	5
Aeolian deposits	313	6

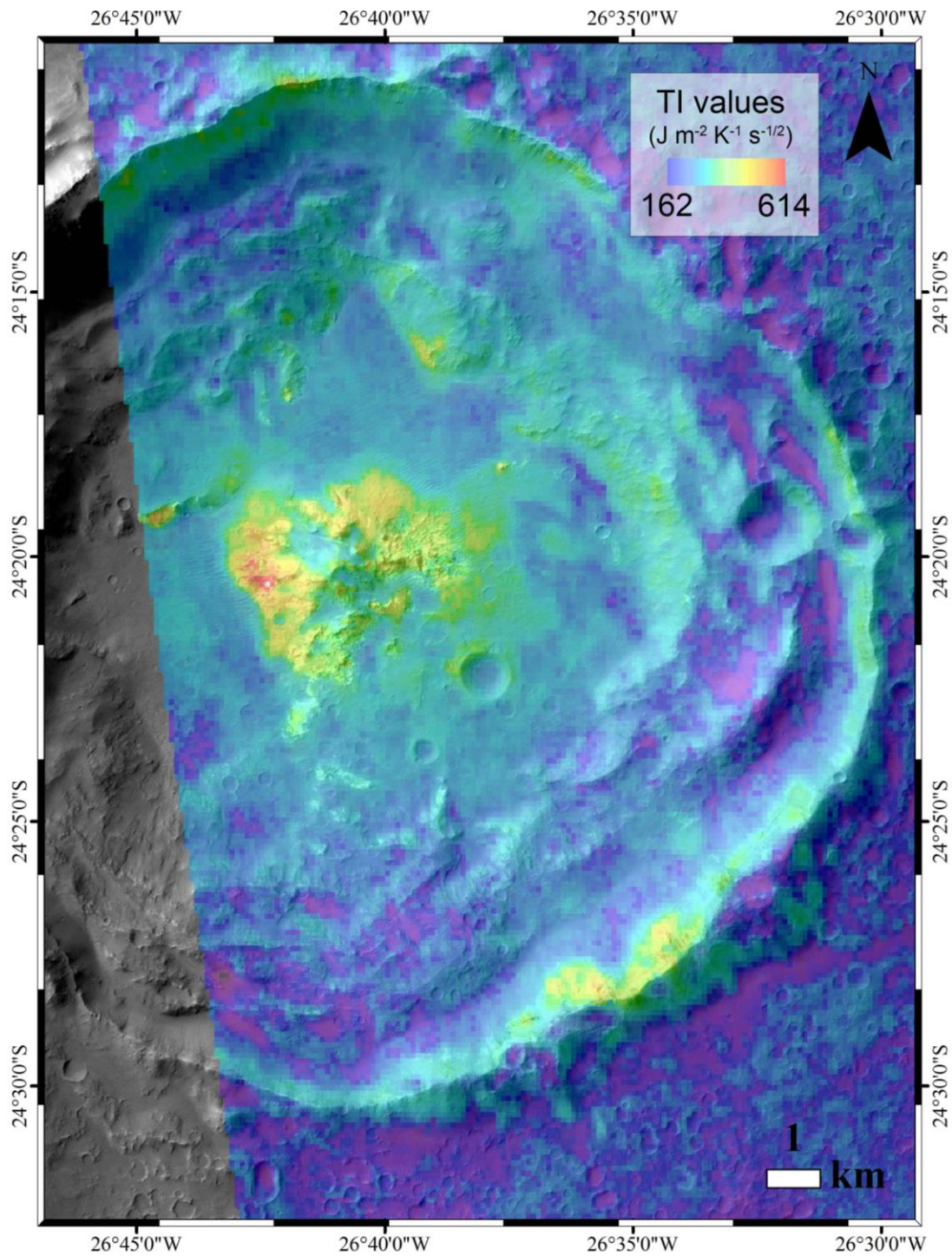


Figure 2.5. Themis-derived thermal inertia map overlying CTX image P18_007929_1555_XI_24S026W of Alga Crater (stretch 162 to 614 J m⁻² K⁻¹ s^{-1/2}).

A CRISM summary colour composite (Fig. 2.6) of mafic spectral parameters OLINDEX, LCPINDEX and HCPINDEX reveals that the strongest olivine and low-calcium pyroxene (LCP) signatures in the central uplift of Alga Crater are associated to the MFB. A strong olivine signature is specifically observed for outcrops of MFB in the western and northwestern sections of the uplift. The remaining bulk of the uplift show spectral absorptions in LCP, with the strongest signatures observed in the northwestern and western sections of the uplift similarly to olivine.

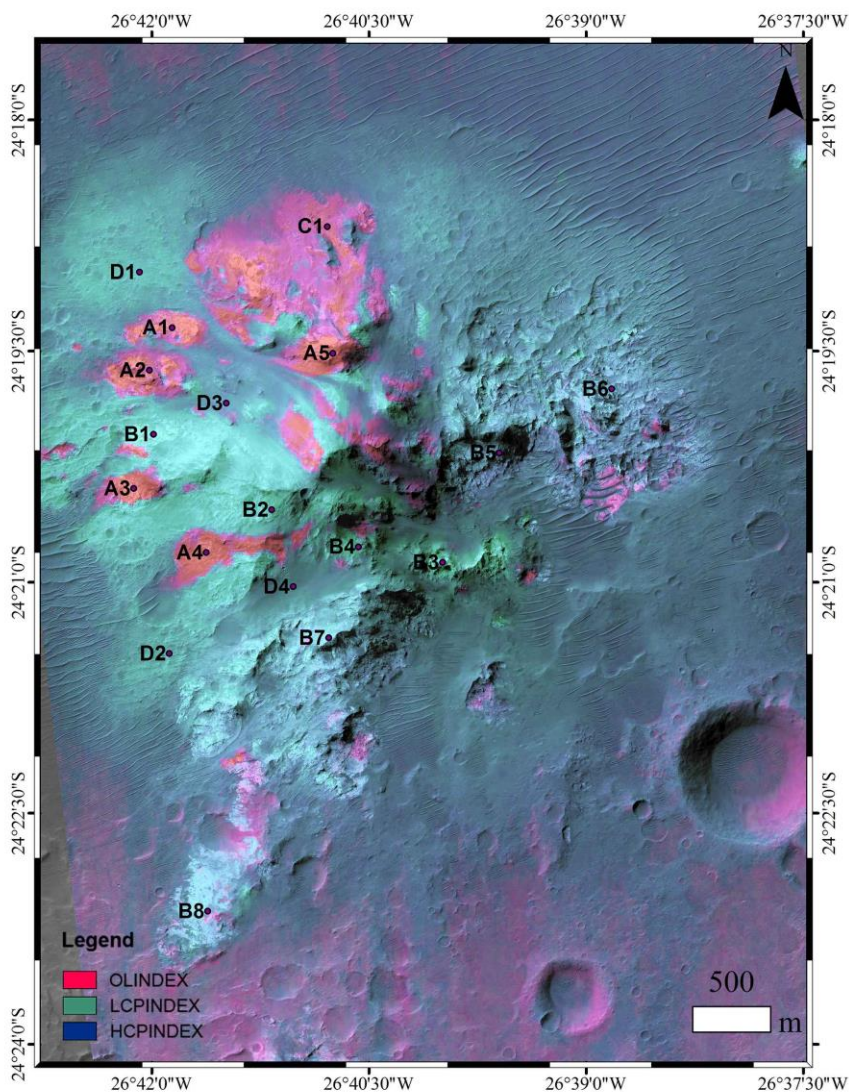


Figure 2.6. Mafic spectral parameter and summary product superposed on HiRISE orthoimage PSP_007929_1555.

Spectral analysis of the MFB outcrops in the northwestern and western sections reveals broad spectral absorptions centered at $\sim 1 \mu\text{m}$ (Fig. 2.7A) as well as comparable band position and strength to the mineral olivine (Adams, 1974, 1975; King and Ridley, 1987). Ratioed spectra collected on the MFB for the remaining bulk of the central uplift reveal broad absorption bands centered at values just below $2 \mu\text{m}$ (Fig. 2.7B), characteristic of low-calcium pyroxene (Adams, 1974; Cloutis and Gaffey, 1991) and previously determined from MGM analysis conducted by Skok et al. (2012). The LCP-bearing MFB in the northwestern and western sections of the uplift (Figs. 2.7B1, B2, B3, B4) has deeper pyroxene band depths and stronger spectral absorptions than other exposures in the eastern (Figs. 2.7B5, B6) and southwestern (Figs. 2.7B7, B8) sections of the uplift. Although a difference in band depths is recorded for LCP in the northwestern/western, southwestern and eastern sections of the uplift, band positions are comparable. Extracted spectra of olivine are compared to olivineKI3005 because of its similar forsterite content (Fo_{11}) to the mean (Fo_{18}) determined from MGM analysis by Skok et al. (2012). Extracted spectra of low-calcium pyroxene are compared to enstatite (NMNH128288) from the USGS digital spectral library splib01 (Figs. 2.7E, F). Table 2.4 provides X and Y coordinates and size of selected regions of interest and bland areas.

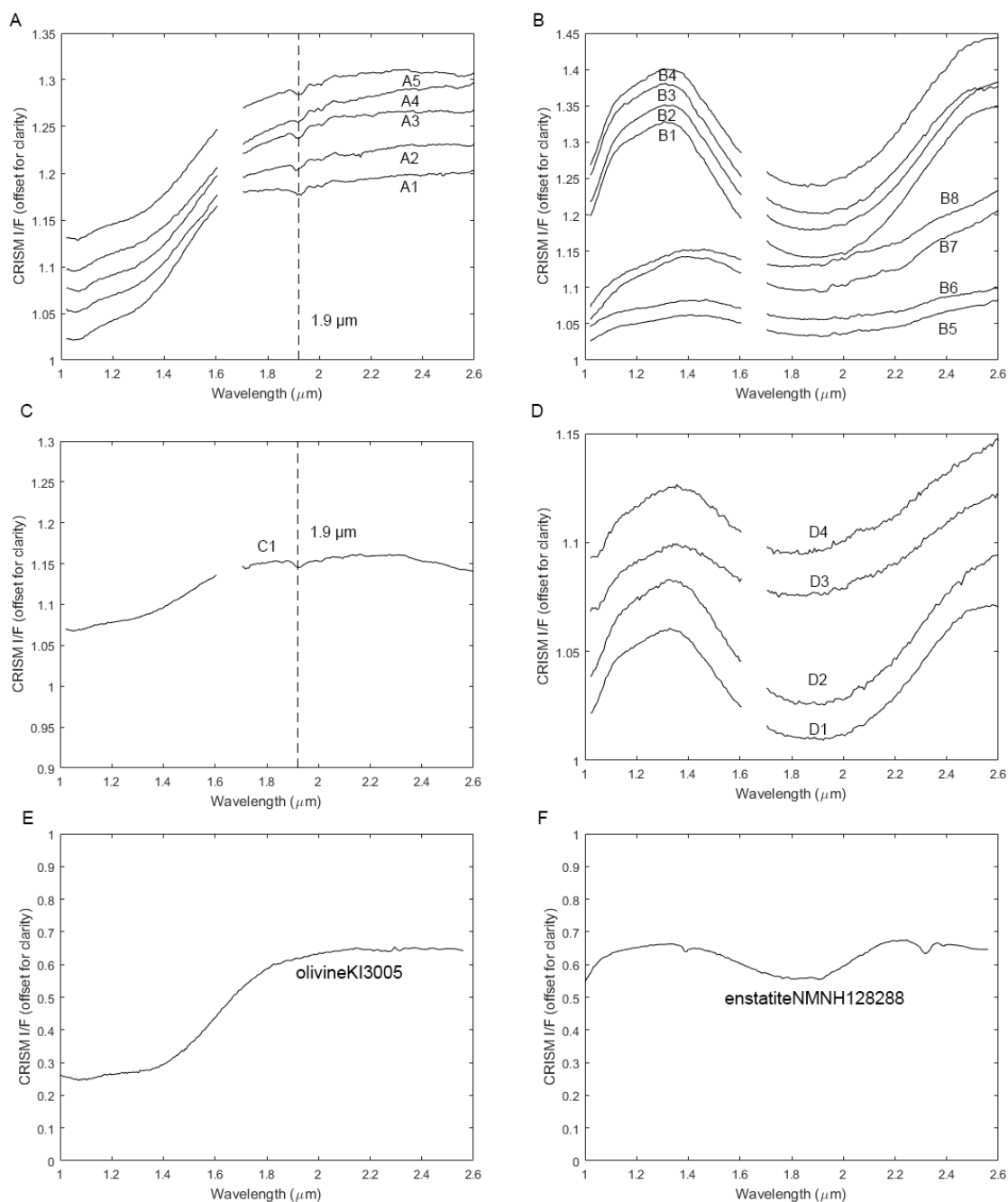


Figure 2.7. Ratioed CRISM I/F spectra extracted from FRT00006415_07_IF164. A: OLINDEX spectra from ROIs representing outcrops of MFB in the northwestern and western sections of the uplift. B: LCPINDEX spectra from ROIs representing outcrops of MFB in the northern, western, southwestern and eastern sections of the uplift. C: OLINDEX spectrum from a ROI taken on the dark-toned clast-rich. D:

LCPINDEX spectra from ROIs taken on the dark-toned clast-rich unit at the crater floor in the northwestern and western sections of the uplift and on the dark-toned clast-poor unit in the northwestern and southwestern sections of the uplift. E: Laboratory spectrum olivineKI3005 from the USGS digital spectral library splib01. F: Laboratory spectrum enstatiteNMNH128288 from the USGS digital spectral library splib01.

Table 2.4. CRISM spectra regions of interest (ROIs) and denominators.

CRISM summary products	Morphological units	ROI X	ROI Y	ROI size (pixels)	Bland area X	Bland area Y	Bland area size (pixels)	Band thresholds
OLINDEX	MFB (western quadrant)	478	271	91	481	336	260	0.075-0.15
OLINDEX	MFB (western quadrant)	492	256	84	492	334	325	0.075-0.15
OLINDEX	MFB (western quadrant)	503	211	98	500	334	154	0.075-0.15
OLINDEX	MFB (western quadrant)	478	181	64	478	337	156	0.075-0.15
OLINDEX	MFB (western quadrant)	422	255	107	421	347	240	0.075-0.15
OLINDEX	MFB (western quadrant)	595	294	60	594	348	110	0.075-0.15
OLINDEX	Dark-toned clast-rich	409	291	50	412	338	406	0.04-0.15
LCPINDEX	MFB (western quadrant)	497	231	56	493	336	190	0.35-0.5
LCPINDEX	MFB (western quadrant)	459	200	64	360	336	300	0.35-0.5
LCPINDEX	MFB (western quadrant)	380	166	18	384	339	56	0.3-0.5
LCPINDEX	MFB (western quadrant)	421	181	15	420	347	56	0.3-0.5
LCPINDEX	MFB (eastern quadrant)	302	236	278	301	326	56	0.03-0.5
LCPINDEX	MFB (eastern quadrant)	365	206	206	363	364	288	0.03-0.5
LCPINDEX	MFB (southwestern quadrant)	477	74	115	476	342	156	0.03-0.5
LCPINDEX	MFB (southwestern quadrant)	433	145	152	430	349	272	0.03-0.5
LCPINDEX	Dark-toned-clast-poor	460	241	43	460	337	75	0.03-0.5
LCPINDEX	Dark-toned-clast-poor	449	165	37	449	337	84	0.03-0.5
LCPINDEX	Dark-toned clast-rich	493	295	310	493	336	190	0.03-0.5
LCPINDEX	Dark-toned clast-rich	497	147	101	496	335	132	0.03-0.5

2.4.2 Dark-toned clast-rich unit

This unit is composed of poorly sorted angular to semi-angular light-toned clasts generally ranging from ~1–15 m in size embedded in a dark-toned matrix (Fig. 2.4E). The matrix is indistinguishable from the matrix of the dark-toned clast-poor unit (see section 2.4.3). The clast-poor unit generally grades directly into this clast-rich unit towards the crater floor (Fig. 2.4F), and often terminates at the periphery of outcrops of the MFB unit (Figs. 2.4G). Exposures of the MFB unit are partially coated, superposed and embayed by both the dark-toned clast-rich and -poor units. The clast-rich unit accounts for the greatest extent (~6.5 km² or ~40%) of the uplift. The clast-rich unit generally occurs on intermediate to low slopes (avg. ~12 °, std. dev. ~7), and possess one of the highest thermal inertia values (avg. ~376 J m⁻² K⁻¹ s^{-1/2}, std. dev. ~5) (Table 2.3), aside from the MFB and unconsolidated materials.

Extracted spectra of this unit at the western and northwestern crater floor possess strong signatures in LCP (Figs. 2.7D1, D2). The CRISM mafic spectral parameter and summary colour composite (Fig. 2.6) reveals that the dark-toned clast-rich unit correlates with LCP across the uplift, especially at the crater floor. On the other hand, there are a few occurrences in the northern section of the uplift characterized by olivine-bearing materials.

2.4.3 Dark-toned clast-poor unit

This is a characteristic dark-toned, coherent (preferentially crater-retaining), and smooth-textured unit that contains rare occasional clasts (Figs. 2.4H, I). The "clast-poor" description is included here because of the contiguous grading relationship between this unit and the clast-rich unit described above. This unit likewise appears to be partially coating MFB in some localities, but is commonly observed as a nearly flat-lying unit that embays topographically higher-standing units including outcrops of MFB (Figs. 2.4H, I). In some localities, particularly in the eastern section of the uplift, this unit exhibits a smooth texture when coating relatively even topography, whereas it displays a comparatively rougher texture when coating uneven outcrops of MFB. It also appears to be contiguous to the dark-toned clast-rich unit at the crater floor. Spectral analysis

reveals weaker absorptions in LCP, hence weaker band depths (compared to the LCP signature of the MFB and clast-rich units) in the western and northwestern sections of the uplift (Figs. 2.7D3, D4). Overall, this unit covers $\sim 4.5 \text{ km}^2$ ($\sim 28\%$), and occurs over a range of both steep slopes in the uplift and low slopes at the crater floor (smooth texture: avg. $\sim 13^\circ$, std. dev. ~ 7 ; rough texture: avg. $\sim 22^\circ$, std. dev. ~ 9). Thermal inertia values (avg. $\sim 292 \text{ J m}^{-2} \text{ K}^{-1} \text{ s}^{-1/2}$) (Table 2.3) are lower than for the dark-toned clast-rich and dark-toned pit-bearing units (see section 2.4.4).

2.4.4 Dark-toned pit-bearing unit

This unit is best observed at the southern crater floor and is characterized by arcuate ridges and quasi-circular relatively shallow subdued pits (Fig. 2.4J) that range from ~ 5 – 340 m in diameter. In the southeastern, we observe a clear stratigraphic relationship between this and three other mapped morphological units (Fig. 2.8). A topographically high-standing feature is coated by the dark-toned pit-bearing unit and embayed within the dark-toned clast-poor unit, which is in turn overlain by aeolian deposits (Fig. 2.8A). Metre- to decametre- scale light-toned boulders are observed on the north-facing slope of this feature, and a flow feature with distinct flow lines is observed on the south-facing slope (Fig. 2.8B). Most of the pit-bearing unit is generally overlain by aeolian bedforms, especially in the northern section of the uplift (where it is mapped as aeolian deposits only in Fig. 2.3), but it can still be clearly recognized. Overall, this unit appears to completely surround and embay the central uplift, and is generally observed to be predominantly contiguous with the dark-toned clast-poor and clast-rich units. It covers $\sim 0.9 \text{ km}^2$ ($\sim 5\%$) of the uplift (but all of the crater floor), and occurs on relatively low topography (avg. $\sim 12^\circ$, std. dev. ~ 9), and has higher thermal inertia than the dark-toned clast-poor unit (avg. $\sim 338 \text{ J m}^{-2} \text{ K}^{-1} \text{ s}^{-1/2}$, std. dev. ~ 7) (Table 2.3). No distinct spectral signature in the VNIR appears to be associated with this unit.

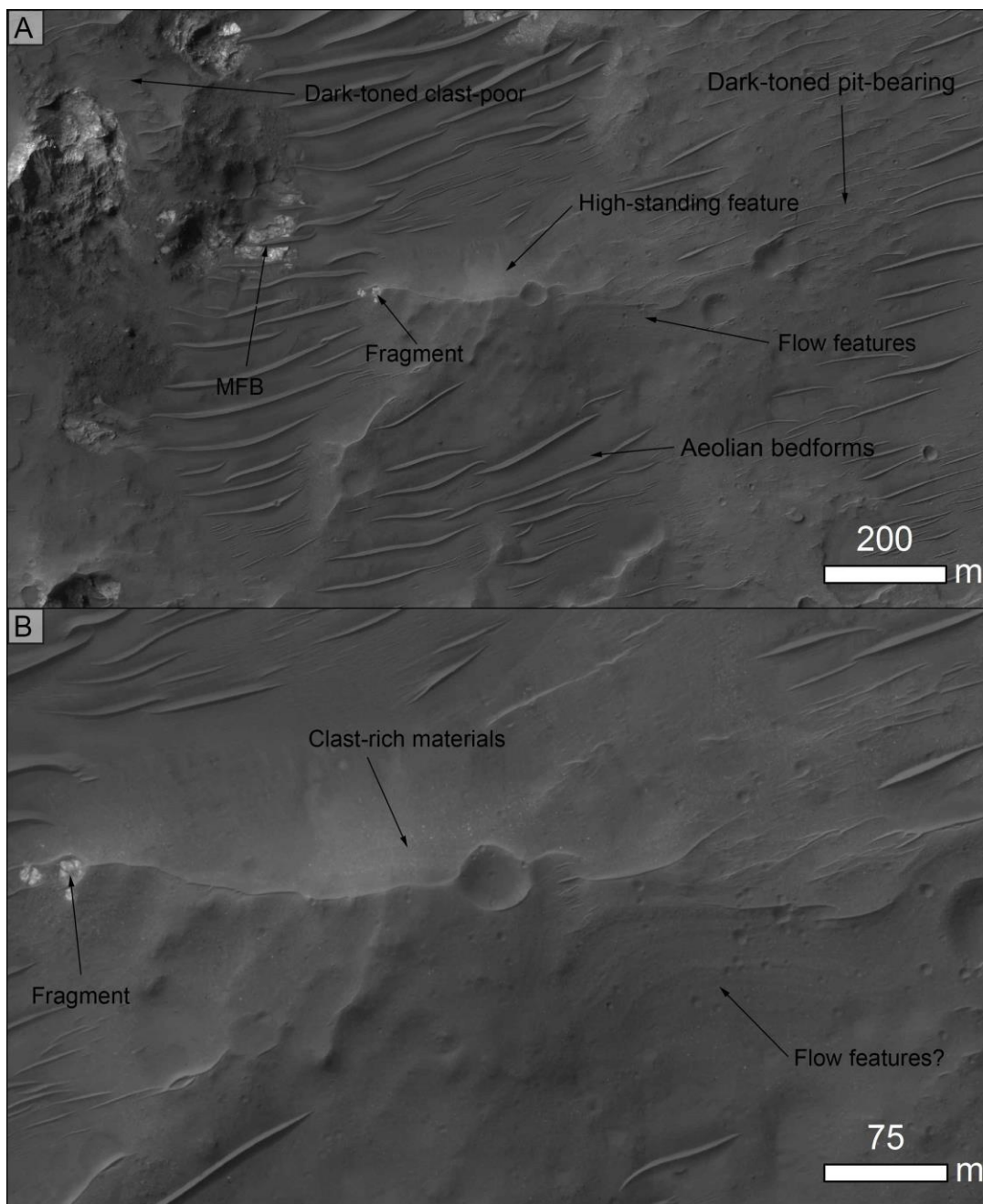


Figure 2.8. HiRISE orthoimage PSP_007929_1555. The relationship between 4 morphological units is illustrated here: a high-standing topographic feature overlain by the dark-toned pit-bearing unit is embayed within the dark-toned clast-poor unit. The topographic feature is characterized by clast-rich materials on its north-facing slope and putative flow features on its south-facing slope.

2.4.5 Unconsolidated materials

This unit is found amongst the steepest slopes of the uplift, and overlies the dark-toned clast-poor unit in the northwestern section (Fig. 2.4K). This unit covers $\sim 0.4 \text{ km}^2$ ($\sim 2\%$) of the area occupied by the central uplift, generally occurs on steep slopes of the uplift (avg. $\sim 17^\circ$, std. dev. ~ 6), and has the second highest thermal inertia (avg. $\sim 425 \text{ J m}^{-2} \text{ K}^{-1} \text{ s}^{-1/2}$, std. dev. ~ 5) (Table 2.3) after the MFB.

2.4.6 Aeolian deposits

This unit occurs within low-lying depressions and is superposed on the dark-toned pit-bearing unit at the southern crater floor, whereas it is widespread at the northern crater floor. The unit includes characteristic aeolian bedforms that have a preferential southwest-northeast orientation (Fig. 2.4L). This unit covers $\sim 0.4 \text{ km}^2$ ($\sim 2.7\%$) of the uplift, occurs on low slopes (avg. $\sim 11^\circ$, std. dev. ~ 9), and is characterized by the second lowest thermal inertia (avg. $\sim 313 \text{ J m}^{-2} \text{ K}^{-1} \text{ s}^{-1/2}$, std. dev. ~ 6) (Table 2.3) after the dark-toned clast-poor unit.

2.4.7 Lineaments

The results of the structural mapping reveal a range of darker-toned lineaments cross-cutting the exposed MFB, including short and narrow lineaments to longer and thicker ones (Fig. 2.9A). A certain proportion of lineaments could not be mapped as they are located in shaded regions. We have identified approximately ten of these larger lineaments in the southwestern section of the central uplift with a preferential southwest-northeast trend, and that range from ~ 80 – 140 m in length (Fig. 2.9B). Lineaments were mapped for the western, eastern, southwestern and southeastern sections of the uplift as they correspond to the four localities with the most exposure of MFB and thereby the highest density of lineaments. The trend of 259 lineaments were measured from 0 to 180° , and values were mirrored in order to form a 360° plot. Mirrored rose diagrams were created for each of the four sections (Figs. 2.10). Structural mapping indicates that lineaments are radial and tangential to the central uplift.

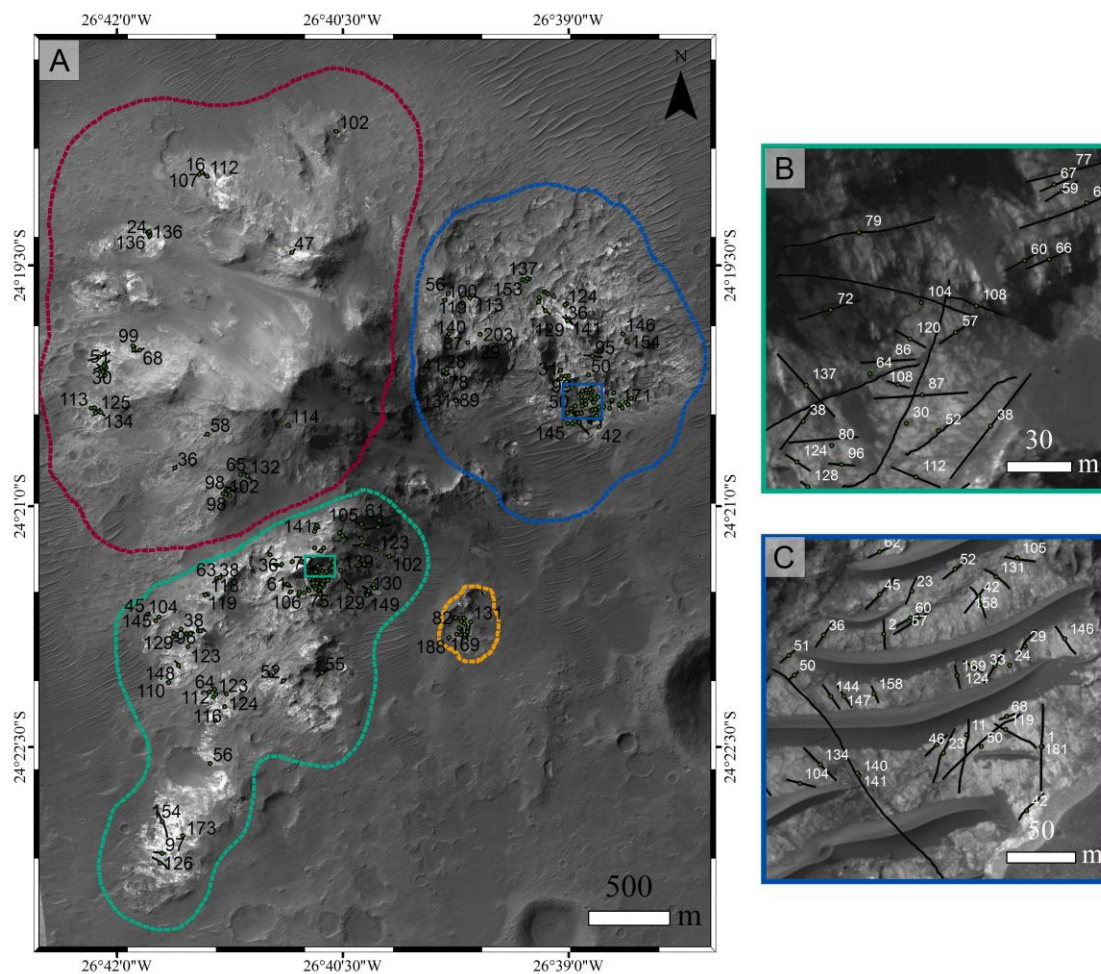


Figure 2.9. A: Structural mapping over HiRISE orthoimage showing lineaments cross-cutting the MFB. Dotted lines represent the three sections for which rose diagrams were produced (red: western, blue: eastern and green: southwestern). **B:** Southwestern section showing lineaments with preferential southwest-northeast trend. **C:** Eastern section showing lineaments with varying trends.

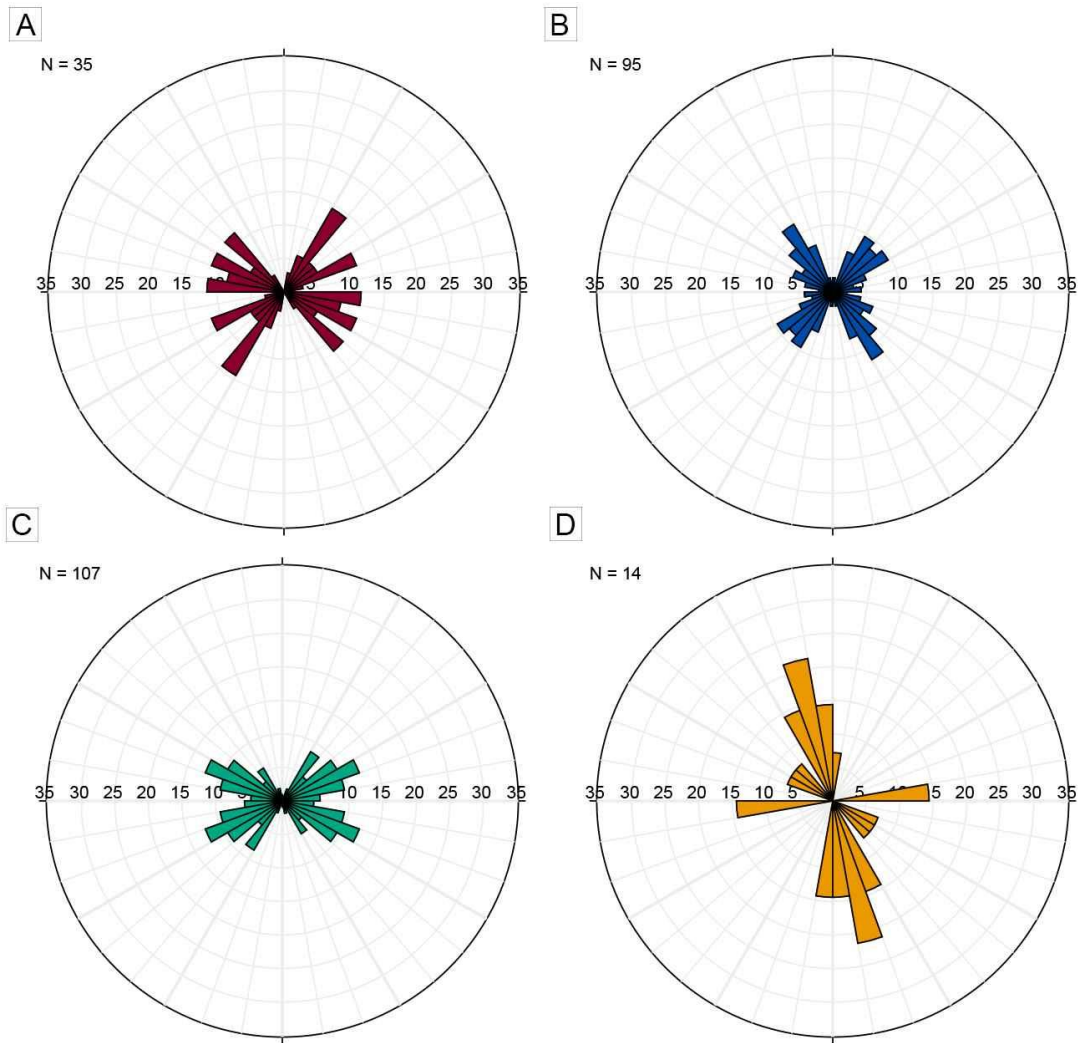


Figure 2.10. Stereonet rose diagrams of lineaments measured from 0 to 180 ° and mirrored in order to form a 360 ° plot for the central uplift of Alga Crater. A: Western section. B: Eastern section. C: Southwestern section. D: Southeastern section.

2.5 Discussion

2.5.1 Interpretation of morphological units

We have identified and described six distinct morphological units along with their associated structural attributes and inferred composition: (1) massive and fractured bedrock (MFB), (2) dark-toned clast-rich unit, (3) dark-toned clast-poor unit, (4) dark-toned pit-bearing unit, (5) unconsolidated materials, and (6) aeolian deposits. Below we present our interpretations and a discussion of these units.

2.5.1.1 Parautochthonous target rocks

The unit mapped as MFB is interpreted as pre-existing parautochthonous bedrock that was uplifted during the formation of Alga Crater. The morphometry, structure, tonality, and texture that characterize this unit in Alga is consistent with the MFB class observed by Tornabene et al. (2010, 2015) within 124 crater central uplifts on Mars. MFB has also been observed and described in some detail in the studies of Toro Crater (Marzo et al., 2010) and Ritchey Crater (Sun and Milliken, 2014; Ding et al., 2015). Importantly, many of the outcrops of MFB are partially draped (i.e., overlain) and embayed by materials interpreted to be allochthonous impactites (Fig. 2.11A), whereas other outcrops, such as in the northwestern and western sections of the uplift, are very well-exposed (Fig. 2.11B). It is difficult to establish whether these well-exposed areas were once draped by impactites that were subsequently eroded, or whether they were never covered to begin with. Statistical analysis reveals that exposures of MFB correspond to ~22% of the entire uplift, with the best exposures in the northwestern and western sections.

Based on the composition inferred from our spectral analysis, MFB appears to be enriched in olivine in the northwestern and western sections of the central uplift, whereas the remaining bulk of the uplift appears to be enriched in low-calcium pyroxene (LCP) (Fig. 2.6). This is generally consistent with the observations of Skok et al. (2012). MFB with the strongest spectral signature in LCP is recorded in the northwestern and western sections of the uplift (Fig. 2.7B). LCP-bearing MFB in the southwestern section of the uplift has relatively intermediate band depths, but a weaker LCP spectral absorption is

recorded for the eastern section of the uplift (Fig. 2.7C). The varying spectral absorptions of LCP in the central uplift of Alga could be due to brightening from contributions of a spectrally neutral component, as previously suggested by Skok et al. (2012). Furthermore, the highest thermal inertia values are constrained to the northwestern and western sections of the uplift where the best-exposed and most coherent bedrock is observed with HiRISE (up to $\sim 614 \text{ J m}^{-2} \text{ K}^{-1} \text{ s}^{-1/2}$). As such, MFB is consistent with previous interpretations that it must represent pre-impact bedrock materials exposed during the formation of the uplift (Tornabene et al., 2010, 2015).

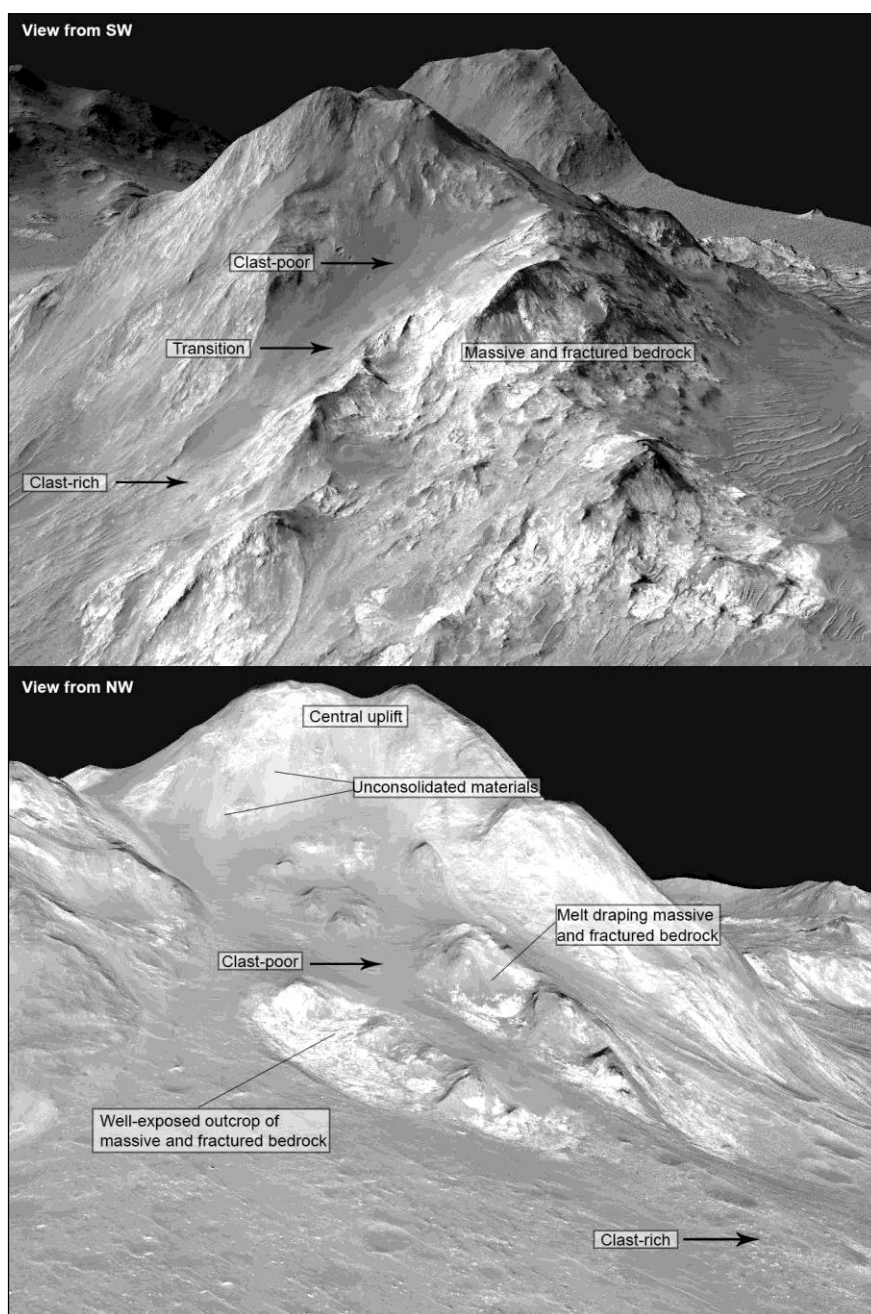


Figure 2.11. A: View from the southwest showing the transition between the clast-poor and clast-rich impact melt rocks, contained within outcrops of MFB. B: View from the northwest showing unconsolidated materials near the top of the uplift, overlying clast-poor impact melt rocks. Clast-poor impact melt is observed on both sides of a well-exposed outcrop of MFB, and grades into the clast-rich facie downward towards the crater floor.

2.5.1.2 Allochthonous crater-fill impactites

We propose that the 3 units mapped as dark-toned clast-rich, clast-poor and the pit-bearing units are all consistent with impactite deposits formed by Alga Crater. Impactite deposits result from the propagation of shock and rarefaction waves generated by the hypervelocity impact of a projectile into the target materials. Terrestrial impactites are subdivided according to their clast content (clast-poor, clast-rich, clast-free) and groundmass texture (phaneritic, aphanitic, vitric/glassy, vesicular, particulate, fragmental) (e.g., Osinski and Pierazzo (2012)). Impact melt rocks (i.e., impactites in which the matrix corresponds to melted target materials) in terrestrial complex impact structures formed in crystalline targets take the form of coherent sheets or lenses that generally overly parautochthonous target rocks at the crater floor and occur within the crater-fill, respectively (Grieve et al., 1977). Furthermore, the composition of impact melt rocks typically represents a chemical mixture of the melted target rocks (Grieve et al., 1977; Osinski et al., 2008).

Based on their characteristics of coating, embaying, and in some cases flowing with respect to local topography (Figs. 2.11), we suggest that the dark-toned clast-poor and clast-rich units correspond to impact melt rocks of varying clast content. Their stratigraphic setting is consistent with observations of impact melt rocks of Lunar craters (Hawke and Head, 1977), Earth (Grieve et al., 1977; Grieve and Cintala, 1992; Osinski and Pierazzo, 2013), and other Martian impact structures (Tornabene et al., 2010, 2015; Marzo et al., 2010; Osinski et al., 2011; Ding et al., 2015). In addition, the smooth and coherent texture of the dark-toned clast-poor unit, which directly grades into the clast-rich unit as observed in the western section of the uplift (Fig. 2.11A), has been noted in other Martian central uplifts (Tornabene et al., 2010, 2015; Osinski et al., 2011). We suggest that the clast-rich unit formed as a result of the dark-toned clast-poor impact melt incorporating lithic inclusions (clasts) from the underlying MFB and/or from the settling out of clasts from the clast-poor unit. The correlation of our morphological mapping with our compositional analysis corroborates both these interpretations and previous spectral results from Skok et al. (2012); over most of the central uplift, the CRISM mafic spectral parameter product (Fig. 2.6) shows stronger spectral absorptions in LCP for the clast-rich

impact melt rocks that are comparatively weaker in clast-poor deposits. Skok et al. (2012) attributed a dominantly bland spectral signature to impact melt (i.e., the dark-toned clast-poor unit), but noted a weak absorption in LCP. We interpret the LCP-rich deposits to have originated from the transient cavity lining (i.e., comprised of melts and breccias). Basically, these initial breccias and melt-bearing deposits were likely captured during the formation of the central uplift. The bulk of the bedrock of which the uplift is comprised (i.e., MFB) originates as part of and from below the transient cavity floor; as such, these rocks had to rise up through the transient cavity lining in order for the uplift to come to be in its current place of rest. Some of these melt-bearing deposits that coated the uplift must have remained hot enough to be affected by the newly formed topography of the uplift, and thereby subsequently flowed off the central peak. Evidence for later-stage flows comes from the correlation of clast-rich materials that possess an olivine-rich signature, and how these materials only occur where closely associated with exposures of olivine-rich MFB (Fig. 2.6). This is in contrast with the LCP-bearing clast-rich and clast-poor units, which occur over the bulk of the uplift without necessarily being closely associated with LCP-rich outcrops of MFB. Although impact melt rocks in Alga Crater could be of pre-impact origin (i.e., produced by previous impact events and excavated by Alga), the combined synthesis of our morphological mapping and compositional analysis offers a strong case for a syn-impact origin.

Previous studies of terrestrial impact structures demonstrated that impact melt rocks tend to be somewhat homogeneous in composition (Grieve et al., 1977; Dressler and Reimold, 2001; Osinski et al., 2008). Furthermore, the composition of impact melt rocks usually reflects the chemical mixture of the melted target rocks (Grieve et al., 1977; Osinski et al., 2008). Therein, we hypothesize that the pre-impact target rocks at Alga were predominantly enriched in low-calcium pyroxene, and that the impact yielded a considerable amount of crystalline (fine-grained) homogeneous melt with a varying clast content (clast-poor and clast-rich).

The dark-toned smooth-textured unit in Alga is observed to grade directly into the pit-bearing unit that is extensive throughout the crater floor (i.e., the primary crater-fill deposits) consistent with previous observations from other craters (Nuhn et al., 2015; Tornabene et al., 2015). Although eroded and degraded when compared to examples from previous work, this unit is consistent with the crater-related pitted materials, which are interpreted to be volatile-rich impact melt-bearing deposits (Tornabene et al., 2012). Pitted materials have been observed on crater floors, terraces, and ejecta blankets of impact structures with the best-preserved and least eroded conditions, and are consistent with the top of crater-fill and melt-bearing deposits (Boyce et al., 2012; Denevi et al., 2012; Tornabene et al., 2012).

The eroded pits in Alga range from ~5 to 340 m in diameter. Tornabene et al. (2012) provided two equations based on the best-preserved pitted-material bearing craters:

$$(1) D_{mp} = 27.5D_c^{0.86}$$

$$(2) D_{ap} = 16.4D_c^{0.87}$$

where D_{mp} is the maximum pit diameter (in metres), D_{ap} is the average pit diameter (in metres), and D_c is the host crater's diameter (in kilometres). This equation reveals that the maximum pit diameter increases with increasing crater diameter. For Alga Crater, the calculated $D_{mp} = \sim 345$ m is consistent with our measurement of the largest pit we observed (~ 340 m) and falls above the calculated average of $D_{ap} = \sim 212$ m. This supports our interpretation of the dark-toned pit-bearing unit as a partially eroded/degraded surface that is consistent with the crater-related pitted materials. This is also supported by the fact that the unit is extensive throughout the crater floor; as well as the observed transitions of clast-poor to clast-rich to pit-bearing unit. Therefore, we conclude that the pit-bearing unit at the base of the uplift and crater floor of Alga represents the topmost unit of the crater-fill deposits.

Schultz and Mustard (2004) proposed that impact melt rocks and glasses should be more abundant on Mars than previously thought. Spectral modeling of mixtures of quenched basaltic glass and crystalline phases such as olivine and pyroxene was recently reported by Cannon and Mustard (2015) in Alga and other craters using radiative transfer Hapke spectral mixture modeling. Our CRISM glass spectral parameter and summary colour composite (Fig. 2.12) reveals that the periphery of outcrops of olivine-bearing MFB, which we correlate to the dark-toned clast-rich impact melt rocks, are consistent with glass. Cannon and Mustard (2015) had a similar conclusion, in which they stated that glass-rich impactites are modeled at the margins of putative impact melt flows in the uplift of Alga.

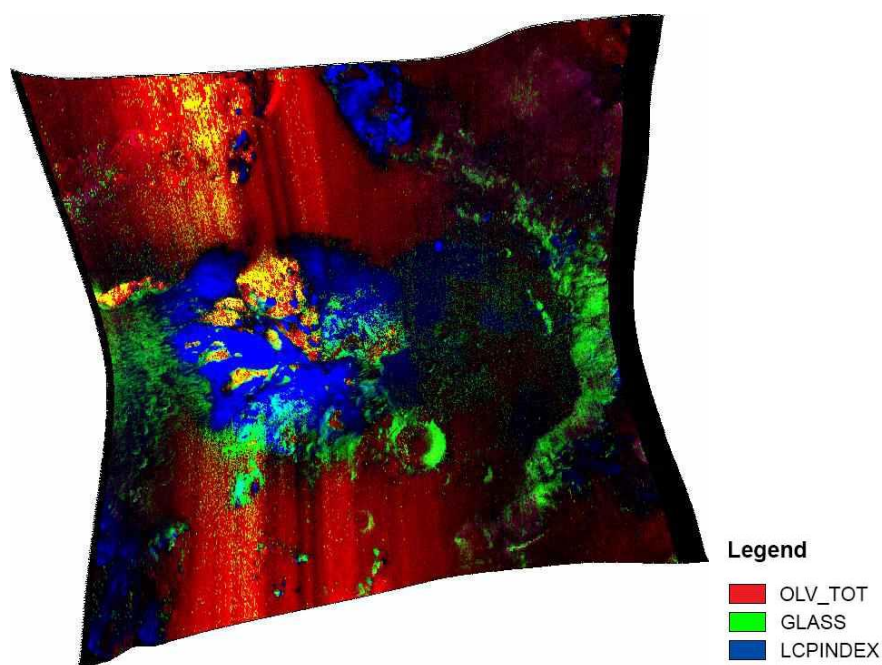


Figure 2.12. CRISM glass spectral parameter and summary colour composite (red: OLV_TOT, green : GLASS, blue : LCPINDEX; courtesy of Kevin Cannon and John “Jack” Mustard, Brown University) (see Cannon and Mustard, 2015 for details). Mixtures of glass and olivine are modeled around outcrops of olivine-bearing MFB in the western and northwestern sections of the central uplift.

Terrestrial field observations indicate that impact glass may be found in two main types of impactites: impact glass-bearing lithic breccias and impact melt rocks. In both types, rapid quenching of a melt into glasses is key. In impact melt rocks, this is typically where the melt is in contact with cooler bedrock and/or where it is charged with clasts (Onorato et al., 1978). We suggest that impact glass in the central uplift of Alga is the result of the rapid quenching of clast-laden melt at the contact with the uplifted target rocks.

In summary, although Alga Crater contains very good exposures of pre-impact target rocks (MFB), approximately 75% of its uplift is covered by what we interpret to be impact melt-bearing lithologies (i.e., dark-toned clast-poor and clast-rich units, dark-toned pit-bearing unit), which coated the parautochthonous target rocks during the uplift of the transient cavity floor.

2.5.1.3 Post-impact erosional units

Unconsolidated materials. Unconsolidated materials are observed on steep slopes in the very centre of the central uplift of Alga Crater (Fig. 2.4K). They are interpreted as mass wasting deposits. Relatively high thermal inertia values (Table 2.3) are attributed to the inclusion of boulders entrained during mass wasting events.

Aeolian deposits. The aeolian nature of these deposits are based on relatively low thermal inertia values (Ferguson et al., 2006) and abundant aeolian bedforms (Fig. 2.4L). These deposits may represent regionally-derived materials (Rogers et al., 2005; Tornabene et al., 2015) or be derived from the weathering of crater-fill deposits as a result of aeolian saltation of grains (Sullivan et al., 2005; Bridges et al., 2010).

Post-impact unconsolidated materials and aeolian deposits represent the topmost and youngest geological units occurring within the central uplift of Alga Crater. The identification and mapping of post-impact erosional units is essential as they not only overlay the exposed bedrock and crater-fill impactites, but also affect the exposure as well as thermal and spectral analysis of other intra-crater units (Tornabene et al., 2015).

2.5.2 Structure of the central uplift

Structural analysis is complicated by the fact that Alga is located in the centre of Chekalin Crater. We also know from previous field studies of terrestrial impact structures that a complex kinematic history is associated to target rocks exposed in the central uplifted area (Osinski and Spray, 2005). Alga has not only potentially uplifted the central uplift of Chekalin, but it is located in the vicinity of Ladon Basin and of the ~1,800 km diameter Argyre Basin.

Based on field studies at Meteor Crater, it has also been suggested that pre-existing structures (i.e., faults, joints, etc.) in the target rocks play a considerable role on the geometry of the transient cavity (Shoemaker and Kieffer, 1974). On the other hand, field studies at many complex impact structures have shown that during the excavation stage of crater formation, new structures in the target rocks can be generated, and have significant influence on the weakening of the target sequence prior to crater collapse in the subsequent modification stage (Osinski and Spray, 2005). Without the ability to conduct field-based studies, the assessment of the origin of structures in the central uplift of Alga Crater is challenging. However, structural mapping reveals that lineaments are broadly distributed in a radial and tangential patterns around the uplift, which is what was observed at the Haughton complex impact structure on Devon Island (Osinski and Spray, 2005) and in Ritchey Crater on Mars (Ding et al., 2015). Non-radial, non-concentric or even random lineaments would be expected for a pre-impact origin for the majority of these structural features. Thus, the distinct radial and tangential pattern of lineaments in the central uplift of Alga strongly suggests an impact-generated origin during the modification stage of crater formation (Kenkmann, 2002; Kenkmann et al., 2014). If Chekalin also had a radial and tangential pattern (or even something else more random or strongly oriented in some other way), that pattern would have been disturbed and reoriented (if sampled) by the Alga forming event.

2.5.3 Origin(s) of the exposed bedrock

The materials sampled by Alga may have experienced a complex history. Alga is located within a region that is in the vicinity of the multiring ~1,800 km diameter Argyre Basin, and within the ~88 km infilled and degraded Chekalin Crater, which, in turn, occurs within the heavily degraded potential multiring ~1,000 km diameter Ladon Basin.

Based on a revised maximum depth-to-diameter (d/D) ratio scaling relationship for Martian complex craters, $d=0.334D^{0.545}$, where d is the crater depth and D the diameter in km (Tornabene et al., 2013), Chekalin should have had an initial depth of ~3.8 km when it was newly formed. MOLA MEGDR point-to-point elevation data indicates a current rim-to-floor depth of ~800 m for Chekalin (Fig. 2.1C). This suggests that Chekalin Crater may have experienced infilling of materials up to a maximum of ~3 km of post-impact material.

For terrestrial complex craters, the stratigraphic uplift is determined using the equation $SU=0.086D_e^{1.03}$, where SU is the stratigraphic uplift and D_e is the final diameter in km (Grieve and Pilkington, 1996). While the accuracy of this equation is unknown for planetary bodies, it can be used to provide a broad estimate of stratigraphic uplift for Martian complex craters. Based on this equation, Chekalin Crater should have a SU of ~8.6 km, and Alga Crater, ~1.8 km. Thus, given the estimate of ~3 km of post-impact infill noted above, one would expect Alga's central uplift to be exposing the infill materials of Chekalin Crater. However, as we have demonstrated above, Alga's central uplift is quite clearly comprised of massive and fractured bedrock and not layered rocks, which would be indicative of post-impact sedimentary and/or volcanic infilling. The most plausible interpretation then is that the central uplift of Alga has exposed and uplifted the central uplift of Chekalin. This is consistent with the complete lack of high-calcium pyroxene (HCP) in the central uplift, which is typical in younger Hesperian-aged volcanic deposits (Mustard et al., 2005). Olivine, on the other hand, is detected in both ancient Noachian-aged terrains and younger Hesperian-aged volcanic flows. The most plausible interpretation then is that the central uplift of Alga has exposed and uplifted the

central uplift of Chekalin. This is consistent with the position of Alga within Chekalin (Fig. 2.1B). This then begs the question as to the nature of Chekalin's central uplift.

Generally, near-surface occurrences of olivine on differentiated planetary bodies are associated with geological processes such as volcanism and/or plutonism (Dhingra et al., 2015). Olivine-bearing deposits are extensively detected in the heavily cratered terrains of Mars, including around the three major impact basins on Mars (i.e., Hellas, Argyre, Isidis) (Hoefen et al., 2003; Hamilton and Christensen, 2005; Rogers et al., 2005; Bandfield and Rogers, 2008; Tornabene et al., 2008; Ody et al., 2013), and occurrences of olivine-bearing bedrock are recorded in Valles Marineris (Edwards et al., 2008). The formation of olivine on Mars has generally been ascribed to volcanic eruptions of ultramafic lava flows during the formation of the early Martian crust, from fractional crystallization and segregation in a magma chamber (Mustard et al., 2005), low degrees of partial melting of ultramafic sources (Tornabene et al., 2008) or from a global deep magma ocean (Elkins-Tanton et al., 2005; Skok et al., 2012). On the other hand, olivine among other minerals can also crystallize from impact melt (Osinski and Pierazzo, 2012).

Skok et al. (2012) noted a lack of mineral mixing in the VNIR between olivine and pyroxene. Correlations between our morphological mapping, compositional and thermophysical analysis reveal that olivine-bearing materials are well constrained to the northwestern and western sections of the uplift, and are interpreted to be more coherent than LCP-bearing outcrops (i.e., they have higher thermal inertias). Alternating exposures of olivine-bearing and LCP-bearing deposits are also observed within the western and eastern crater wall and terraces of Alga. These observations likely indicate a regional property of the subsurface, as demonstrated by Bandfield and Rogers (2008) across Argyre Planitia. Mustard et al. (2005) noted that regions richer in basalts such as Syrtis Major, southeastern Valles Marineris, and Terra Cimmeria are characterized by small exposures of what is interpreted as olivine-bearing crustal rocks excavated from depth by impact. Since the bulk of the uplift at Alga is characterized by LCP-bearing materials, we suggest that the pre-impact target lithology was predominantly enriched in LCP and that isolated occurrences of olivine-bearing materials were possibly resampled

by Chekalin and then by Alga. Both LCP-bearing and olivine-bearing bedrock could correspond to samples of the early Martian crust equivalent to gabbros, pyroxenite or peridotites.

2.6 Conclusions

Detailed morphological and structural mapping combined with spectral analysis and a synthesis of additional information provided by other datasets (e.g., MOLA, THEMIS thermal inertia, etc.) have revealed that the central uplift of Alga Crater is composed of relatively high thermal inertia olivine-bearing and low-calcium pyroxene-bearing massive and fractured bedrock (MFB) constrained to the northwestern and western sections of the uplift, and less coherent pyroxene-bearing MFB for the remaining bulk of the uplift. Parautochthonous target rocks (i.e., the MFB) are coated by crater-fill impact melt-bearing deposits that cover three quarters of the uplifted area, whereas widespread pitted materials across the southern crater floor correspond to the topmost surfaces of these deposits. Furthermore, the northern floor of Alga Crater is extensively covered by aeolian deposits, and unconsolidated materials are also observed in the central uplift. Determining the origin of MFB is complicated by the fact that Alga is located within a larger infilled complex crater (Chekalin), which is superposed on an inner ring of Ladon Basin, which, in turn, is located in the vicinity of Argyre Basin. We suggest that Alga uplifted and excavated the central uplift of Chekalin, and this would be consistent with scaling relationships and the relative position of Alga in the very centre of Chekalin. Overall, our detailed morphological and structural map of Alga Crater adds to the previous detailed spectral study conducted by Skok et al. (2012) in which they found that complex craters central uplifts in Argyre Planitia generally show enrichment in olivine and low-calcium pyroxene. Our structural mapping revealed that lineaments are oriented radially and concentrically to the central uplift, which is primarily attributed to the Alga-forming event, and consistent with structural assessments at terrestrial impact structures (e.g., Haughton impact structure, Devon Island; Ritchey Crater, Mars). Finally, this study further demonstrates the importance of correlating detailed morphological and

structural mapping with compositional analysis in order to assess the pre-, syn-, and post-impact origin of various materials that occur within Martian complex craters.

2.7 References

- Adams, J.B., 1974. Visible and near-infrared diffuse reflectance spectra of pyroxenes as applied to remote sensing of solid objects in the solar system. *J. Geophys. Res.* 79, 4829–4836.
- Adams, J.B., 1975. Interpretation of visible and near-infrared diffuse reflectance spectra of pyroxenes and other rock-forming minerals. in *Infrared and Raman Spectroscopy of Lunar and Terrestrial Materials* (C. Karr, ed.), Academic, New York, 91-116.
- Anderson, J.H., Wickersheim, K.A., 1964. Near infrared characterization of water and hydroxyl groups on silica surfaces. *Surf. Sci.* 2, 252–260.
- Bandfield, J.L., Hamilton, V.E., Christensen, P.R., 2000. A Global View of Martian Surface Compositions from MGS-TES. *Science.* 287, 1626–1630.
- Bandfield, J.L., Rogers, A.D., 2008. Olivine dissolution by acidic fluids in Argyre Planitia, Mars: Evidence for a widespread process? *Geology.* 36, 579–582.
- Barlow, G., Boyce, M., Costard, M., Craddock, A., Garvin, B., Sakimoto, E.H., Kuzmin, O., Roddy, J., Soderblom, L.A., 2000. Standardizing the nomenclature of Martian impact crater ejecta morphologies. *J. Geophys. Res.* 105, 26,733–26,738.
- Barlow, N.G., Bradley, T.L., 1990. Martian Impact Craters - Correlations of Ejecta and Interior Morphologies with Diameter, Latitude, and Terrain. *Icarus.* 87, 156–179.
- Bibring, J.-P., Langevin, Y., Gendrin, A., Gondet, B., Poulet, F., Berthé, M., Soufflot, A., Arvidson, R.E., Mangold, N., Mustard, J.F., Drossart, P., Team, O., 2005. Mars Surface Diversity as Revealed by the OMEGA/Mars Express Observations. *Science.* 307, 1576–1581.
- Boyce, J.M., Wilson, L., Mouginiis-Mark, P.J., Hamilton, C.W., Tornabene, L.L., 2012. Origin of small pits in martian impact craters. *Icarus.* 221, 262–275.

- Bridges, N.T., Banks, M.E., Beyer, R.A., Chuang, F.C., Noe Dobrea, E.Z., Herkenhoff, K.E., Keszthelyi, L.P., Fishbaugh, K.E., McEwen, A.S., Michaels, T.I., Thomson, B.J., Wray, J.J., 2010. Aeolian bedforms, yardangs, and indurated surfaces in the Tharsis Montes as seen by the HiRISE Camera: Evidence for dust aggregates. *Icarus*. 205, 165–182.
- Cannon, K.M., Mustard, J.F., 2015. Preserved glass-rich impactites on Mars. *Geology*. 43, 635–638.
- Chapman, C.R., Jones, K.L., 1977. Cratering and obliteration history of Mars. *Annu. Rev. Earth Planet. Sci.* 5, 515–540.
- Christensen, P.R., Jakosky, B.M., Kieffer, H.H., Malin, M.C., McEwen, H.Y., Neelson, K., Mehall, G.L., Silverman, S.H., Ferry, S., Caplinger, M.A., Ravine, M.A., 2004. The thermal emission imaging system (THEMIS) for the Mars 2001 Odyssey mission. *Space Sci. Rev.* 110, 85–130.
- Clark, R.N., Swayze, G.A., Wise, R., Livo, K.E., Hoefen, T.M., Kokaly, R.F., Sutley, S.J., 2007. USGS digital spectral library splib06a.
- Cloutis, E., Gaffey, J., 1991. Pyroxene spectroscopy revisited: Spectral-compositional correlations and relationship to geothermometry. *J. Geophys. Res.* 96, 22,809–22,826.
- Delamere, W.A., Tornabene, L.L., McEwen, A.S., Becker, K., Bergstrom, J.W., Bridges, N.T., Eliason, E.M., Gallagher, D., Herkenhoff, K.E., Keszthelyi, L., Mattson, S., McArthur, G.K., Mellon, M.T., Milazzo, M., Russell, P.S., Thomas, N., 2010. Color imaging of Mars by the High Resolution Imaging Science Experiment (HiRISE). *Icarus*. 205, 38–52.
- Denevi, B.W., Koeber, S.D., Robinson, M.S., Garry, W.B., Hawke, B.R., Tran, T.N., Lawrence, S.J., Keszthelyi, L.P., Barnouin, O.S., Ernst, C.M., Tornabene, L.L., 2012. Physical constraints on impact melt properties from Lunar Reconnaissance

- Orbiter Camera images. *Icarus*. 219, 665–675.
- Dhingra, D., Pieters, C.M., Head, J.W., 2015. Multiple origins for olivine at Copernicus crater. *Earth Planet. Sci. Lett.* 420, 95–101.
- Ding, N., Bray, V.J., McEwen, A.S., Mattson, S.S., Okubo, C.H., Chojnacki, M., Tornabene, L.L., 2015. The central uplift of Ritchey crater, Mars. *Icarus*. 252, 255–270.
- Dressler, B.O., Reimold, W.U., 2001. Terrestrial impact melt rocks and glasses. *Earth-Science Rev.* 56, 205–284.
- Edwards, C.S., Christensen, P.R., Hamilton, V.E., 2008. Evidence for extensive olivine-rich basalt bedrock outcrops in Ganges and Eos chasmas, Mars. *J. Geophys. Res. E Planets*. 113, 1–15.
- Elkins-Tanton, L.T., Hess, P.C., Parmentier, E.M., 2005. Possible formation of ancient crust on Mars through magma ocean processes. *J. Geophys. Res. E Planets*. 110, 1–11.
- Fergason, R.L., Christensen, P.R., Kieffer, H.H., 2006. High-resolution thermal inertia derived from the Thermal Emission Imaging System (THEMIS): Thermal model and applications. *J. Geophys. Res.* 111, 1–22.
- Grieve, R.A.F., Cintala, M.J., 1992. An analysis of differential impact melt-crater scaling and implications for the terrestrial impact record. *Meteoritics*. 27, 526–538.
- Grieve, R.A.F., Dence, M.R., Robertson, P.B., 1977a. Cratering processes: As interpreted from the occurrences of impact melts. *Impact Explos. Cratering Planet. Terr. Implic.* 1, 791–814.
- Grieve, R.A.F., Dence, M.R., Robertson, P.B., 1977b. Cratering processes-As interpreted from the occurrence of impact melts, in: *Impact and Explosion Cratering: Planetary and Terrestrial Implications*. pp. 791–814.

- Grieve, R.A.F., Pilkington, M., 1996. The signature of terrestrial impacts. *AGSO J. Aust. Geol. Geophys.* 16, 399–420.
- Guinness, E.A., Arvidson, R.E., Slavney, S., 1996. The Planetary Data System Geosciences Node. *Planet. Space Sci.* 44, 13–22.
- Hamilton, V.E., Christensen, P.R., 2005. Evidence for extensive, olivine-rich bedrock on Mars. *Geology.* 33, 433–436.
- Hawke, B.R., Head, J.W., 1977. Impact melt on lunar crater rims, in: *Impact and Explosion Cratering: Planetary and Terrestrial Implications.* pp. 815–841.
- Hoefen, T.M., Clark, R.N., Bandfield, J.L., Smith, M.D., Pearl, J.C., Christensen, P.R., 2003. Discovery of Olivine in the Nili Fossae Region of Mars. *Science.* 302, 627–630.
- Kenkmann, T., 2002. Folding within seconds. *Geology.* 30, 231–234.
- Kenkmann, T., Poelchau, M.H., Wulf, G., 2014. Structural geology of impact craters. *J. Struct. Geol.* 62, 156–182.
- King, T.V.V., Ridley, W.I., 1987. Relation of the Spectroscopic Reflectance of Olivine to Mineral Chemistry and Some Remote Sensing Implications. *J. Geophys. Res.* 92, 11,457–11,469.
- Kirk, R.L., Howington-Kraus, E., Rosiek, M.R., Anderson, J.A., Archinal, B.A., Becker, K.J., Cook, D.A., Galuszka, D.M., Geissler, P.E., Hare, T.M., Holmberg, I.M., Keszthelyi, L.P., Redding, B.L., Delamere, W.A., Gallagher, D., Chapel, J.D., Eliason, E.M., King, R., McEwen, A.S., 2008. Ultrahigh resolution topographic mapping of Mars with MRO HiRISE stereo images: Meter-scale slopes of candidate Phoenix landing sites. *J. Geophys. Res. E Planets.* 113, 1–31.

- Malin, M.C., Bell, J.F., Cantor, B.A., Caplinger, M.A., Calvin, W.M., Clancy, R.T., Edgett, K.S., Edwards, L., Haberle, R.M., James, P.B., Lee, S.W., Ravine, M.A., Thomas, P.C., Wolff, M.J., 2007. Context Camera Investigation on board the Mars Reconnaissance Orbiter. *J. Geophys. Res.* 112, 1–25.
- Marzo, G.A., Davila, A.F., Tornabene, L.L., Dohm, J.M., Fairén, A.G., Gross, C., Kneissl, T., Bishop, J.L., Roush, T.L., McKay, C.P., 2010. Evidence for Hesperian impact-induced hydrothermalism on Mars. *Icarus*. 208, 667–683.
- McEwen, A.S., Eliason, E.M., Bergstrom, J.W., Bridges, N.T., Hansen, C.J., Delamere, W.A., Grant, J.A., Gulick, V.C., Herkenhoff, K.E., Keszthelyi, L., Kirk, R.L., Mellon, M.T., Squyres, S.W., Thomas, N., Weitz, C.M., 2007. Mars Reconnaissance Orbiter's High Resolution Imaging Science Experiment (HiRISE). *J. Geophys. Res.* 112, 1–40.
- McGuire, P.C., Bishop, J.L., Brown, A.J., Fraeman, A.A., Marzo, G.A., Frank Morgan, M., Murchie, S.L., Mustard, J.F., Parente, M., Pelkey, S.M., Roush, T.L., Seelos, F.P., Smith, M.D., Wendt, L., Wolff, M.J., 2009. An improvement to the volcano-scan algorithm for atmospheric correction of CRISM and OMEGA spectral data. *Planet. Space Sci.* 57, 809–815.
- Mellon, M., Jackosky, B.M., Kieffer, H.H., Christensen, P.R., 2000. High-Resolution Thermal Inertia Mapping from the Mars Global Surveyor Thermal Emission Spectrometer. *Icarus*. 148, 437–455.
- Murchie, S., Arvidson, R., Bedini, P., Beisser, K., Bibring, J.-P., Bishop, J., Boldt, J., Cavender, P., Choo, T., Clancy, R.T., Darlington, E.H., Des Marais, D., Espiritu, R., Fort, D., Green, R., Guinness, E., Hayes, J., Hash, C., Heffernan, K., Hemmler, J., Heyler, G., Humm, D., Hutcheson, J., Izenberg, N., Lee, R., Lees, J., Lohr, D., Malaret, E., Martin, T., McGovern, J.A., McGuire, P., Morris, R., Mustard, J., Pelkey, S., Rhodes, E., Robinson, M., Roush, T., Schaefer, E., Seagrave, G., Seelos, F., Silverglate, P., Slavney, S., Smith, M., Shyong, W.-J., Strohhahn, K., Taylor, H., Thompson, P., Tossman, B., Wirzburger, M., Wolff, M., 2007. Compact

Reconnaissance Imaging Spectrometer for Mars (CRISM) on Mars Reconnaissance Orbiter (MRO). *J. Geophys. Res.* 112, 1–57.

Murchie, S.L., Seelos, F.P., Hash, C.D., Humm, D.C., Malaret, E., McGovern, J.A., Choo, T.H., Seelos, K.D., Buczkowski, D.L., Morgan, M.F., Barnouin-Jha, O.S., Nair, H., Taylor, H.W., Patterson, G.W., Harvel, C.A., Mustard, J.F., Arvidson, R.E., McGuire, P., Smith, M.D., Wolff, M.J., Titus, T.N., Bibring, J.P., Poulet, F., 2009. Compact Reconnaissance Imaging Spectrometer for Mars investigation and data set from the Mars Reconnaissance Orbiter's primary science phase. *J. Geophys. Res. E Planets.* 114, 1–15.

Mustard, J.F., Murchie, S.L., Pelkey, S.M., Ehlmann, B.L., Milliken, R.E., Grant, J.A., Bibring, J.-P., Poulet, F., Bishop, J., Dobreá, E.N., Roach, L., Seelos, F., Arvidson, R.E., Wiseman, S., Green, R., Hash, C., Humm, D., Malaret, E., McGovern, J.A., Seelos, K., Clancy, T., Clark, R., Marais, D.D., Izenberg, N., Knudson, A., Langevin, Y., Martin, T., McGuire, P., Morris, R., Robinson, M., Roush, T., Smith, M., Swayze, G., Taylor, H., Titus, T., Wolff, M., 2008. Hydrated silicate minerals on Mars observed by the Mars Reconnaissance Orbiter CRISM instrument. *Nature.* 454, 305–309.

Mustard, J.F., Poulet, F., Gendrin, A., Bibring, J., Langevin, Y., Gondet, B., Mangold, N., 2005. Olivine and Pyroxene Diversity in the Crust of Mars. *Science.* 307, 1594–1598.

Nuhn, A.M., Tornabene, L.L., Osinski, G.R., McEwen, A.S., 2015. Morphologic and structural mapping of the central uplift of Betio crater, Thaumasia Planum, Mars. *Geol. Soc. Am. Spec. Pap.* 518, 65–83.

Ody, A., Poulet, F., Bibring, J.P., Loizeau, D., Carter, J., Gondet, B., Langevin, Y., 2013. Global investigation of olivine on Mars: Insights into crust and mantle compositions. *J. Geophys. Res. E Planets.* 118, 234–262.

- Onorato, P.I.K., Hlmann, D.R.U., Simonds, C.H., 1978. The Thermal History of the Manicouagan Impact Melt Sheet, Quebec. *J. Geophys. Res.* 83, 2789–2798.
- Osinski, G.R., Grieve, R.A.F., Collins, G.S., Marion, C., Sylvester, P., 2008. The effect of target lithology on the products of impact melting. *Meteorit. Planet. Sci.* 43, 1939–1954.
- Osinski, G.R., Lee, P., Spray, J.G., Parnell, J., Lim, D.S.S., Bunch, T.E., Cockell, C.S., Glass, B., 2005. Geological overview and cratering model for the Haughton impact structure, Devon Island, Canadian High Arctic. *Meteorit. Planet. Sci.* 40, 1759–1776.
- Osinski, G.R., Pierazzo, E., 2012. *Impact cratering: Processes and products*. John Wiley & Sons. 330 pp.
- Osinski, G.R., Spray, J.G., 2005. Tectonics of complex crater formation as revealed by the Haughton impact structure, Devon Island, Canadian High Arctic. *Meteorit. Planet. Sci.* 40, 1789–1812.
- Osinski, G.R., Tornabene, L.L., Banerjee, N.R., Cockell, C.S., Flemming, R., Izawa, R.M., McCutcheon, J., Parnell, J., Preston, L.J., Pickersgill, A.E., Pontefract, A., Sapers, H.M., Southam, G., 2013. Impact-generated hydrothermal systems on Earth and Mars. *Icarus.* 224, 347–363.
- Osinski, G.R., Tornabene, L.L., Grieve, R.A.F., 2011. Impact ejecta emplacement on terrestrial planets. *Earth Planet. Sci. Lett.* 310, 167–181.
- Pan, C., Rogers, A.D., Michalski, J.R., 2015. Thermal and near-infrared analyses of central peaks of Martian impact craters: Evidence for a heterogeneous Martian crust. *J. Geophys. Res.* 120, 662–688.
- Parente, M., 2008. A new approach to denoising CRISM images. 39th Lunar Planet. Sci. Conf. Abstract # 2528.

- Pelkey, S.M., Mustard, J.F., Murchie, S., Clancy, R.T., Wolff, M., Smith, M., Milliken, R.E., Bibring, J.-P., Gendrin, A., Poulet, F., Langevin, Y., Gondet, B., 2007. CRISM multispectral summary products: Parameterizing mineral diversity on Mars from reflectance. *J. Geophys. Res. E Planets*. 112, 1–18.
- Rogers, D.A., Christensen, P.R., Bandfield, J.L., 2005. Compositional heterogeneity of the ancient Martian crust: Analysis of Ares Vallis bedrock with THEMIS and TES data. *J. Geophys. Res.* 110, 1–26.
- Schultz, P.H., Mustard, J.F., 2004. Impact melts and glasses on Mars. *J. Geophys. Res.* 109, 1–23.
- Shoemaker, E.M., Kieffer, S.E., 1974. Synopsis of the geology of Meteor Crater. Guideb. to Geol. Meteor Crater, Arizona, ASU Cent. Meteor. Stud. Publ 17, 1–11.
- Skok, J.R., Mustard, J.F., Tornabene, L.L., Pan, C., Rogers, D.A., Murchie, S.L., 2012. A spectroscopic analysis of Martian crater central peaks: Formation of the ancient crust. *J. Geophys. Res.* 117, 1–33.
- Sullivan, R.J., Banfield, D., Bell, J.F., Calvin, W.M., Fike, D.A., Golombek, M.P., Greeley, R., Grotzinger, J.P., Herkenhoff, K.E., Jerolmack, D., Malin, M.C., Ming, D.W., Soderblom, L. a, Squyres, S.W., Thompson, S., Watters, W.A., Weitz, C.M., Yen, A., 2005. Aeolian processes at the Mars Exploration Rover Meridiani Planum landing site. *Nature*. 436, 58–61.
- Sun, V.Z., Milliken, R.E., 2014. The geology and mineralogy of Ritchey crater, Mars: Evidence for post-Noachian clay formation. *J. Geophys. Res. Planets*. 119, 810–836.
- Tanaka, K.L., Robbins, S.J., Fortezzo, C.M., Skinner, J.A., Hare, T.M., 2014. The digital global geologic map of Mars: Chronostratigraphic ages, topographic and crater morphologic characteristics, and updated resurfacing history. *Planet. Space Sci.* 95, 11–24.

- Tornabene, L., Osinski, G.R., Barlow, N.G., Bray, V.J., Caudill, C.M., D'Aoust, B., Ding, N., Hopkins, R., Nuhn, A.M., Mayne, A., McEwen, A.S., 2015. Meter- to decameter-scale characteristics of central uplifts revealed by the Mars Reconnaissance Orbiter. *Bridg. Gap* III 5–6.
- Tornabene, L.L., Ling, V., Osinski, G.R., Boyce, J.M., Harrison, T.N., McEwen, A.S., 2013. Identification of the deepest craters on Mars based on the preservation of pitted impact melt-bearing deposits. in: 44th Lunar Planet. Sci. Conf. Abstract # 2592.
- Tornabene, L.L., McEwen, A.S., Caudill, C., Osinski, G.R., Wray, J.J., Marzo, G.A., Mustard, J.F., Skok, J.R., 2010. A Crater-Exposed Bedrock Database for Mars With Applications for Determining the Composition and Structure of the Upper Crust. in: 41st Lunar Planet. Sci. Conf. Abstract # 1737.
- Tornabene, L.L., Moersch, J.E., McSween, H.Y., Hamilton, V.E., Piatek, J.L., Christensen, P.R., 2008. Surface and crater-exposed lithologic units of the Isidis Basin as mapped by coanalysis of THEMIS and TES derived data products. *J. Geophys. Res.* 113, 1–30.
- Tornabene, L.L., Osinski, G.R., McEwen, A.S., Boyce, J.M., Bray, V.J., Caudill, C.M., Grant, J.A., Hamilton, C.W., Mattson, S.S., Mouginis-Mark, P.J., 2012. Widespread crater-related pitted materials on Mars: Further evidence for the role of target volatiles during the impact process. *Icarus.* 220, 348–368.
- Tornabene, L.L., Osinski, G.R., McEwen, A.S., Wray, J.J., Craig, M.A., Sapers, H.M., Christensen, P.R., 2013. An impact origin for hydrated silicates on Mars: A synthesis. *J. Geophys. Res. Planets* 118, 994–1012.
- Wyatt, M., McSween, H., 2002. Spectral evidence for weathered basalt as an alternative to andesite in the northern lowlands of Mars. *Nature.* 417, 263–266.

Zuber, M.T., Smith, D.E., Solomon, S.C., Muhleman, D.O., Head, J.W., Garvin, J.B., Abshire, J.B., Bufton, J.L., 1992. The Mars Observer Laser Altimeter Investigation. *J. Geophys. Res.* 97, 7781–7797.

Zurek, R.W., Smrekar, S.E., 2007. An overview of the Mars Reconnaissance Orbiter (MRO) science mission. *J. Geophys. Res. E Planets.* 112, 1–22.

Chapter 3

3 Morphological, Structural and Spectral Mapping of the Central Uplift of Verlaine Crater, Sabae Terra, Mars

3.1 Introduction

Impact craters are the most common landforms on the surface of most of the terrestrial planets and moons of our Solar System. Since very few terrestrial impact structures are well-preserved or exposed (Kenkmann et al., 2005, 2014), Mars represents an excellent site for the study of impact cratering processes. Central uplifts within complex impact craters have been targeted for the study of the Martian crust as they are known to exhume deep subsurface material (Tornabene et al., 2010, 2015; Quantin et al., 2012; Caudill et al., 2012). A global crater-exposed bedrock geodatabase compiled by Tornabene et al. (2010) using data derived from instruments onto the Mars Reconnaissance Orbiter (MRO) and Mars Odyssey (MO) spacecrafts has recorded ~200 Martian complex craters for which morphological, structural, and spectral diversity have been recognized (Tornabene et al., 2015). From the surveying of High Resolution Imaging Science Experiment (HiRISE) images at the decametre- to metre-scale, Tornabene et al. (2010) have documented three distinct textural types of exposed bedrock in central uplifts: layered bedrock (LB), massive and fractured bedrock (MFB) and megabrecciated bedrock (MBB). While complex craters are often compared as windows to the subsurface, the exposed bedrock in central uplifts is rarely well-exposed because of degradation, infilling, dust mantling, obscuration by impact melt coatings and other deposits including dust, unconsolidated and regionally derived materials (Tornabene et al., 2010, 2015; L.L. Tornabene et al., 2013; Osinski et al., 2013). The geology of central uplifts is complicated by the fact that exposed materials could have been previously excavated and redistributed by prior impact events.

Spectral reflectance data from the Observatoire pour la Minéralogie, l'Eau, les Glaces, et l'Activité (OMEGA) and subsequently from the Compact Reconnaissance Imaging Spectrometer for Mars (CRISM) have shown that the distribution of phyllosilicates is closely correlated to the ancient heavily cratered terrains of Mars. Phyllosilicates have been primarily detected within the crater rims, walls, ejecta deposits, and central uplifts of complex craters (Poulet et al., 2005; Bibring et al., 2006; Wray et al., 2008; Mustard et al., 2008; Murchie et al., 2009; Ehlmann et al., 2009, 2011; Carter et al., 2010; Tornabene et al., 2013). Although the formation of hydrated silicates has generally been associated to an early warm and wet Mars (Poulet et al., 2005; Bibring et al., 2006), an impact origin is another viable scenario (Tornabene et al., 2013) that has been suggested from the results of the detailed mapping of complex craters. In fact, recent morphological and spectral studies have suggested that impact-generated hydrothermal activity could have formed hydrated silicates in the central uplifts of Toro, Majuro and Holden Craters (McEwen et al., 2009; Tornabene et al., 2009; Marzo et al., 2010; Mangold et al., 2012a; Osinski et al., 2013).

In this study, we conducted decametre- to metre-scale morphological, structural, and spectral mapping of the central uplift of the ~39 km diameter Verlaine Crater selected from the geodatabase compiled by Tornabene et al. (2010, 2015). The uplift primarily comprises the massive and fractured bedrock (MFB) class, but also includes exposures of the megabrecciated bedrock (MBB) class. This study leverages off of the results from our previous study on Alga Crater (Chapter 2) and intends to: 1) inform on the origin of both textural classes of bedrock, 2) place further constraints on the types and emplacement of impact melt-bearing lithologies, and 3) inform on the formation of central uplifts in massive/complex targets and on the origin of impact megabreccias. Through detailed cartographical mapping, we hope to increase the understanding behind the impact cratering process and the mechanics of central uplift formation respectively.

3.2 General Geological setting: Verlaine Crater

Verlaine Crater (64.1 °E, -9.2 °S) is a ~39 km diameter well-preserved complex crater located within the southern heavily cratered highlands of Mars bordering Terra Sabae and Tyrrhena Terra. The region is bounded to the south by Hellas Planitia, and by Syrtis Major Planum to the north (Fig. 3.1A). More specifically, Verlaine is located in the vicinity of the ~450 km diameter peak ring Huygens structure, and appears to be superposed on a degraded impact basin (northern rim) that is almost the same size as Huygens to the west. It occurs within the middle Noachian highland unit (mNh) (Tanaka et al., 2014), but is also located near the boundary of the early Noachian highland unit (eHn). The mNh unit has been interpreted as undifferentiated impact, volcanic, fluvial, and basin materials that are moderately to heavily degraded (Tanaka et al., 2014). Based on the general elevation of this terrain and the size and proximity of the Hellas Basin, the basin materials mentioned in the above description are likely dominated by Hellas Basin ejecta.

The northeastern crater rim is cross-cut by one branch of an unnamed valley network located just north of Verlaine Crater (Fig. 3.1B). The valley network has a north-south orientation and appears to have flown south towards Verlaine. The branches forming this valley network measure between ~30–40 km in length (Hynek et al., 2010). Elevation ranges from ~2,500 m at the northern and southern crater rims and ~400–700 m at the crater floor (Fig. 3.1C). The central uplift reaches a maximum elevation of ~810 m, hence it rises approximately ~100–400 m with respect to the elevation of the crater floor.

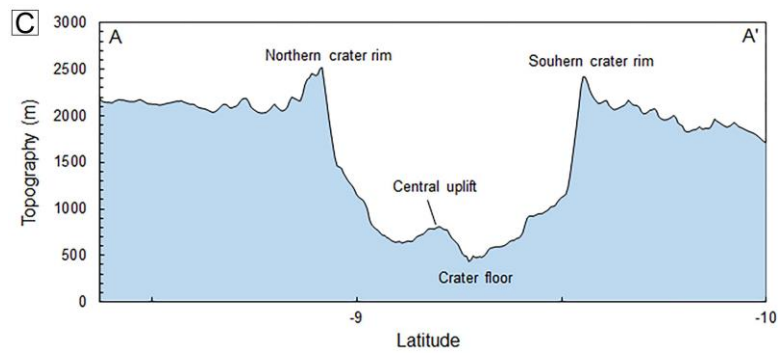
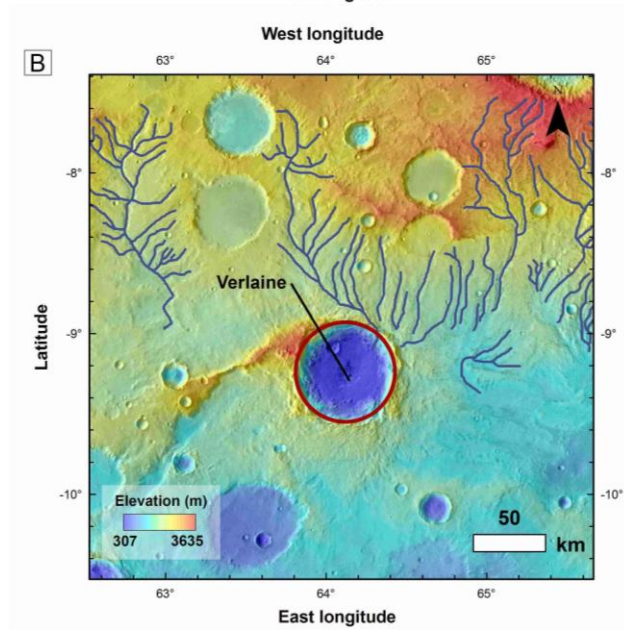
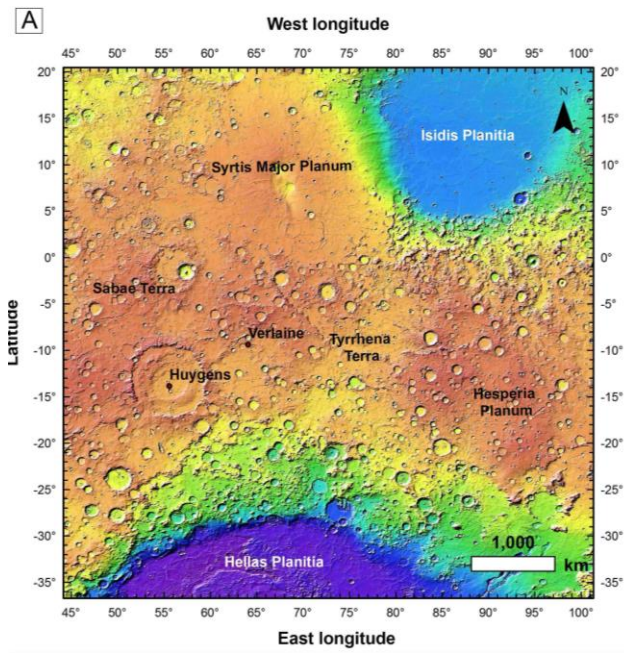


Figure 3.1. A: MOLA MEGDR colourized hillshade showing the geographical setting of the study area. B: A close-up showing the extent of Verlaine Crater and the northeastern section of the rim cross-cut by valley networks. C: A MOLA-derived north-south topographic profile of Verlaine Crater.

3.3 Methodology

The general methodology outlined in Chapter 2 was also used for this study. We acquired Mars Reconnaissance Orbiter (MRO) datasets: High Resolution Imaging Science Experiment (HiRISE) (McEwen et al., 2007), Context Camera (CTX) (Malin et al., 2007) and Compact Reconnaissance Imaging Spectrometer for Mars (CRISM) (Murchie et al., 2007). In addition, we used supplemental datasets such as topography from Mars Orbiter Laser Altimeter (MOLA) (Zuber et al., 1992), thermophysical characteristics from Thermal Emission Imaging System (THEMIS) (Christensen et al., 2004) derived thermal inertia (TI) (Ferguson et al., 2006) and High Resolution Stereo Camera (HRSC) for regional context (Neukum et al., 2004).

3.3.1 Datasets

Table 3.1. Orbital datasets used in this study.

Instruments	Data product ID	Resolution
HiRISE	ESP_013635_1705_RED_B_01_ORTHO	50 cm/pixel
	ESP_013213_1705_IRB_B_01_ORTHO	50 cm/pixel
	DTEED_013213_1705_013635_1705_A01	2.02 m/pixel
CTX	B09_013213_1707_XN_09S295W	5.24 m/pixel
	B10_013635_1707_XN_09S295W	5.71 m/pixel
	B17_016114_1712_XN_08S295W	5.24 m/pixel
	D13_032465_1727_XI_07S296W	5.27 m/pixel
CRISM	FRT00012CD9_07_IF164	18 m/pixel
MOLA	Global Colorized Hillshade 90Nto90S	463 m/pixel
THEMIS	Controlled Mosaic Day and Night IR Iapygia 30S-45E	100 m/pixel
	THEMIS-derived thermal inertia I02114005	100 m/pixel
HRSC	H6387_0000_ND3	10 m/pixel

Morphological mapping was conducted at a scale of 1:5,000 in the ArcMap platform of ArcGIS and using a HiRISE-derived Digital Terrain Model (DTM) for 3D perspective. Trend of lineaments were measured using the DigSym ArcGIS add-on tool and mirrored rose diagrams were plotted in Stereonet (see Chapter 2 for a more detailed description of the methodology).

Spectral analysis was conducted using CRISM Analysis Tool (CAT) v.7.2.1 in Exelis ENVI based on the general procedures described by Murchie et al. (2007, 2009).

Photometric and atmospheric corrections were applied to the calibrated TRDR v3 data products. Spectral summary products were created for the NIR (S) and IR (L) images in addition to hyperspectral summary products for the IR image (Pelkey et al., 2007; Murchie et al., 2009b). Band threshold ROIs were defined and intersected with ROIs delineating specific morphological features, then ratioed to nearby spectrally bland areas located along the same column of the detector. Ratioed spectra were compared to laboratory spectra of the USGS and CRISM spectral libraries (Clark et al., 2007; <http://speclab.cr.usgs.gov/spectral.lib06>) for mineral identification. A CRISM spectral parameter and summary colour composite (red: D2300, green: OLINDEX2, blue: BD1900R) was created to illustrate alteration parameters.

Themis-derived thermal inertia was determined for the best-exposed localities of each morphological units in ENVI, and the average and standard deviation values were recorded.

3.4 Results

Verlaine Crater (Figs. 3.2) possess a central uplift with a morphology that is rather complex, including an off-centered irregular depression (Fig. 3.2C), but it is more consistent with a central peak rather than a central pit feature. The uplift is approximately ~10 km by ~8 km, and occupies an area of ~58 km². A 5-km crater occurs northwest of the central uplift with its ejecta covering some of the materials that occur on the northern slopes of the uplift area.

Below we describe each mapped units, and a summary of their physical attributes is provided in Table 3.2. Figure 3.3 is a simplified morphological map of the central uplift of Verlaine Crater.

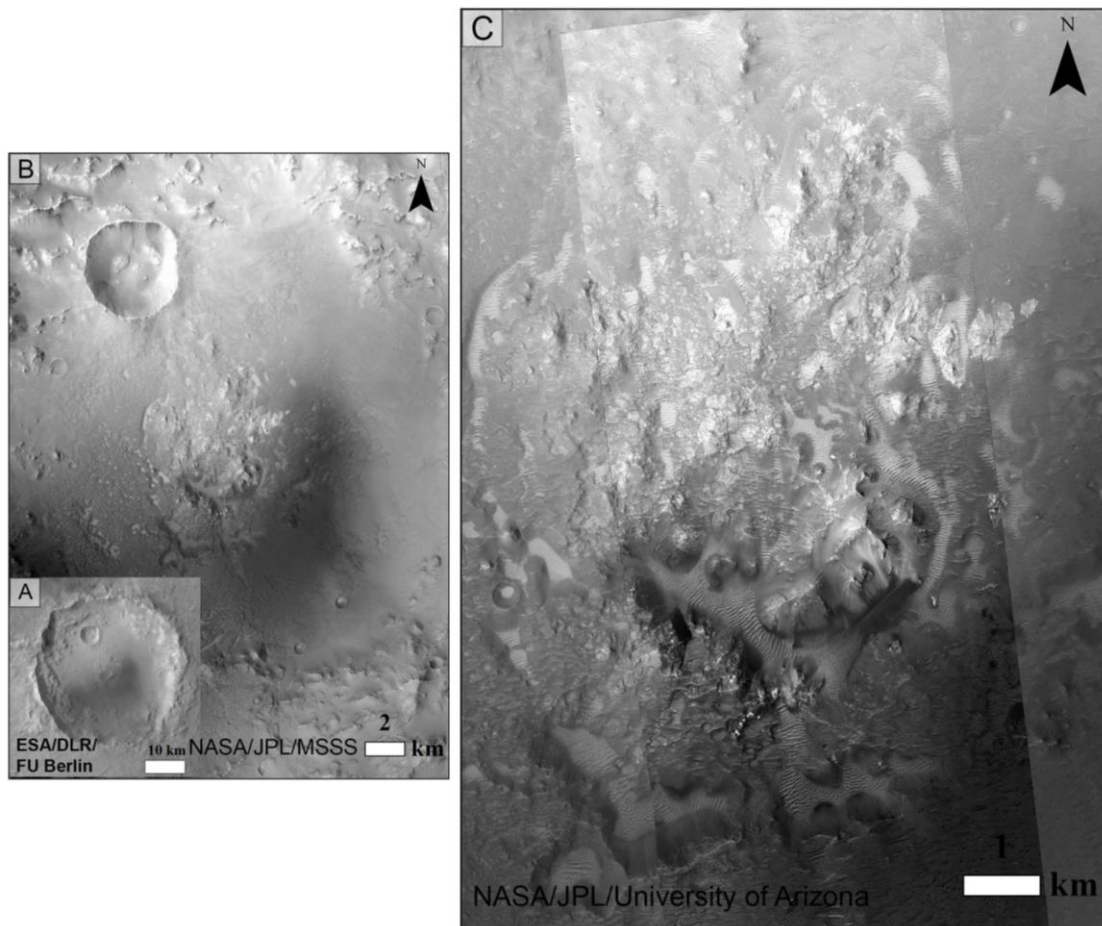


Figure 3.2. A: HRSC image H6387_0000_ND3 of Verlaine Crater and showing the 5 km crater northwest the central uplift of Verlaine. B: CTX image B09_013213_1707_XN_09S295W of the central uplift and floor of Verlaine Crater. C: HiRISE RED orthoimage ESP_013635_1705 overlying CTX image showing the central uplift of Verlaine Crater.

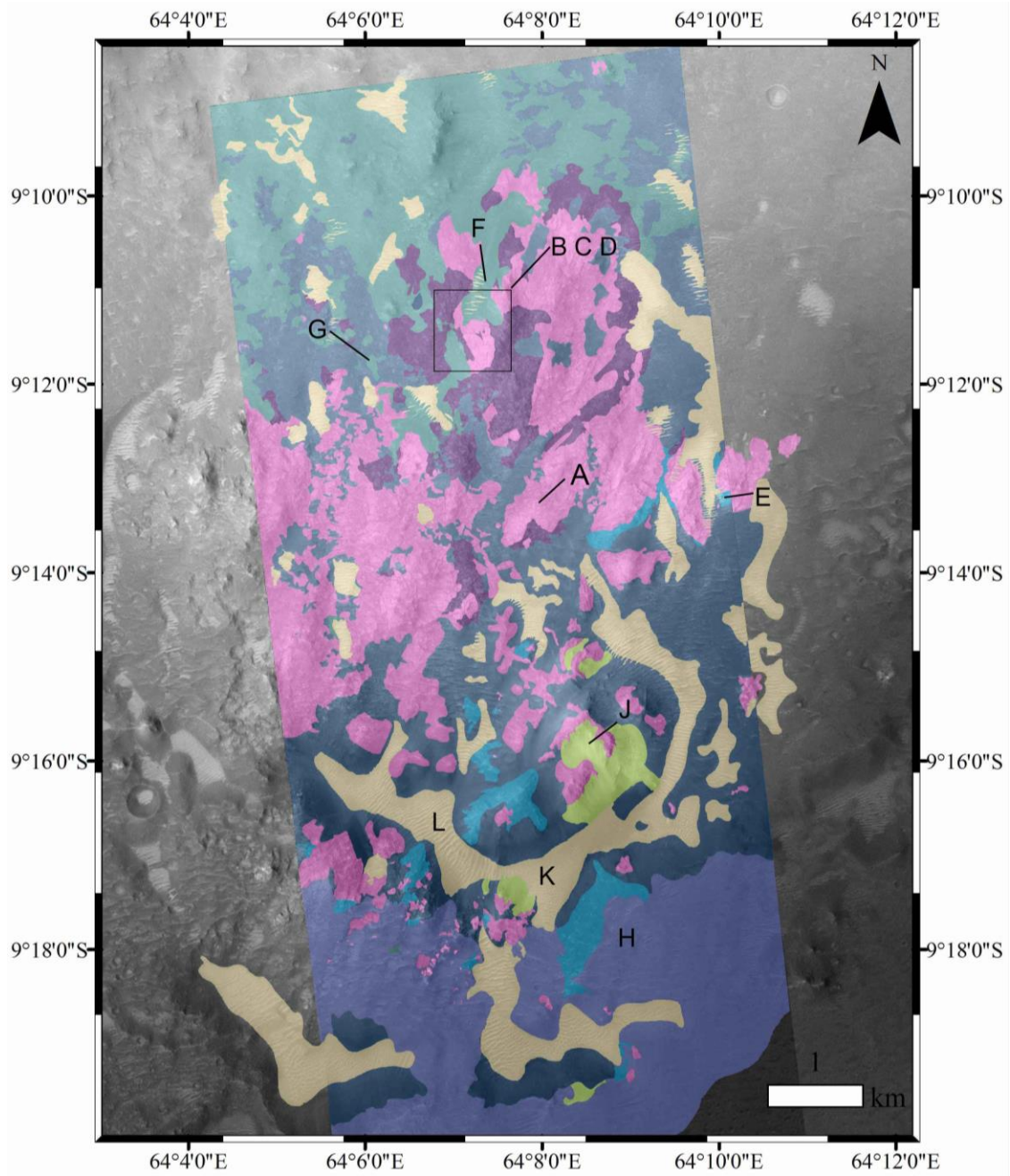
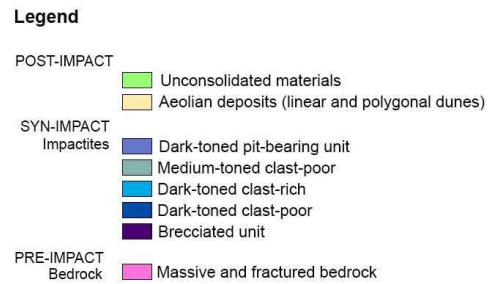


Figure 3.3. Morphological map of the central uplift of Verlainé Crater over HiRISE RED orthoimage ESP_013635_1705.

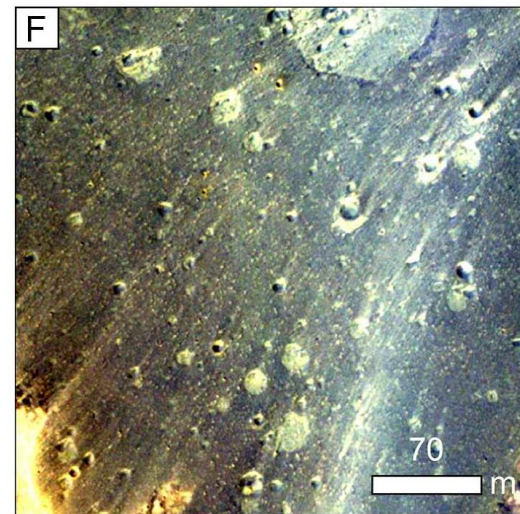
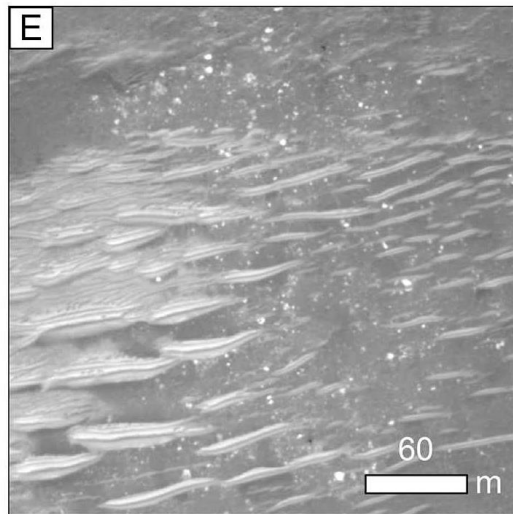
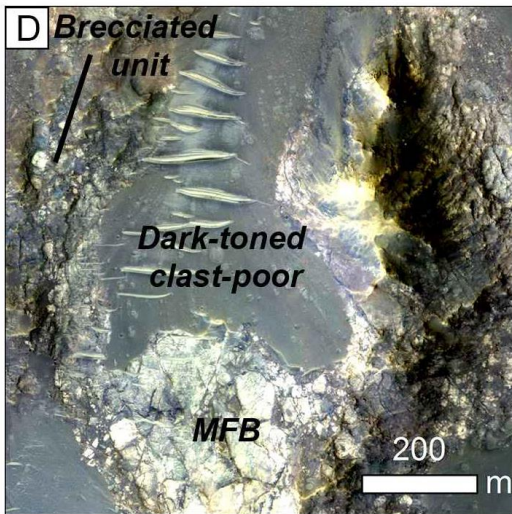
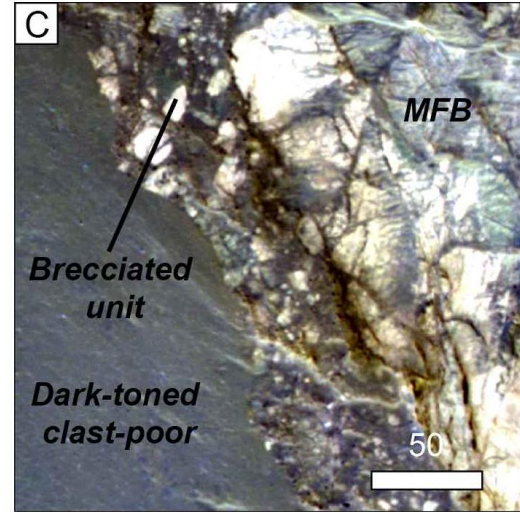
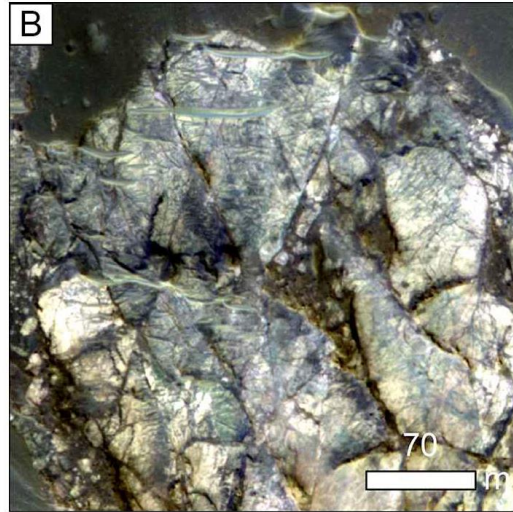
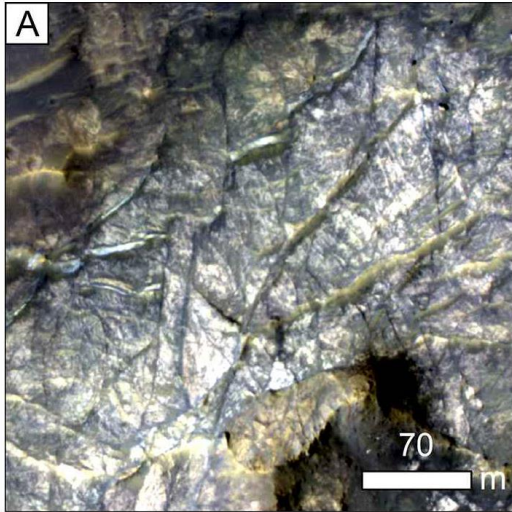


3.4.1 Massive and fractured bedrock (MFB) unit

The lightest-toned materials observed in CTX and HiRISE imagery correspond to outcrops of massive and fractured bedrock (MFB) and possibly some comparatively minor occurrences of megabrecciated bedrock (MBB). The MFB is cross-cut by pervasive dark-toned linear and quasi-linear features (Figs. 3.4A, B, C). The majority of the exposure of MFB occurs north of the off-centered irregular depression. MFB covers an area of $\sim 11.3 \text{ km}^2$ ($\sim 19.6\%$) and occurs on slopes averaging 12° (std. dev. ~ 8) in the central uplift (Table 3.2). Of all the units mapped in Verlaine, this unit possesses the highest thermal inertias (avg. $\sim 453 \text{ J m}^{-2} \text{ K}^{-1} \text{ s}^{-1/2}$, std. dev. ~ 42) (Table 3.3.)

Table 3.2. Properties of each morphological units.

Unit Name	HiRISE-derived DTM Slope				Area (km ²)	Percentage (%)
	Max.	Min.	Avg.	Std.Dev.		
Massive and fractured bedrock	88.4	0.0	11.5	7.8	11.3	19.6
Megabreccia	40.1	0.0	6.3	3.7	2.9	5.0
Dark-toned clast-rich	61.9	0.0	11.5	7.8	0.9	1.5
Dark-toned clast-poor	85.0	0.0	9.1	6.6	15.7	27.2
Medium-toned clast-poor	80.4	0.0	5.8	3.9	7.6	13.2
Dark-toned pit-bearing unit	85.4	0.0	9.8	6.2	10.3	17.8
Unconsolidated materials	72.7	0.1	20.5	9.0	0.8	1.4
Aeolian deposits	57.8	0.0	7.4	5.3	8.3	14.3



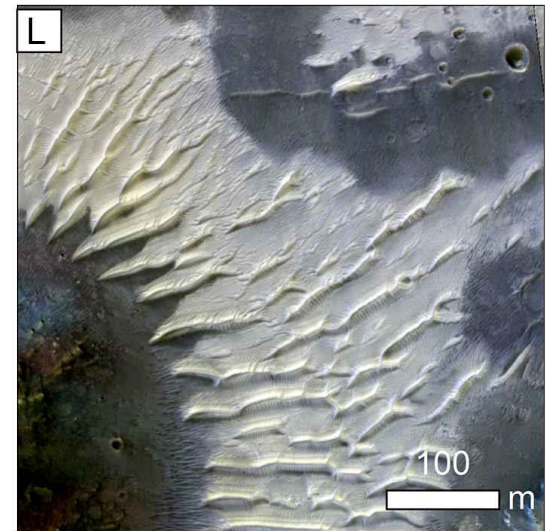
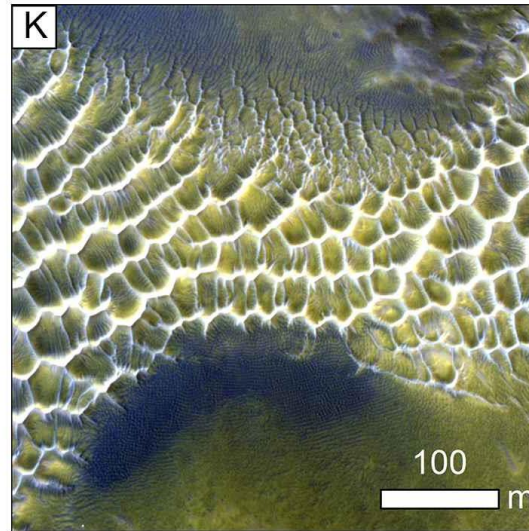
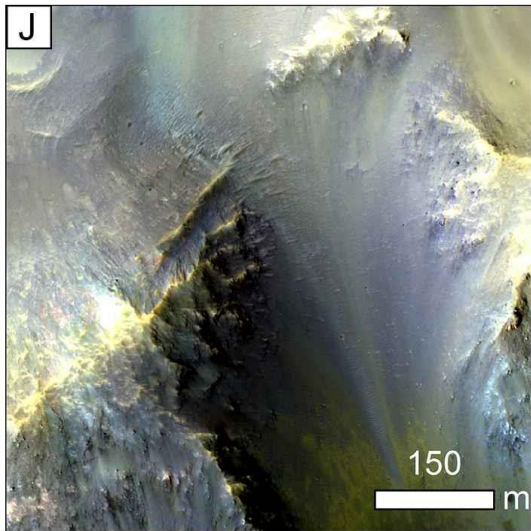
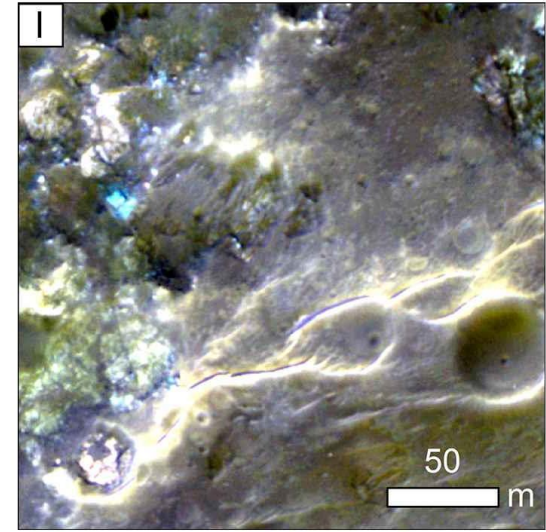
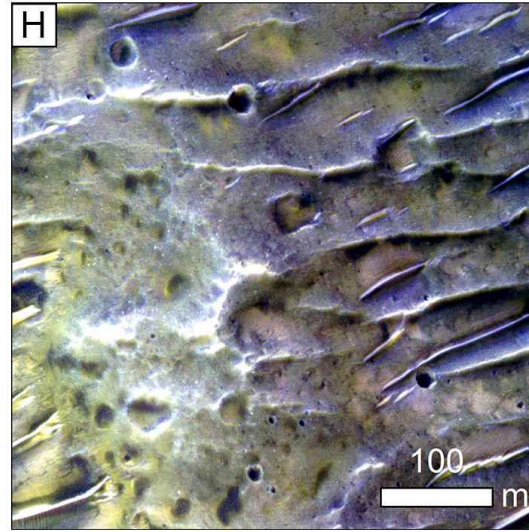
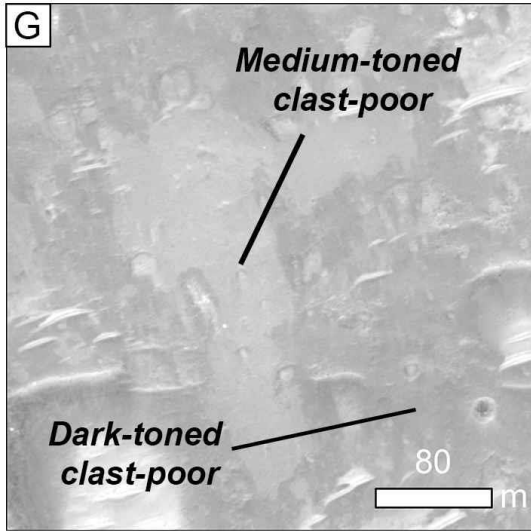


Figure 3.4. Morphological units. HiRISE RED orthoimage ESP_013635_1705 and IRB image ESP_013635_1705. Refer to Fig. 2.3 to view location of each morphological units indicated by the letter ID. A-B: MFB in the central uplift. C: Dark-toned clast-poor unit (left) contiguous to brecciated unit (centre) and to the MFB (right). Note the sharp contact between the dark-toned clast-poor and brecciated units. D: MFB and brecciated unit coated by the dark-toned clast-poor unit in the central uplift. E: Dark-toned clast-rich unit in the eastern section of the uplift. F: Dark-toned clast-poor unit observed in the central uplift. G: Dark-toned clast-poor unit overlain by the medium-toned clast-poor unit in the northern section of the uplift. H: Dark-toned pit-bearing unit overlain by aeolian deposits. I: Dark-toned pit-bearing unit with clast-rich deposits at the southern crater floor. J: Unconsolidated materials in the southern section of the uplift. K: Aeolian bedforms (network dunes) within the off-centered irregular depression at the south of the uplift. L: Aeolian bedforms (linear dunes) in the southern section of the uplift.

Table 3.3. Themis-derived thermal inertia for each morphological units.

Unit Name	Thermal inertia	
	<u>Avg.</u>	<u>Std. Dev.</u>
Massive and fractured bedrock	453	42
Megabreccia	412	22
Dark-toned clast-rich	381	21
Dark-toned clast-poor	296	14
Medium-toned clast-poor	313	15
Dark-toned pit-bearing unit	364	16
Unconsolidated materials	419	43
Aeolian deposits	279	6

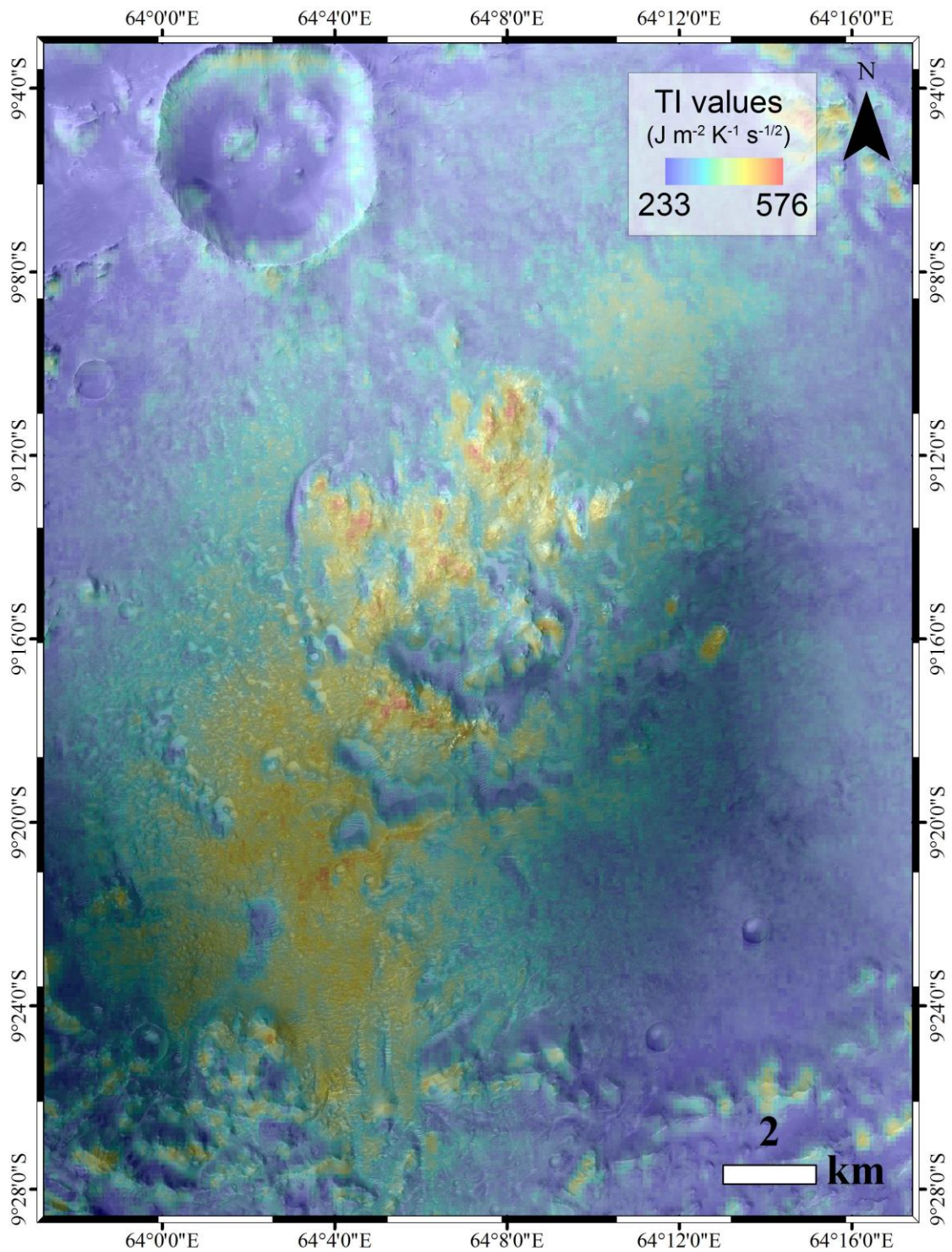


Figure 3.5. Themis-derived thermal inertia map overlying HiRISE RED orthoimage ESP_013635_1705 of Verlainé Crater (stretch 233 to 576 $\text{J m}^{-2} \text{K}^{-1} \text{s}^{-1/2}$).

One topographically high-standing outcrop shows a strong spectral signature in olivine, which also correlates with the highest thermal inertia. It appears in bright green in the CRISM colour composite (Fig. 3.6). The extracted CRISM spectra (Fig. 3.7A1, A2) (see Table 3.4 for ROIs and bland areas coordinates) show a broad absorption feature centered at $\sim 1 \mu\text{m}$ indicative of a ferrous iron band (Adams, 1974), and is generally consistent with olivine. An olivine laboratory spectrum (olivineKI3188) from the USGS spectral library is provided for comparison (Fig. 3.7B). Furthermore, from the CRISM colour composite (Fig. 3.6), a correlation is observed between the OLINDEX2 and D2300 hyperspectral and spectral summary products (areas in yellow). One extracted spectrum for the D2300 parameter revealed absorption features at ~ 1.9 and $\sim 2.31 \mu\text{m}$ and possibly a $1.4 \mu\text{m}$ feature (Figs. 3.7C1). Two outcrops of the MFB in the northern section of the uplift correlate with the BD1900R parameter. Extracted spectra show absorption features at $1.9 \mu\text{m}$ (Figs. 3.7D1, D2), indicative of bound H_2O . We used a laboratory spectrum of the Fe-rich smectite endmember nontronite (nontroniteNDJB26) from the CRISM phyllosilicates spectral library for comparison (Fig. 3.7E).

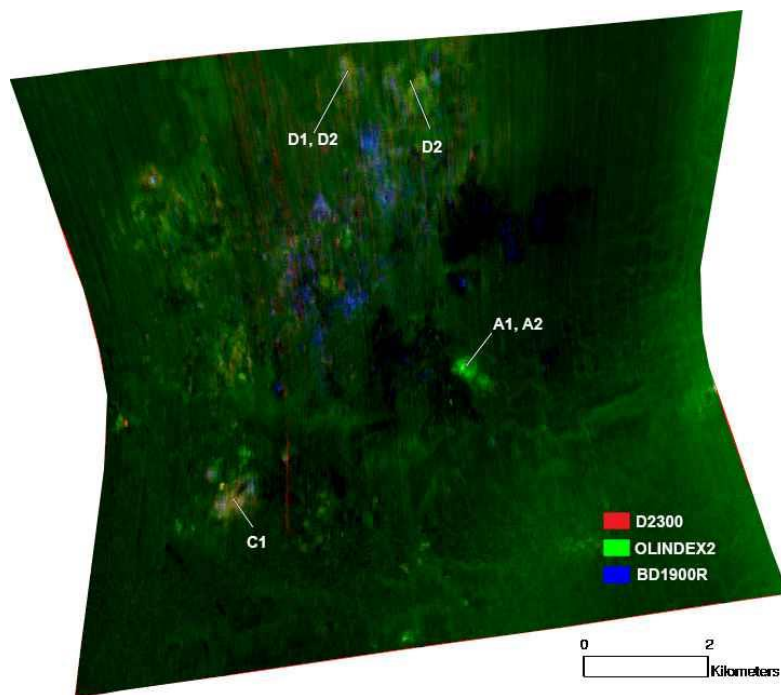


Figure 3.6. CRISM colour composite (Red: D2300 0.000-0.035, Green: OLINDEX2 0.000-0.124, Blue: BD1900R 0.000-0.020).

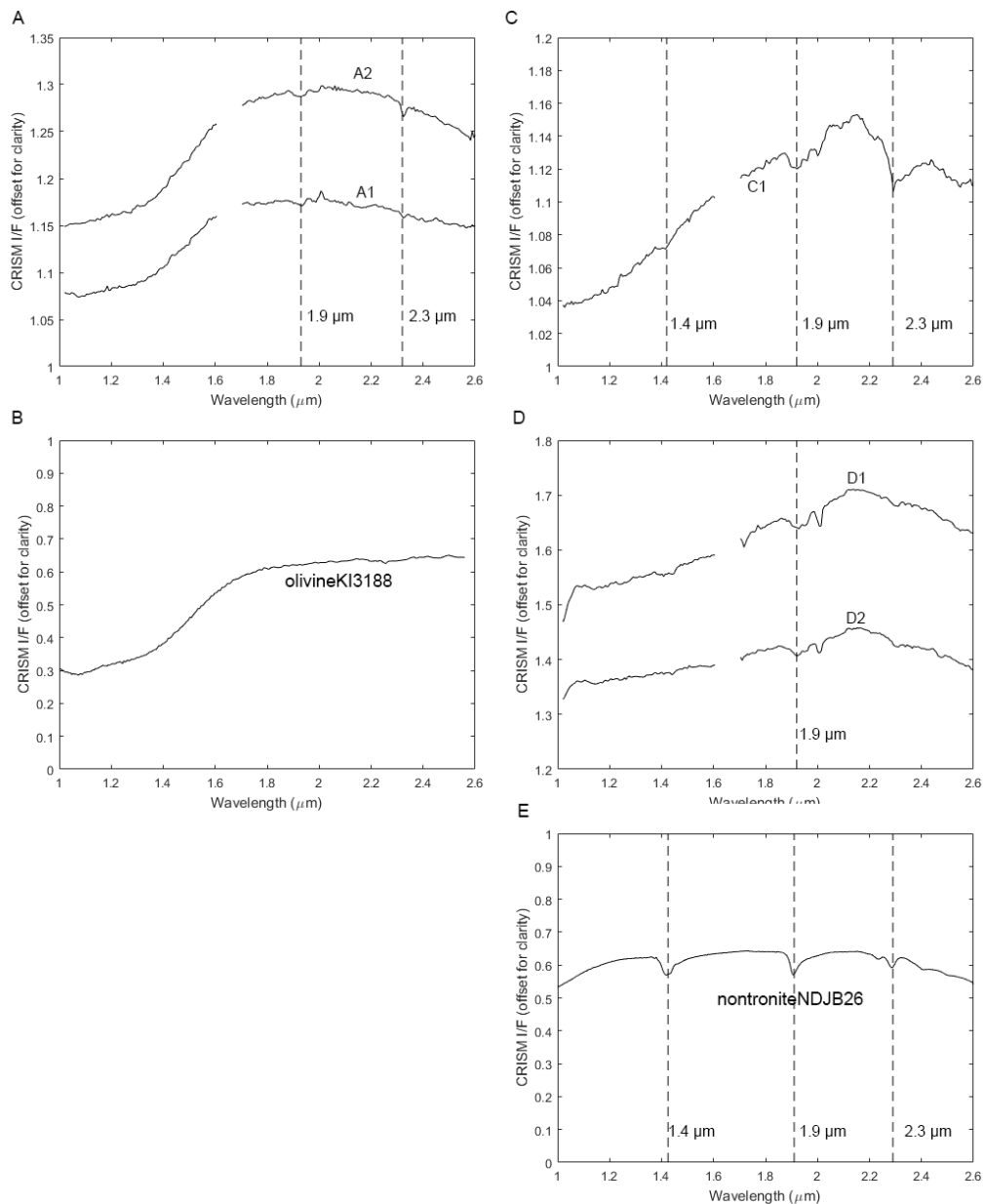


Figure 3.7. Ratioed CRISM I/F spectra extracted from FRT00012CD9_07_IF164. A: OLINDEX spectra taken on a topographic high-standing outcrop in the central uplift. B: Laboratory spectrum olivineKI3188 from the USGS digital spectral library splib01. C: D2300 spectra from the MFB in the southwestern section of the uplift. D: BD1900R from the MFB in the northern section of the uplift. E: Laboratory spectrum nontronite NDJB26 from the CRISM phyllosilicates spectral library.

Table 3.4. CRISM spectra regions of interest (ROIs) and denominators.

CRISM summary products	Morphological units	ROI X	ROI Y	ROI size (pixels)	Bland area X	Bland area Y	Bland area size (pixels)	Band threshold	IDs
OLINDEX	MFB	274	182	32	266	244	255	0.09-0.124	A1
OLINDEX	MFB	274	182	32	272	52	943	0.09-0.124	A2
D2300	MFB	504	92	17	496	27	171	0.02-0.07	B1
BD1900R	MFB	395	336	22	405	93	87	0.012-0.43	C1
BD1900R	MFB	346, 395	370, 336	45	405	93	87	0.012-0.43	C2

3.4.2 Brecciated unit

This unit is composed of poorly sorted angular to sub-angular light-toned multicoloured (polymict) megacrysts within a fine-grained dark-toned matrix (Fig. 3.3). In Verlaine, the megacrysts of this unit range from ~5 to 60 m in size and possess different colours in the HiRISE IRB image. This unit is always observed to be in contact with the MFB unit (Figs. 3.4C, D), and like the MFB unit is restricted to the northern section of the uplift where it is generally exposed on relatively low slopes (avg. $\sim 6^\circ$, std. dev. ~ 4) (Table 3.2). The brecciated unit shares a sharp contact with the dark-toned clast-poor unit (see section 3.4.4), and also appears to underlie it (Fig. 3.4C). This unit occupies an area of $\sim 2.9 \text{ km}^2$ ($\sim 5.0\%$ of the central uplift), and possess relatively high thermal inertia (avg. $\sim 412 \text{ J m}^{-2} \text{ K}^{-1} \text{ s}^{-1/2}$, std. dev. ~ 22) (Table 3.3) along with the MFB unit. We have also identified one exposure of the brecciated unit that possesses both $\sim 1.9 \mu\text{m}$ and $\sim 2.31 \mu\text{m}$ absorptions. However, there is insufficient exposure and spectral signature to resolve as to whether these spectral features are associated with the megacrysts or the dark-toned matrix that contains them.

3.4.3 Dark-toned clast-rich unit

This unit is characterized by poorly sorted angular to sub-angular light-toned clasts ranging from ~1 to 25 m in size that are embedded in a fine-grained dark-toned matrix (Fig. 3.4E), which is indistinguishable from the dark-toned clast-poor unit (see section 3.4.4). It is mostly found in the eastern section of the uplift (Fig. 3.3). This unit has an area of $\sim 0.9 \text{ km}^2$ ($\sim 1.5\%$), occurs on relatively intermediate topography (avg. $\sim 12^\circ$, std. dev. ~ 8) (Table 3.2), and has higher thermal inertia than the dark-toned clast-poor unit, but lower than the MFB unit (avg. $\sim 381 \text{ J m}^{-2} \text{ K}^{-1} \text{ s}^{-1/2}$, std. dev. ~ 21) (Table 3.3).

3.4.4 Dark-toned clast-poor unit

This smooth-textured and preferentially crater-retaining unit (i.e., coherent) is observed across the entire central uplift (Fig. 3.3). It is often observed to be draping the MFB (Figs. 3.4C, D). In other instances, it appears to have been removed or possibly eroded away, exposing the underlying MFB or brecciated unit (Fig. 3.4C). The dark-toned clast-poor unit also extensively covers the southern crater floor, before grading directly into the dark-toned pit-bearing unit (see section 3.4.6). At the northern crater floor, it is contiguous to, or often overlain by the medium-toned clast-poor unit (Fig. 3.4G). Overall, this unit occupies a major area of the uplift ($\sim 16 \text{ km}^2$, or $\sim 27\%$ of the central uplift), is found on both steep and gentler slopes (avg. $\sim 9^\circ$, std. dev. ~ 7) (Table 3.2), and possess some of the lowest thermal inertia (avg. $\sim 296 \text{ J m}^{-2} \text{ K}^{-1} \text{ s}^{-1/2}$, std. dev. ~ 14) (Table 3.3),

3.4.5 Medium-toned clast-poor unit

This unit is strictly observed at the crater floor north of the central uplift. This unit exhibits a lighter tonality than the dark-toned clast-poor unit (Fig. 3.4G), which drapes the majority of the uplift. It is observed to grade into, but in some rare cases overlay, the dark-toned clast-poor unit (Fig. 3.4G). This unit accounts for $\sim 7.6 \text{ km}^2$ or $\sim 13.2\%$ of the central uplift, and occurs on relatively gentle slopes (avg. $\sim 6^\circ$, std. dev. ~ 4) (Table 3.2). The thermal inertia for this unit ranges between the values for the dark-toned clast-poor and -rich units (avg. $\sim 313 \text{ J m}^{-2} \text{ K}^{-1} \text{ s}^{-1/2}$, std. dev. ~ 15) (Table 3.3).

3.4.6 Dark-toned pit-bearing unit

This unit is best exposed in a small area in the southern section of the uplift, but careful observations indicate that it completely embays the central uplift (Fig. 3.3). The dark-toned clast-poor unit generally grades into the dark-toned pit-bearing unit. The best exposures of this unit correspond to shallow subdued pits, and quasi-arcuate and -circular ridges (Fig. 3.4H). It is overlain and partially obscured by aeolian bedforms particularly in the southern section of the uplift (Fig. 3.4H), and by the modified ejecta deposits from a $\sim 5\text{-km}$ crater that occurs just to the northwest of the uplift (Fig. 3.2). Measurable pit

diameters range from ~30–500 m. Light-toned multicoloured clasts are sometimes observed along pit slopes (Fig. 3.4I). This unit covers ~10.3 km² (~17.8% of the uplift), occurs on gentle slopes (avg. ~10 °, std. dev. ~16) (Table 3.2), and has higher thermal inertia than the dark- and medium-toned clast-poor units (avg. ~364 J m⁻² K⁻¹ s^{-1/2}, std. dev. ~16) (Table 3.3).

3.4.7 Unconsolidated materials

This unit consists of light-toned unconsolidated materials or alternatively light-toned streaks of loose material that are observed on the steepest slopes (avg. ~21 °, std. dev. ~9) of the uplift (Fig. 3.4J). Unconsolidated materials account for ~0.8 km² (~1.4%) of the uplift and have relatively high thermal inertia values (avg. ~419 J m⁻² K⁻¹ s^{-1/2}, std. dev. ~43) (Table 3.3).

3.4.8 Aeolian deposits

This unit consists of areas covered by both network (Fig. 3.4K) and linear (Fig. 3.4L) dunes. Linear dunes are observed in the uplift and on the southern and northern crater floors, and possess preferential west-east, southwest-northeast, and southeast-northwest orientations. On the northern crater floor, aeolian bedforms overlay the dark-toned and medium-toned clast-poor units. At the southern crater floor, they overlay the dark-toned pit-bearing unit. Network dunes are observed on the floor of the off-centered irregular depression that surrounds a series of uplifted outcrops in the southern section of the uplift (Fig. 3.3). Network dunes are also observed within low-lying depressions part of the dark-toned pit-bearing unit. Overall, this unit covers ~8.3 km² (~14.3%) of the uplift, occurs on relatively flat slopes (avg. ~7 °, std. dev. ~5) (Table 3.2), and possesses some of the lowest average thermal inertia values (avg. ~265 J m⁻² K⁻¹ s^{-1/2}, std. dev. ~6) relative to the other units in the uplift (Table 3.3).

3.4.9 Lineaments

Structural mapping of lineaments was performed on the northeastern, southwestern and western sections of the central uplift of Verlaine (Fig. 3.8), which correspond to the three localities with the best exposures of the MFB and thereby the highest density of lineaments. Lineaments range from ~50 to 550 m in length with thicknesses averaging ~3–5 m. A total of 305 lineaments were mapped and their orientations were measured from 0 to 180°. Mirrored rose diagrams (Figs. 3.9) reveal that lineaments occur in a radial and tangential orientations to the central uplift.

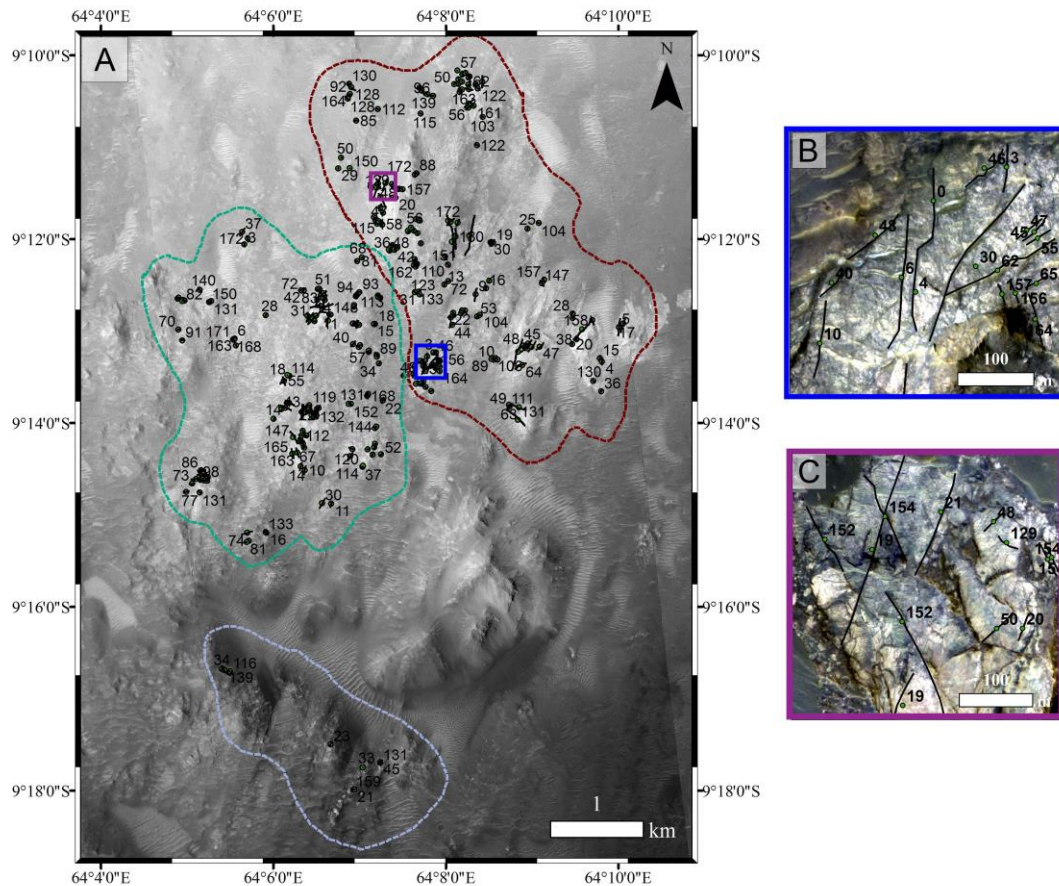


Figure 3.8. Structural mapping over HiRISE with rose diagrams for the southwestern, northwestern, and northeastern sections of the uplift showing orientations of lineaments cross-cutting the MFB. B: Window showing lineaments in the centre of the uplift with preferential south-north trend. C: Window in the

centre of the uplift showing lineaments with preferential southwest-northeast and southeast-northwest trends.

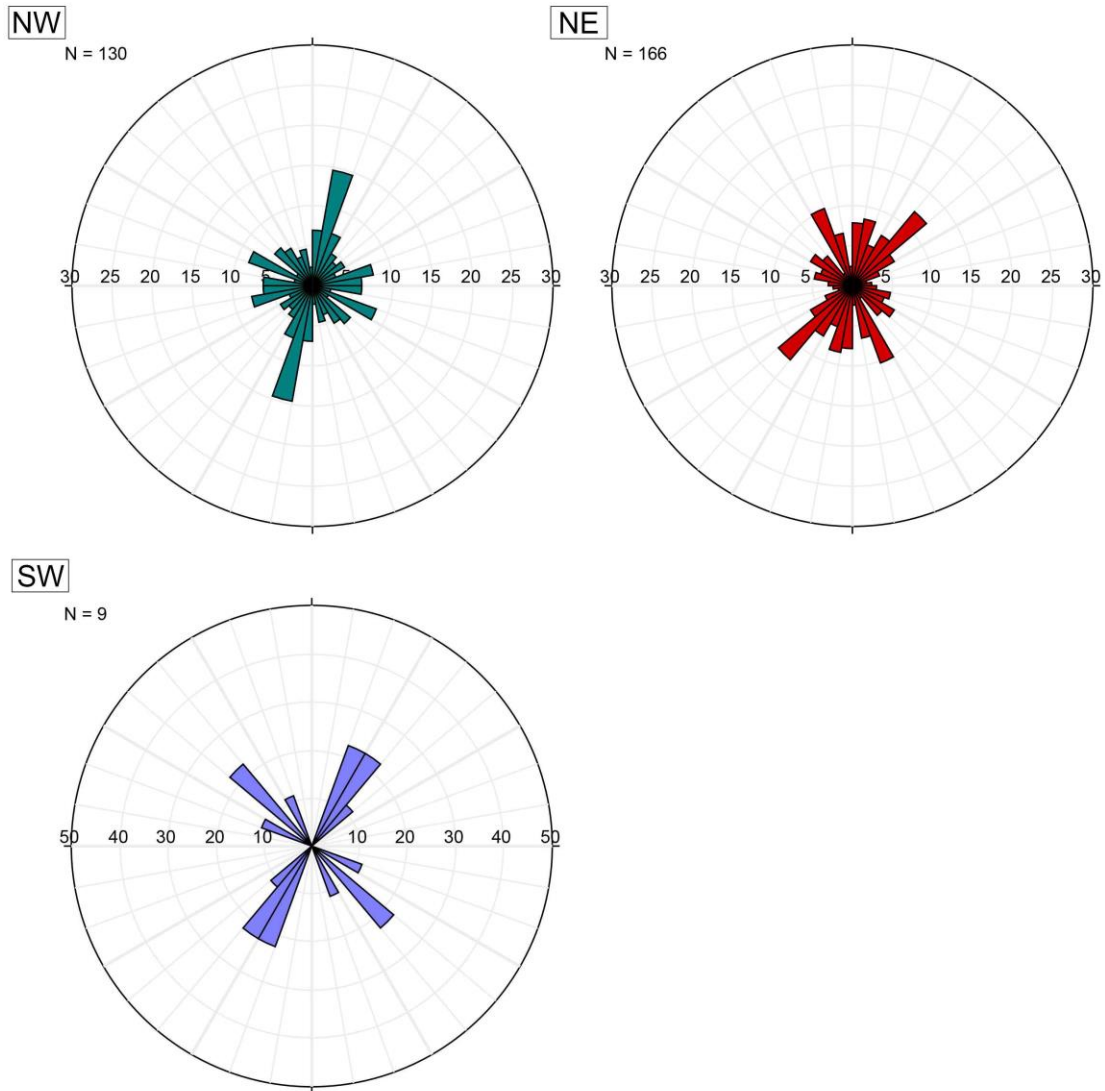


Figure 3.9. Stereonet rose diagrams of lineaments measured from 0 to 180 ° and mirrored in order to form a 360 ° plot for the southwestern, northwestern and northeastern sections of the central uplift of Verlaine Crater.

3.5 Discussion

3.5.1 Interpretation of morphological units

We have identified and described eight distinct morphological units: (1) massive and fractured bedrock (MFB); (2) brecciated unit; (3) dark-toned clast-rich unit; (4) dark-toned clast-poor unit; (5) medium-toned clast-poor unit; (6) dark-toned pit-bearing unit; (7) unconsolidated materials; and (8) aeolian deposits. We interpret and divide these morphological units into four categories: parautochthonous target rock, impact megabreccia, crater-fill impact melt-bearing deposits, and post-impact deposits.

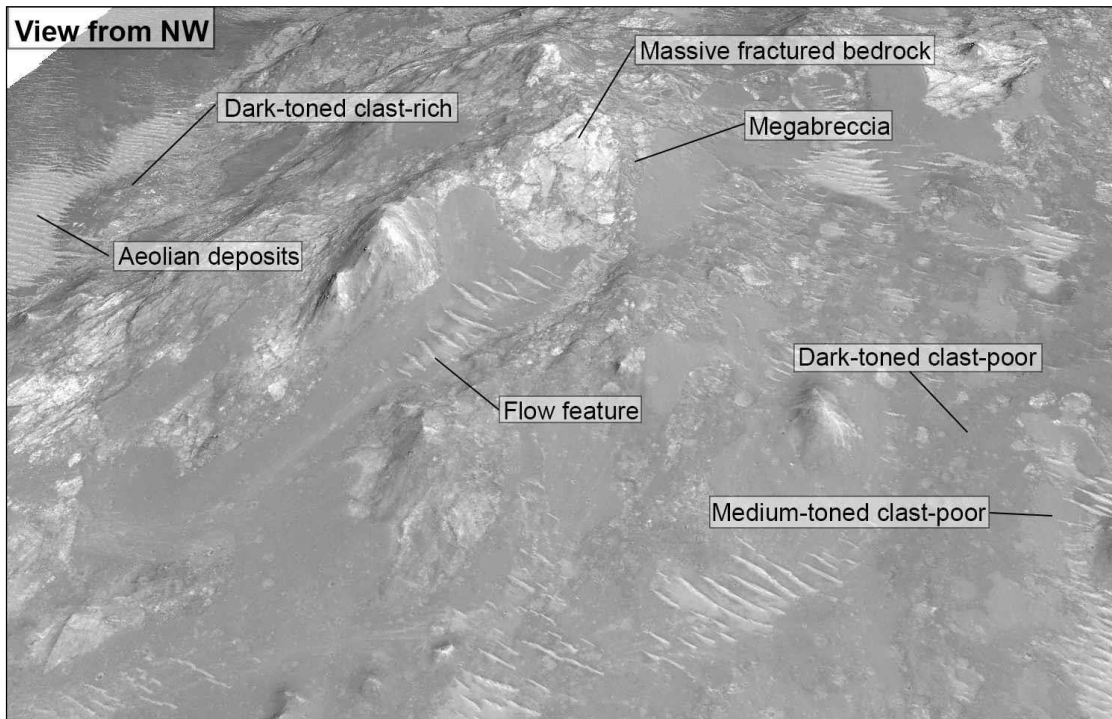


Figure 3.10. HiRISE RED perspective based on an orthorectified HiRISE ESP_013635_1705 on the HiRISE-derived DTM DTEED_013213_1705_013635_1705_A01. View from the north of the central uplift showing the morphological units.

3.5.1.1 Parautochthonous target rocks

The unit we mapped as massive and fractured bedrock (MFB) is interpreted as parautochthonous bedrock (i.e., pre-impact target rocks) that was uplifted by the Verlaine impact, and comprises ~19% of the uplift (Table 3.2). It is consistent with the massive and fractured bedrock (MFB) class documented by Tornabene et al. (2010, 2015) in ~124 Martian central uplifts, including Toro (Marzo et al., 2010) and Ritchey (Sun and Milliken, 2014; Ding et al., 2015) Craters. The MFB is draped (i.e., overlain) by units we interpret as allochthonous impactites (see below) (Fig. 3.10), although it is reasonable to assume that some outcrops of MFB were never coated by these deposits.

From the results of our spectral analysis, we suggest that the bedrock comprising the main bulk of the uplift is enriched in olivine. However, it appears to be pervasively altered throughout the uplift. We have identified a ~1.9 μm spectral feature indicative of bound H₂O water (Poulet et al., 2005; Mustard et al., 2008; Ehlmann et al., 2009) with the BD1900R parameter, and an additional ~2.31 μm feature with the D2300 parameter indicative of Fe- or Mg-OH absorption in Fe-Mg rich clays (Poulet et al., 2005; Mustard et al., 2007; Ehlmann et al., 2009; Ehlmann, 2010) (Fig. 3.7C). This could be an indication of alteration of olivine-bearing bedrock to Fe-Mg rich clays. Although we record the coupled ~1.9 μm hydration band and ~2.31 μm band, the 1.9 μm feature is sometimes weak, which could be explained by dehydration (Milliken and Mustard, 2005).

Overall, clear spectral signatures were difficult to isolate. This is partly due to the noisiness of the L-Sensor, or IR portion of the data that comes from the only targeted CRISM observation (i.e., FRT00012CD9) that covers Verlaine. The noisiness is likely due to the ongoing issues with the onboard coolers for the L-Sensor; this issue causes insufficient cooling resulting in CRISM to run under warmer conditions than normal, and thereby reduces the S/N of the IR data. At the time of writing this thesis, an additional targeted observation has been requested during the next CRISM “cold cycle” as the spectral nature of the Verlaine uplift certainly warrants further investigation.

3.5.1.2 Impact megabreccia

Megabreccia exposures correspond to poorly sorted, randomly oriented, fragmented angular to subrounded monomict and/or polymict breccias. They have mostly been detected from HiRISE imagery in the central uplift of relatively large craters (10's to 100's km diameter), and around the rims of the main impact basins (e.g., Argyre, Isidis, Hellas) (Grant et al., 2008; McEwen et al., 2009; Tornabene et al., 2009; L.L. Tornabene et al., 2013). Therein, it has commonly been referred as impact megabreccia.

Megabreccia is distinct from the impact breccias generally found on crater floors, such as those observed associated with crater-related pitted materials (Tornabene et al., 2012), in that it is composed of much larger blocks (>10 m) and is inferred to be indurated bedrock (McEwen et al., 2009), possibly of parautochthonous origin (e.g., Tornabene et al. (2010, 2015)).

However, there are several possible origins for the megabreccia unit: 1) fault breccias formed in the parautochthonous bedrock during the formation of the Verlaine central uplift; 2) crater-fill breccias at the base of the crater floor formed during the Verlaine impact; 3) pre-impact megabreccia formed during the Late Heavy Bombardment (LHB) by the Hellas impact basin (and likely with additional contributions from other impact craters/basins within the region) that was sampled by Verlaine.

Both preexisting and crater-formed breccias can occur in Martian craters (e.g., (Tornabene et al., 2010, 2015). In the central uplift of Toro Crater, Marzo et al. (2010) reported bedrock consistent with the MFB class, but that is cross-cut by dark interstitial materials, and which grades into a megabreccia facies (Fig. 3.11D). This is consistent with our observations in the central uplift of Verlaine, where outcrops of MFB cross-cut by darker-toned lineaments are contiguous to megabreccia. Ding et al. (2015) also recorded two types of megabreccia in the central uplift of Ritchey Crater; a pre-impact “buried megabreccia” with large clasts (up to a hundred metres) and a clast-rich deposit described as megabreccia with smaller clasts (metres to 10s of metres). Tornabene et al. (2009) also recorded megabreccia associated with Holden Crater, which they described as a non-chaotic distribution of megaclasts characterized by incipient brecciation from

breccia injection dykes (Fig. 3.11G); this suggested that the megabreccia was not of the preexisting type (i.e., pre-Holden), but formed during the Holden impact event.

We favor the formation of megabreccia during the Verlaine impact based on two distinct observations. First, megabreccia is likely polymict based on multiple coloured clasts observed in the HiRISE IRB image, which is consistent with colours associated to outcrops of MFB. Second, megabreccia always shares a sharp contact with the MFB and the dark-toned clast-poor unit (often underlying it) respectively, which suggests that it could be part of the parautochthonous bedrock of the uplift.

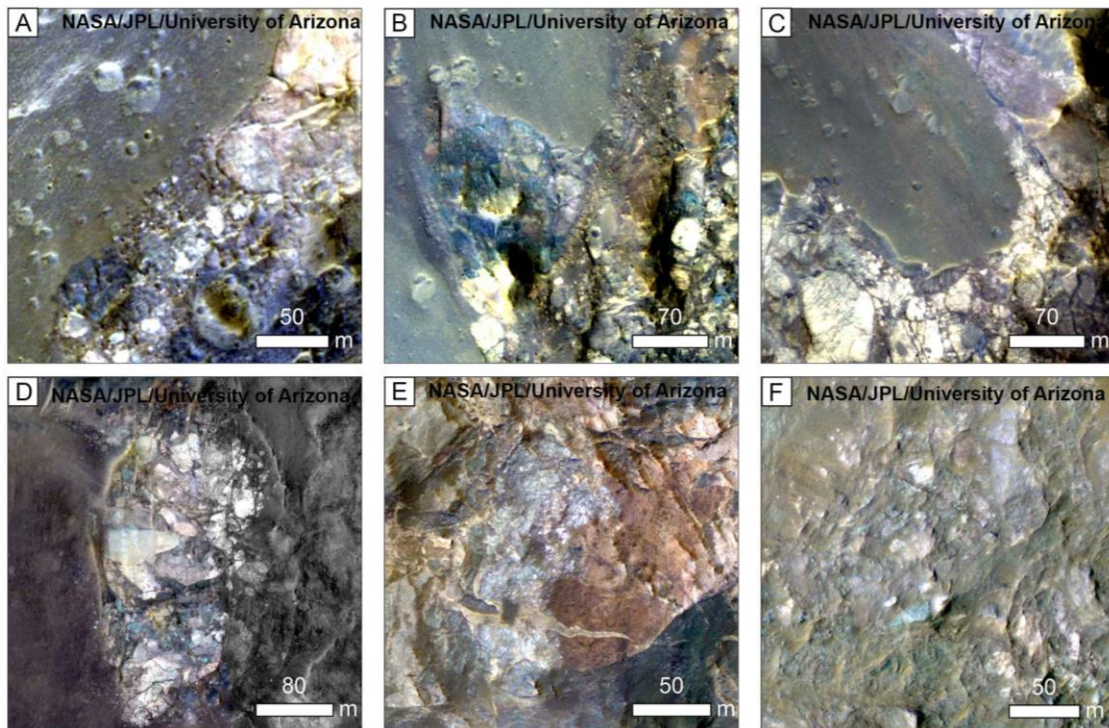


Figure 3.11. Megabreccia in the central uplifts of complex craters. A-C: Verlaine megabreccia. D: Toro megabreccia. E: Holden megabreccia. F: Ritchey megabreccia. Images credit: NASA/JPL/University of Arizona.

3.5.1.3 Allochthonous crater-fill impactites

Previous studies asserted that it would be improbable for coherent impact melt sheets to be generated within a volatile-rich target (Kieffer and Simonds, 1980), including on Mars. This is generally attributed to a lower gravity, lower impact velocities, and to a denser and more mafic crust (Schultz and Mustard, 2004; Pope et al., 2006). However, studies of terrestrial impact structures have demonstrated that impacts into sedimentary target rocks can result in considerable melting (Graup, 1999; Jones et al., 2000; Osinski and Spray, 2001, 2003; Dressler et al., 2004; Osinski et al., 2004, 2005b; Tuchscherer et al., 2004). Therein, the generation, dispersion and alteration of impact melt products in and around Martian impact structures have been reconsidered since. The recognition of crater-related pitted materials on Mars (Tornabene et al., 2012) and Vesta (Denevi et al., 2012) as a crater-formed volatile-rich impact melt-bearing deposits, which is likely equivalent to suevite (i.e., impact melt-bearing breccias), now supports that impact melting on Mars is more common than previously thought. Furthermore, morphological mapping and spectral analysis of complex craters have shown that a considerable proportion of the central uplift and crater floor are covered by impact melt-bearing deposits (Tornabene et al., 2010, 2015; Marzo et al., 2010; Osinski et al., 2011; Skok et al., 2012; Sun and Milliken, 2014; Ding et al., 2015; K.M. Cannon and Mustard, 2015; Nuhn et al., 2015). These deposits could potentially be used to assess past and current weathering rates, whereas their recognition is essential for future ground sampling (Schultz and Mustard, 2004; Sapers et al., 2015).

Based on clast content and tonality, we mapped three units (i.e., dark-toned clast-poor, medium-toned clast-poor and dark-toned clast-rich) that we interpret as impact melt rocks, and a fourth unit, the dark-toned pit-bearing unit, is interpreted as crater-related pitted materials. All together, these four units represent the impactite deposits formed by the Verlaine impact event. The dark-toned clast-poor unit, which covers the greatest area of the uplift (~27.2 %), is interpreted as a fine-grained melt unit that coated the exposed bedrock, megabreccia and lined the crater floor during the formation of the transient crater cavity. Flow features (Fig. 3.4F) associated with this unit as well as its stratigraphic (i.e., overlay) relationship to MFB and impact megabreccia support this

interpretation. The incorporation of cooler inclusions from the exposed bedrock and/or megabreccia would have produced the clast-rich facies of impact melt in some localities of the uplift, although we observe the dark-toned clast-poor unit to be directly grading to the clast-rich unit in very few localities. Indeed, the clast-rich unit covers a very small area of the uplift (~1.5 %) compared to Alga Crater (see Chapter 2), where it covers ~40% of the uplift. On the other hand, what we described as the medium-toned clast-poor unit covers a significant proportion of the uplift in Verlaine Crater (~13.2%) and is strictly observed in the northern section of the uplift on relatively gentle slopes and overlays the dark-toned clast-poor unit. It has an average thermal inertia in between the dark-toned clast-poor and clast-rich units ($\sim 323 \text{ J m}^{-2} \text{ K}^{-1} \text{ s}^{-1/2}$). We suggest that its intermediate tonality could be explained by a possible enrichment in very small light-toned clasts, although the resolution of HiRISE (~50 cm/pixel) does not allow to discern them.

Observations of both the Alga and Verlaine central uplifts reveal that the dark-toned clast-poor unit grades into the pit-bearing unit, which we interpret as crater-related pitted materials, and thereby the top-most portion of volatile-rich melt-bearing deposits in Verlaine (Boyce et al., 2012; Tornabene et al., 2012). Pitted materials in Verlaine Crater are better preserved than in Alga Crater (see Chapter 2). They cover a small area in the southern section of the uplift and completely surround the central uplift across the crater floor. They display subtle raised rims, lack proximal ejecta materials compared to secondary craters, and in some instances contain aeolian bedforms and/or light-toned clasts (Fig. 3.4H, 3.4I). This is consistent with observations of pitted materials by Tornabene et al. (2012) in other Martian uplifts, for which he provided the following two equations:

$$(1) D_{\text{mp}} = 27.5 D_{\text{c}}^{0.86}$$

$$(2) D_{\text{ap}} = 16.4 D_{\text{c}}^{0.87}$$

where D_{mp} is the maximum pit diameter (in metres), D_{ap} is the average pit diameter (in metres), and D_{c} is the host's crater diameter (in kilometres). Based on the diameter of

Verlaine, we find that $D_{ap}= 397$ m and $D_{mp}= 642$ m. Our largest pit diameter (~500 m) is just under the expected largest pit diameter from the scaling equations by Tornabene et al. (2012), but falls between the average and this upper limit. This result, along with the general occurrence, morphology and stratigraphic relationship that the pit-bearing unit possesses, corroborates our interpretation that the pit-bearing unit is consistent with the crater-related pitted materials, and thereby represents the top-most surface of the primary crater-fill deposits in Verlaine Crater.

3.5.1.4 Post-impact erosional deposits

As it can be also observed in Alga Crater (see Chapter 2), these deposits are recognized as post-impact erosional deposits. Unconsolidated and aeolian deposits represent the youngest and topmost morphological units in the central uplift of Verlaine Crater. Both units are important to recognize as they influence the exposure of each morphological units, and can affect thermal as well as spectral analysis (Tornabene et al., 2015).

Unconsolidated materials. This post-impact unit, which may also be a currently active process, is interpreted as weaker sediments of the regolith that got eroded away on the steepest slopes of the uplift under the influence of gravity. Some of the highest thermal inertia is recorded for this unit ($\sim 419 \text{ J m}^{-2} \text{ K}^{-1} \text{ s}^{-1/2}$), and we attribute it to the presence of light-toned clasts/boulders entrained during mass wasting events.

Aeolian deposits. This unit is interpreted as aeolian bedforms that formed as a result of aeolian saltation (fine sand) (Sullivan et al., 2005; Bridges et al., 2010). Relatively low thermal inertia values ($\sim 279 \text{ J m}^{-2} \text{ K}^{-1} \text{ s}^{-1/2}$) corroborate our interpretation of the unconsolidated and fine-grained nature of this unit (Ferguson et al., 2006). Both network and linear aeolian bedforms in the intra-crater area of Verlaine are the result of saltation. Network dunes are formed from the intersection of sand ridges as wind is blowing in multiple directions, whereas the linear dunes are formed from 1 or 2 opposing wind directions. Aeolian bedforms could have originated from the weathering of crater-related deposits or from regionally derived materials.

3.5.2 Structure of the central uplift

The results of the structural mapping indicate that lineaments are oriented radially and concentrically to the central uplift, which is consistent with the structural assessment of Alga Crater. A random distribution, including non-radial and non-tangential pattern of structural features would indicate a pre-impact origin. However, the distinct radial and tangential pattern of lineaments recorded for the central uplift of Verlaine Crater suggests an impact-generated origin for the structural features (Kenkmann, 2002; Kenkmann et al., 2014). The same has been concluded for the Haughton impact structure on Devon Island (Osinski and Spray, 2005) and for Ritchey Crater (Ding et al., 2015) on Mars.

Considering that Verlaine is located within what appears to be a degraded basin, it is possible that pre-existing structural patterns could have been disturbed and reoriented by the Verlaine impact.

3.5.3 Geology and mineralogy of the central uplift of Verlaine Crater

The regional geological context associated with Verlaine Crater is complex for a number of reasons. First, Verlaine Crater appears to be superposed on a larger degraded basin (Fig. 3.1B), and a 5-km crater is located northwest of its central uplift at the crater floor (Fig. 3.2B). On a more regional scale, Verlaine is bounded to the southwest by the Huygens Crater and is also in the vicinity of the ~2,300 km Hellas Basin (Fig. 3.1A), the largest preserved and clearly recognizable impact basin on Mars. Verlaine Crater could represent a mixed uplift, comprised of both massive and fractured bedrock (MFB) and megabrecciated bedrock (MBB). Some of that bedrock could represent pre-existing ejecta material originating from the Hellas Basin, of which the formation dates back to the Early Noachian period (Hartmann and Neukum, 2001). Alternatively, as previously discussed, the megabreccias may be Verlaine-formed.

The mineralogy of the central uplift of Verlaine Crater appears to be characterized by a mixture of olivine, low-calcium pyroxene (LCP) and high-calcium pyroxene (HCP), with alteration products interpreted as Fe/Mg-rich clays. The correlation between the ~1.9 μm and ~2.31 μm spectral absorption features with olivine-bearing MFB suggests that

alteration of primary mafic minerals (i.e., olivine) to secondary minerals (i.e., Fe/Mg-rich clays) occurred at some point during or prior to the Verlaine impact. Sun and Milliken (2014) had a similar conclusion for the Ritchey central uplift in which they concluded that "clay minerals are primarily associated with olivine-bearing materials in the exposed bedrock". Two scenarios are proposed for the origin of Fe/Mg-rich clays detected in the central uplift of Verlaine Crater.

3.5.3.1 Excavation of pre-existing materials by impact?

Outcrops of MFB exposed in the central uplift are interpreted as pre-impact target rocks representing the deepest materials of the target stratigraphy. From the observed correlation between Fe/Mg-rich clays and the exposed bedrock in the central uplift, one plausible interpretation is that the clays were formed prior to the Verlaine impact and then uplifted and excavated (Poulet et al., 2005; Bibring et al., 2006; Mustard et al., 2007, 2008; Ehlmann et al., 2009; Michalski and Niles, 2010; L.L. Tornabene et al., 2013; Osinski et al., 2013). For Fe/Mg-rich clays, we have to consider the thermal stability of phyllosilicates in relationship to shock-induced temperatures. Milliken and Mustard (2005) concluded that for pre-impact phyllosilicates to be associated with the floor, rim, wall, central uplift and ejecta blanket of impact craters, they should not be exposed to high enough temperatures (above 600 °C) for their spectral features to be altered. However, it can be very difficult to tell the difference between pre-impact and impact-induced (i.e., "syn-" impact) alteration in these crater settings (Tornabene et al., 2013). Fairén et al. (2010) suggested that phyllosilicates can be preexisting and minimally altered if found in occurrences with low-shock rocks of the central uplift. On the other hand, they found out that above temperatures of 800 °C, the IR spectra of phyllosilicates are subjected to significant modification. The central uplift of Toro Crater, a ~ 42 km complex crater, is thought to have been exposed to minimum temperatures near 650 to 800 °C. Given the size of Verlaine (~39 km) and using Toro Crater as a proxy, it is likely that pre-existing clays brought up in the uplift of Verlaine would have been preserved if minimum post-shock temperatures were near 650 °C or below (since Verlaine Crater is slightly smaller than Toro). If post-shock temperatures were closer to 800 °C, then it would be unlikely for pre-existing clays to be preserved. Nevertheless, it is entirely

plausible that the clays in the central uplift of Verlaine are pre-impact in origin, but they could have also been destroyed during the formation of the central uplift.

3.5.3.2 Impact-generated hydrothermal alteration?

A second scenario is an impact-generated origin for the Fe/Mg-rich clays in the central uplift of Verlaine Crater through impact-generated hydrothermal activity (Osinski et al., 2013) or other possible impact-induced pathways (Tornabene et al., 2013). Models suggest that post-impact hydrothermal circulation can be sustained for ~67,000 years for a Martian impact crater of ~30 km in diameter (Verlaine Crater is 39 km in diameter) (Abramov and Kring, 2005). Evidence for the impact-generated hydrothermal alteration hypothesis is supported by combined morphological and spectral observations from several craters on Mars. Hydrated materials within the crater-fill deposits of Toro Crater were observed to be only in portions of the crater-fill that are pervaded by light-toned fractures (see both Marzo et al., 2010 and Osinski et al., 2013). Additionally, small scale mounds (10s to 100s of metres in diameter) linked by light-toned fractures associated with the central uplift of Toro Crater (and possibly a few other craters on Mars (Osinski et al., 2013)) may represent putative hydrothermal mounds (Marzo et al., 2010). Furthermore, CRISM analysis by Marzo et al. (2010) revealed mineral assemblages such as prehnite-chlorite that are consistent with temperature and pressure conditions of hydrothermal environments. In Holden Crater, the strict occurrence of Fe/Mg phyllosilicates in breccia injection dykes also indicates a probable impact-generated origin for clays (Tornabene et al., 2009; L.L. Tornabene et al., 2013; Osinski et al., 2013). Lastly, Mangold et al. (2012b) suggested that fan deposits in Manjuro Crater formed rapidly coming into contact with the hot crater-related pitted materials on the crater floor (a heat and volatile-rich), which subsequently pervasively altered the fan deposits. Unfortunately, the central uplift of Verlaine appears to lack such detailed morphological observations associated with the spectral detection of hydrated minerals indicative of impact-induced alteration (i.e., light-toned fractures associated with hydration or injection dykes cross-cutting impactites, or morphological evidence of hydrothermal mounds). Therefore, there does not appear to be a strong case for the impact-generated scenario for the origin of Fe/Mg-rich clays in Verlaine. However, terrestrial analog studies indicate

that such evidence is very difficult to recognize even under the best observations, and so we do not rule out the possibility of an impact-generated scenario.

3.6 Conclusions

Detailed morphological and structural mapping combined with compositional analysis in addition to supplemental datasets (e.g., topography and thermal inertia data) have revealed that the central uplift of Verlainé is composed of high thermal inertia massive and fractured bedrock (MFB), which appears to be enriched in olivine. However, the bedrock is pervasively altered throughout the uplift. Some of the olivine-rich exposures of MFB have been altered to Fe/Mg-rich clays, which we suggest are possibly pre-impact in origin. The central uplift is also characterized by a diversity of allochthonous crater-fill impactites, which includes impact melt-bearing rocks (i.e., dark-toned clast-poor, medium-toned clast-poor, dark-toned clast-rich) and crater-related pitted materials. Almost two thirds of the central uplift is coated (i.e., overlain) by impact melt-bearing lithologies (~60%), while being embayed in crater-related pitted materials. Impact megabreccia is interpreted to be the result of brecciation by the Verlainé impact, but cannot be ruled out as pre-existing breccias contributed by nearby basins. In fact, the regional context at Verlainé Crater is complicated by the fact that it occurs within a larger degraded basin, while being located in the vicinity of the Hellas Basin. Furthermore, a 5-km crater is located northwest of the uplift on the crater floor. Structural mapping reveals that lineaments are oriented radially and concentrically to the central uplift, which is consistent with structural assessments at terrestrial complex craters (e.g., Haughton impact structure, Devon Island) and at Ritchey Crater on Mars. Finally, this study aims to demonstrate the importance of correlating morphological and structural observations to compositional information from spectral reflectance data in order to distinguish the origin (i.e., pre-, syn- and/or post-impact) of the deposits in Martian central uplifts.

3.7 References

- Abramov, O., Kring, D.A., 2005. Impact-induced hydrothermal activity on early Mars. *J. Geophys. Res.* 110, 1–19.
- Adams, J.B., 1974. Visible and near-infrared diffuse reflectance spectra of pyroxenes as applied to remote sensing of solid objects in the solar system. *J. Geophys. Res.* 79, 4829–4836.
- Bibring, J.-P., Langevin, Y., Mustard, J.F., Poulet, F., Arvidson, R.E., Gendrin, A., Gondet, B., Mangold, N., Pinet, P., Forget, F., Berthé, M., Gomez, C., Jouglet, D., Soufflot, A., Vincendon, M., Combes, M., Drossart, P., Encrenaz, T., Fouchet, T., Merchiorri, R., Belluci, G., Altieri, F., Formisano, V., Capaccioni, F., Cerroni, P., Coradini, A., Fonti, S., Korablev, O., Kottsov, V., Ignatiev, N., Moroz, V., Titov, D., Zasova, L., Loiseau, D., Pinet, P., Douté, S., Schmitt, B., Sotin, C., Hauber, E., Hoffmann, H., Jaumann, R., Keller, H.U., Arvidson, R.E., Duxbury, T.C., Forget, F., Neukum, G., Team, O., 2006. Global Mineralogical and Aqueous Mars History Derived from OMEGA/Mars Express Data. *Science*. 312, 400–404.
- Boyce, J.M., Wilson, L., Mouginiis-Mark, P.J., Hamilton, C.W., Tornabene, L.L., 2012. Origin of small pits in martian impact craters. *Icarus*. 221, 262–275.
- Bridges, N.T., Banks, M.E., Beyer, R. A., Chuang, F.C., Noe Dobrea, E.Z., Herkenhoff, K.E., Keszthelyi, L.P., Fishbaugh, K.E., McEwen, a. S., Michaels, T.I., Thomson, B.J., Wray, J.J., 2010. Aeolian bedforms, yardangs, and indurated surfaces in the Tharsis Montes as seen by the HiRISE Camera: Evidence for dust aggregates. *Icarus*. 205, 165–182.
- Cannon, K.M., Mustard, J.F., 2015. Preserved glass-rich impactites on Mars. *Geology*. 43, 635–638.
- Carter, J., Poulet, F., Bibring, J.-P., Murchie, S.L., 2010. Detection of hydrated silicates in crustal outcrops in the northern plains of Mars. *Science*. 328, 1682–1686.

- Caudill, C.M., Tornabene, L.L., McEwen, A.S., Byrne, S., Ojha, L., Mattson, S., 2012. Layered MegaBlocks in the central uplifts of impact craters. *Icarus*. 221, 710–720.
- Christensen, P.R., Jakosky, B.M., Kieffer, H.H., Malin, M.C., Mcdween, H.Y., Nealon, K., Mehall, G.L., Silverman, S.H., Ferry, S., Caplinger, M.A., Ravine, M.A., 2004. The thermal emission imaging system (THEMIS) for the Mars 2001 Odyssey mission. *Space Sci. Rev.* 110, 85–130.
- Clark, R.N., Swayze, G.A., Wise, R., Livo, K.E., Hoefen, T.M., Kokaly, R.F., Sutley, S.J., 2007. USGS digital spectral library splib06a.
- Denevi, B.W., Koeber, S.D., Robinson, M.S., Garry, W.B., Hawke, B.R., Tran, T.N., Lawrence, S.J., Keszthelyi, L.P., Barnouin, O.S., Ernst, C.M., Tornabene, L.L., 2012. Physical constraints on impact melt properties from Lunar Reconnaissance Orbiter Camera images. *Icarus*. 219, 665–675.
- Ding, N., Bray, V.J., McEwen, A.S., Mattson, S.S., Okubo, C.H., Chojnacki, M., Tornabene, L.L., 2015. The central uplift of Ritchey crater, Mars Ning Ding. *Icarus*. 252, 255–270.
- Dressler, B.O., Sharpton, V.L., Schwandt, C.S., Ames, D., 2004. Impactites of the Yaxcopoil-1 drilling site, Chicxulub impact structure: Petrography, geochemistry, and depositional environment. *Meteorit. Planet. Sci.* 39, 857–878.
- Ehlmann, B., Mustard, J.F., Swayze, G. A., Clark, R.N., Bishop, J.L., Poulet, F., Des Marais, D.J., Roach, L.H., Milliken, R.E., Wray, J.J., Barnouin-Jha, O., Murchie, S.L., 2009. Identification of hydrated silicate minerals on Mars using MRO-CRISM: Geologic context near Nili Fossae and implications for aqueous alteration. *J. Geophys. Res. E Planets*. 114, 1–33.
- Ehlmann, B.L., 2010. Diverse aqueous environments during Mars' first billion years: the emerging view from orbital visible-near infrared spectroscopy. *Geochemical News* 142, gn142.

- Ehlmann, B.L., Mustard, J.F., Murchie, S.L., Bibring, J.-P., Meunier, A., Fraeman, A.A., Langevin, Y., 2011. Subsurface water and clay mineral formation during the early history of Mars. *Nature*. 479, 53–60.
- Fairén, A.G., Chevrier, V., Abramov, O., Marzo, G.A., Gavin, P., Davila, A.F., Tornabene, L.L., Bishop, J.L., Roush, T.L., Gross, C., Kneissl, T., Uceda, E.R., Dohm, J.M., Schulze-Makuch, D., Rodríguez, J.A.P., Amils, R., McKay, C.P., 2010. Noachian and more recent phyllosilicates in impact craters on Mars. *Proc. Natl. Acad. Sci. U. S. A.* 107, 12095–12100.
- Ferguson, R.L., Christensen, P.R., Kieffer, H.H., 2006. High-resolution thermal inertia derived from the Thermal Emission Imaging System (THEMIS): Thermal model and applications. *J. Geophys. Res.* 111, 1–22.
- Grant, J.A., Irwin, R.P., Grotzinger, J.P., Milliken, R.E., Tornabene, L.L., McEwen, A.S., Weitz, C.M., Squyres, S.W., Glotch, T.D., Thomson, B.J., 2008. HiRISE imaging of impact megabreccia and sub-meter aqueous strata in Holden Crater, Mars. *Geology*. 36, 195.
- Graup, G., 1999. Carbonate-silicate liquid immiscibility upon impact melting: Ries Crater, Germany. *Meteorit. Planet. Sci.* 34, 425–438.
- Hartmann, W.K., Neukum, G., 2001. Cratering chronology and the evolution of Mars. *Space Sci. Rev.* 96, 165–194.
- Hynek, B.M., Beach, M., Hoke, M.R.T., 2010. Updated global map of Martian valley networks and implications for climate and hydrologic processes. *J. Geophys. Res.* 115, 1–14.
- Jones, A.P., Claeys, P., Heuschkel, S., 2000. Impact melting of carbonates from the Chicxulub Crater. *Lect. Notes Earth Sci.* 91, 343–361.
- Kenkmann, T., 2002. Folding within seconds. *Geology*. 30, 231–234.

- Kenkmann, T., Jahn, A., Scherler, D., Ivanov, B.A., 2005. Structure and formation of a central uplift: A case study at the Upheaval Dome impact crater, Utah. *Geol. Soc. Am. Spec. Pap.* 384, 85–115.
- Kenkmann, T., Poelchau, M.H., Wulf, G., 2014. Structural geology of impact craters. *J. Struct. Geol.* 62, 156–182.
- Kieffer, S.W., Simonds, C.H., 1980. The Role of Volatiles and Lithology in the Impact Cratering Process. *Rev. Geophys. Sp. Phys.* 18, 143–181.
- Malin, M.C., Bell, J.F., Cantor, B. A., Caplinger, M. A., Calvin, W.M., Clancy, R.T., Edgett, K.S., Edwards, L., Haberle, R.M., James, P.B., Lee, S.W., Ravine, M. a., Thomas, P.C., Wolff, M.J., 2007. Context Camera Investigation on board the Mars Reconnaissance Orbiter. *J. Geophys. Res.* 112, 1–25.
- Mangold, N., Adeli, S., Conway, S., Ansan, V., Langlais, B., 2012a. A chronology of early Mars climatic evolution from impact crater degradation. *J. Geophys. Res. Planets.* 117, 1–22.
- Mangold, N., Kite, E.S., Kleinhans, M.G., Newsom, H., Ansan, V., Hauber, E., Kraal, E., Quantin, C., Tanaka, K., 2012b. The origin and timing of fluvial activity at Eberswalde crater, Mars. *Icarus.* 220, 530–551.
- Marzo, G.A., Davila, A.F., Tornabene, L.L., Dohm, J.M., Fairén, A.G., Gross, C., Kneissl, T., Bishop, J.L., Roush, T.L., McKay, C.P., 2010. Evidence for Hesperian impact-induced hydrothermalism on Mars. *Icarus.* 208, 667–683.
- McEwen, A.S., Eliason, E.M., Bergstrom, J.W., Bridges, N.T., Hansen, C.J., Delamere, W.A., Grant, J.A., Gulick, V.C., Herkenhoff, K.E., Keszthelyi, L., Kirk, R.L., Mellon, M.T., Squyres, S.W., Thomas, N., Weitz, C.M., 2007. Mars Reconnaissance Orbiter's High Resolution Imaging Science Experiment (HiRISE). *J. Geophys. Res.* 112, 1–40.

- McEwen, A.S., Grant, J., Mustard, J., Wray, J., Tornabene, L.L., 2009. Early Noachian rocks in megabreccia deposits on Mars. EPSC Abstr. 4, 2.
- Michalski, J.R., Niles, P.B., 2010. Deep crustal carbonate rocks exposed by meteor impact on Mars. *Nat. Geosci.* 3, 751–755.
- Milliken, R.E., Mustard, J.F., 2005. Quantifying absolute water content of minerals using near-infrared reflectance spectroscopy. *J. Geophys. Res.* 110, 1–25.
- Murchie, S., Arvidson, R., Bedini, P., Beisser, K., Bibring, J.-P., Bishop, J., Boldt, J., Cavender, P., Choo, T., Clancy, R.T., Darlington, E.H., Des Marais, D., Espiritu, R., Fort, D., Green, R., Guinness, E., Hayes, J., Hash, C., Heffernan, K., Hemmler, J., Heyler, G., Humm, D., Hutcheson, J., Izenberg, N., Lee, R., Lees, J., Lohr, D., Malaret, E., Martin, T., McGovern, J. A., McGuire, P., Morris, R., Mustard, J., Pelkey, S., Rhodes, E., Robinson, M., Roush, T., Schaefer, E., Seagrave, G., Seelos, F., Silverglate, P., Slavney, S., Smith, M., Shyong, W.-J., Strohhahn, K., Taylor, H., Thompson, P., Tossman, B., Wirzburger, M., Wolff, M., 2007. Compact Reconnaissance Imaging Spectrometer for Mars (CRISM) on Mars Reconnaissance Orbiter (MRO). *J. Geophys. Res.* 112, 1–57.
- Murchie, S.L., Mustard, J.F., Ehlmann, B.L., Milliken, R.E., Bishop, J.L., McKeown, N.K., Noe Dobrea, E.Z., Seelos, F.P., Buczkowski, D.L., Wiseman, S.M., Arvidson, R.E., Wray, J.J., Swayze, G., Clark, R.N., Des Marais, D.J., McEwen, A.S., Bibring, J.-P., 2009a. A synthesis of Martian aqueous mineralogy after 1 Mars year of observations from the Mars Reconnaissance Orbiter. *J. Geophys. Res.* 114, 1–30.
- Murchie, S.L., Seelos, F.P., Hash, C.D., Humm, D.C., Malaret, E., McGovern, J.A., Choo, T.H., Seelos, K.D., Buczkowski, D.L., Morgan, M.F., Barnouin-Jha, O.S., Nair, H., Taylor, H.W., Patterson, G.W., Harvel, C. A., Mustard, J.F., Arvidson, R.E., McGuire, P., Smith, M.D., Wolff, M.J., Titus, T.N., Bibring, J.P., Poulet, F., 2009b. Compact Reconnaissance Imaging Spectrometer for Mars investigation and data set from the Mars Reconnaissance Orbiter's primary science phase. *J. Geophys. Res. E Planets.* 114, 1–15.

- Mustard, J.F., Murchie, S.L., Pelkey, S.M., Ehlmann, B.L., Milliken, R.E., Grant, J.A., Bibring, J.-P., Poulet, F., Bishop, J., Dobrea, E.N., Roach, L., Seelos, F., Arvidson, R.E., Wiseman, S., Green, R., Hash, C., Humm, D., Malaret, E., McGovern, J.A., Seelos, K., Clancy, T., Clark, R., Marais, D.D., Izenberg, N., Knudson, A., Langevin, Y., Martin, T., McGuire, P., Morris, R., Robinson, M., Roush, T., Smith, M., Swayze, G., Taylor, H., Titus, T., Wolff, M., 2008. Hydrated silicate minerals on Mars observed by the Mars Reconnaissance Orbiter CRISM instrument. *Nature*. 454, 305–309.
- Mustard, J.F., Poulet, F., Head, J.W., Mangold, N., Bibring, J.-P., Pelkey, S.M., Fassett, C.I., Langevin, Y., Neukum, G., 2007. Mineralogy of the Nili Fossae region with OMEGA/Mars Express data: 1. Ancient impact melt in the Isidis Basin and implications for the transition from the Noachian to Hesperian. *J. Geophys. Res.* 112, 1–14.
- Neukum, G., Jaumann, R., Team, H.C.-I. and E., 2004. HRSC : the High Resolution Stereo Camera of Mars Express. *Mars Express Sci. payload* 17–35.
- Nuhn, A.M., Tornabene, L.L., Osinski, G.R., McEwen, A.S., 2015. Morphologic and structural mapping of the central uplift of Betio crater, Thaumasia Planum, Mars. *Geol. Soc. Am. Spec. Pap.* 518, 65–83.
- Osinski, G.R., Grieve, R.A.F., Spray, J.G., 2004. The nature of the groundmass of surficial suevite from the Ries impact structure, Germany, and constraints on its origin. *Meteorit. Planet. Sci.* 39, 1655–1683.
- Osinski, G.R., Spray, J.G., 2001. Impact-generated carbonate melts: evidence from the Haughton structure, Canada. *Earth Planet. Sci. Lett.* 194, 17–29.
- Osinski, G.R., Spray, J.G., 2003. Evidence for the shock melting of sulfates from the Haughton impact structure, Arctic Canada. *Earth Planet. Sci. Lett.* 215, 357–370.

- Osinski, G.R., Spray, J.G., 2005. Tectonics of complex crater formation as revealed by the Haughton impact structure, Devon Island, Canadian High Arctic. *Meteorit. Planet. Sci.* 40, 1789–1812.
- Osinski, G.R., Spray, J.G., Lee, P., 2005. Impactites of the Haughton impact structure, Devon Island, Canadian High Arctic. *Meteorit. Planet. Sci.* 40, 1789–1812.
- Osinski, G.R., Tornabene, L.L., Banerjee, N.R., Cockell, C.S., Flemming, R., Izawa, R.M., McCutcheon, J., Parnell, J., Preston, L.J., Pickersgill, A.E., Pontefract, A., Sapers, H.M., Southam, G., 2013. Impact-generated hydrothermal systems on Earth and Mars. *Icarus.* 224, 347–363.
- Osinski, G.R., Tornabene, L.L., Grieve, R.A.F., 2011. Impact ejecta emplacement on terrestrial planets. *Earth Planet. Sci. Lett.* 310, 167–181.
- Pelkey, S.M., Mustard, J.F., Murchie, S., Clancy, R.T., Wolff, M., Smith, M., Milliken, R.E., Bibring, J.-P., Gendrin, A., Poulet, F., Langevin, Y., Gondet, B., 2007. CRISM multispectral summary products: Parameterizing mineral diversity on Mars from reflectance. *J. Geophys. Res. E Planets.* 112, 1–18.
- Pope, K.O., Kieffer, S.W., Ames, D.E., 2006. Impact melt sheet formation on Mars and its implication for hydrothermal systems and exobiology. *Icarus.* 183, 1–9.
- Poulet, F., Bibring, J.-P., Mustard, J.F., Gendrin, A., Mangold, N., Langevin, Y., Arvidson, R.E., Gondet, B., Gomez, C., Berthé, M., Erard, S., Forni, O., Manaud, N., Poulleau, G., Soufflot, A., Combes, M., Drossart, P., Encrenaz, T., Fouchet, T., Melchiorri, R., Bellucci, G., Altieri, F., Formisano, V., Fonti, S., Capaccioni, F., Cerroni, P., Coradini, A., Korablev, O., Kottsov, V., Ignatiev, N., Titov, D., Zasova, L., Pinet, P., Schmitt, B., Sotin, C., Hauber, E., Hoffmann, H., Jaumann, R., Keller, H.U., Forget, F., 2005. Phyllosilicates on Mars and implications for early martian climate. *Nature.* 438, 623–627.

- Quantin, C., Flahaut, J., Clenet, H., Allemand, P., Thomas, P., 2012. Composition and structures of the subsurface in the vicinity of Valles Marineris as revealed by central uplifts of impact craters. *Icarus*. 221, 436–452.
- Sapers, H.M., Banerjee, N.R., Osinski, G.R., 2015. Potential for impact glass to preserve microbial metabolism. *Earth Planet. Sci. Lett.* 430, 95–104.
- Schultz, P.H., Mustard, J.F., 2004. Impact melts and glasses on Mars. *J. Geophys. Res.* 109, 1–23.
- Skok, J.R., Mustard, J.F., Tornabene, L.L., Pan, C., Rogers, D.A., Murchie, S.L., 2012. A spectroscopic analysis of Martian crater central peaks: Formation of the ancient crust. *J. Geophys. Res.* 117, 1–33.
- Sullivan, R.J., Banfield, D., Bell, J.F., Calvin, W.M., Fike, D. a, Golombek, M.P., Greeley, R., Grotzinger, J.P., Herkenhoff, K.E., Jerolmack, D., Malin, M.C., Ming, D.W., Soderblom, L.A, Squyres, S.W., Thompson, S., Watters, W. A., Weitz, C.M., Yen, a, 2005. Aeolian processes at the Mars Exploration Rover Meridiani Planum landing site. *Nature*. 436, 58–61.
- Sun, V.Z., Milliken, R.E., 2014. The geology and mineralogy of Ritchey crater, Mars: Evidence for post-Noachian clay formation. *J. Geophys. Res. Planets.* 119, 810–836.
- Tanaka, K.L., Robbins, S.J., Fortezzo, C.M., Skinner, J.A., Hare, T.M., 2014. The digital global geologic map of Mars: Chronostratigraphic ages, topographic and crater morphologic characteristics, and updated resurfacing history. *Planet. Space Sci.* 95, 11–24.
- Tornabene, L., Osinski, G.R., Barlow, N.G., Bray, V.J., Caudill, C.M., D'Aoust, B., Ding, N., Hopkins, R., Nuhn, A.M., Mayne, A., Mcewen, A.S., 2015. Meter- to decameter-scale characteristics of central uplifts revealed by the Mars Reconnaissance Orbiter. *Bridg. Gap III* 5–6.

- Tornabene, L.L., McEwen, A.S., Caudill, C., Osinski, G.R., Wray, J.J., Marzo, G.A., Mustard, J.F., Skok, J.R., 2010. A Crater-Exposed Bedrock Database for Mars With Applications for Determining the Composition and Structure of the Upper Crust. in: 41st Lunar Planet. Sci. Conf. Abstract #1737.
- Tornabene, L.L., Osinski, G.R., McEwen, A.S., Boyce, J.M., Bray, V.J., Caudill, C.M., Grant, J.A., Hamilton, C.W., Mattson, S.S., Mouginis-Mark, P.J., 2012. Widespread crater-related pitted materials on Mars: Further evidence for the role of target volatiles during the impact process. *Icarus*. 220, 348–368.
- Tornabene, L.L., Osinski, G.R., McEwen, A.S., Wray, J.J., Craig, M.A., Sapers, H.M., Christensen, P.R., 2013. An impact origin for hydrated silicates on Mars: A synthesis. *J. Geophys. Res. Planets*. 118, 994–1012.
- Tornabene, L.L., Osinski, G.R., McEwen, S., 2009. Parautochthonous megabreccias and possible evidence of impact-induced hydrothermal alteration in Holden Crater, Mars. in: 40th Lunar Planet. Sci. Conf. Abstract # 1766.
- Tuchscherer, M.G., Reimold, W.U., Koeberl, C., Gibson, R.L., Bruin, D., 2004. First petrographic results on impactites from the Yaxcopoil-1 borehole, Chicxulub structure, Mexico. *Meteorit. Planet. Sci.* 39, 899–930.
- Wray, J.J., Ehlmann, B.L., Squyres, S.W., Mustard, J.F., Kirk, R.L., 2008. Compositional stratigraphy of clay-bearing layered deposits at Mawrth Vallis, Mars. *Geophys. Res. Lett.* 35, 1–6.
- Zuber, M.T., Smith, D.E., Solomon, S.C., Muhleman, D.O., Head, J.W., Garvin, J.B., Abshire, J.B., Bufton, J.L., 1992. The Mars Observer Laser Altimeter Investigation. *J. Geophys. Res.* 97, 7781–7797.

Chapter 4

4 Final discussion and conclusions

4.1 Review

The formation of central uplifts remains a poorly understood process on Earth and other planetary bodies. The main objective of this thesis was to conduct detailed morphological and structural mapping as well as compositional analysis of the central uplifts of Martian complex craters. We used Mars Reconnaissance Orbiter (MRO) High Resolution Imaging Science Experiment (HiRISE) (McEwen et al., 2007), Context Camera (CTX) (Malin et al., 2007) and Compact Reconnaissance Spectrometer for Mars (CRISM) (Murchie et al., 2007) datasets, supplemented by topography data from Mars Orbiter Laser Altimeter (MOLA) (Smith et al., 2001) and thermal inertia data derived from the Thermal Emission Imaging System (THEMIS) (Christensen et al., 2004; Fergason et al., 2006). Two craters located within Noachian-aged terrains were selected: Alga (333.3 °E, 24.3 °S), a ~19 km diameter crater located within Noachis Terra southeast of Valles Marineris, and just north of Argyre Planitia; and Verlaine (64.1 °E, -9.2 °S), a ~39 km diameter crater bordered by Terra Sabae and Tyrhenna Terra just north of Hellas Planitia. These craters were selected based on the fact that their central uplifts are mainly comprised of the massive and fractured bedrock (MFB) textural class initially defined by Tornabene et al. (2010) and catalogued in 124 of 200 complex craters on Mars (Tornabene et al., 2015).

The central uplift of Alga is characterized by olivine-bearing and low-calcium pyroxene (LCP)-bearing outcrops of MFB. The olivine-bearing MFB corresponds to the best-exposed and most coherent MFB with the highest thermal inertia, and is constrained to the northern and northwestern sections of the central uplift. The remaining bulk of the uplift is characterized by lower thermal inertia LCP-bearing MFB. The central uplift of Verlaine is comprised of both the MFB and megabrecciated bedrock (MBB) textural classes that exhibit the highest thermal inertia. The MFB in Verlaine appears to be enriched in olivine, although it is pervasively altered throughout the uplift. Additional

spectral analysis will be conducted when we will have acquired a targeted observation from the upcoming CRISM “cold cycle”. While Alga Crater is strictly characterized by an unaltered mafic mineralogy, secondary alteration phases interpreted as Fe/Mg-rich clays correlate with olivine-bearing MFB in the central uplift of Verlaine Crater and are consistent with pre-impact uplifted and excavated hydrated silicates, similarly to observations at Ritchey Crater by Sun and Milliken (2014). Structural analysis of both central uplifts revealed that lineaments are oriented radially and concentrically to the uplift, which is equivalent to structural assessments of terrestrial complex structures such as the Haughton impact structure on Devon Island (Osinski and Spray, 2005) and Ritchey Crater on Mars (Ding et al., 2015).

A very important outcome of this study is that both central uplifts are overlain by a significant proportion of impact melt-bearing lithologies of varying tonality (dark, medium and light-toned) and clast content (clast-poor and clast-rich), and are embayed in crater-related pitted materials (Tornabene et al., 2012). Approximately three quarters (or ~73%) of the central uplift of Alga is coated (i.e., overlain) by impact melt-bearing lithologies and close to two thirds (or ~60%) of the central uplift of Verlaine is covered by these deposits. In Alga Crater, we observe the dark-toned clast-rich melt to be directly grading into the clast-rich melt, which we suggest is a result of the incorporation of lithic clasts from the underlying bedrock as impact melt flowed downward towards the crater floor. In Verlaine Crater, this grading relationship is rare, but we record a contiguous relationship between dark-toned clast-poor and medium-toned clast-poor impact melt rocks. Sometimes, the medium-toned clast-poor melt is observed to be overlying the darker-toned melt, and is suggested to possess a lighter tonality due to an enrichment in clasts, although not discernable at the resolution of HiRISE (~50 cm/pixel for Verlaine).

The origin of the bedrock exposed in the central uplift of Alga Crater is complicated by the fact that it is located within Chekalin Crater, which in turn is located in the vicinity of Ladon Basin, and on a greater scale in the vicinity of Argyre Planitia. On the other hand, Verlaine Crater is located within a large (~200-km scale) degraded impact basin and within the vicinity of the Huygens peak-ring basin and the Hellas Basin. The results of

our morphological, structural, and spectral mapping indicate that olivine-rich and low-calcium pyroxene-rich bedrock in Alga Crater is consistent with other studies of Martian central uplifts around Argyre Planitia (Skok et al., 2012; Pan et al., 2015). Furthermore, we suggest that Alga Crater strictly uplifted the central uplift of Chekalin Crater based on its relative position in the centre of Chekalin, and the absence of layered rocks in the crater walls and terraces. In Verlaine Crater, we observed impact megabreccia that is very similar to megabreccia observed in the central uplift of Toro Crater (Marzo et al., 2010), and we suggested that it is was formed by the Verlaine impact event.

In conclusion, this study demonstrates the importance of correlating morphological and structural observations with compositional analysis, and care is needed when interpreting intra-crater deposits. Our results indicate that central uplifts of Martian complex craters correlate with previous studies of uplifts in the surrounding regions, that they expose mafic-rich deep-seated bedrock, and that they correlate well with results of global surface mapping.

4.2 Limitations of remotely-based geological mapping

Remotely-based geological mapping presents many limitations. First of all, it is not a possibility at the moment to conduct ground truth studies in order to confirm many of the hypotheses presented in this study. Indeed, the morphology of impact craters makes them challenging planetary bodies to explore. Second, many assumptions had to be made throughout the research (e.g., nature of the pre-impact target lithology, depth of subsurface geology) and some equations that have been tested only for Earth have been used. Third, orbital datasets represent another major limitation. For instance, HiRISE provides imagery with resolution ranging from ~25 cm/pixel to ~50 cm/pixel, and this can be limiting especially in the context of assessing the clast content of impact melt rocks. On the other hand, HiRISE colour imagery only covers ~20% of the HiRISE full swath of the image. For compositional analysis, CRISM spectral data were available for the central uplift of Alga Crater and for some regions of the rims, but CRISM data were only available for the central uplift of Verlaine Crater.

4.3 Future work

Since most detailed mapping studies have been conducted for impact craters located in the southern heavily cratered highlands, we suggest that a new study should select a crater situated in the northern lowlands of Mars. In fact, two localities, one in Chryse Planitia and the other in Acidalia Planitia, have all together 13 well-exposed central uplifts recorded in the database compiled by Tornabene et al. (2010) that possess the massive and fractured textural type of bedrock. One approach could be to select one crater of similar size to Alga or Verlaine for mapping and comparison.

4.4 References

- Christensen, P.R., Jakosky, B.M., Kieffer, H.H., Malin, M.C., Mcsween, H.Y., Neelson, K., Mehall, G.L., Silverman, S.H., Ferry, S., Caplinger, M.A., Ravine, M.A., 2004. The thermal emission imaging system (THEMIS) for the Mars 2001 Odyssey mission. *Space Sci. Rev.* 110, 85–130.
- Ding, N., Bray, V.J., Mcewen, A.S., Mattson, S.S., Okubo, C.H., Chojnacki, M., Tornabene, L.L., 2015. The central uplift of Ritchey crater, Mars Ning Ding. *Icarus.* 252, 255–270.
- Ferguson, R.L., Christensen, P.R., Kieffer, H.H., 2006. High-resolution thermal inertia derived from the Thermal Emission Imaging System (THEMIS): Thermal model and applications. *J. Geophys. Res.* 111, 1–22.
- Malin, M.C., Bell, J.F., Cantor, B.A., Caplinger, M.A., Calvin, W.M., Clancy, R.T., Edgett, K.S., Edwards, L., Haberle, R.M., James, P.B., Lee, S.W., Ravine, M.A., Thomas, P.C., Wolff, M.J., 2007. Context Camera Investigation on board the Mars Reconnaissance Orbiter. *J. Geophys. Res.* 112, 1–25.
- Marzo, G.A., Davila, A.F., Tornabene, L.L., Dohm, J.M., Fairén, A.G., Gross, C., Kneissl, T., Bishop, J.L., Roush, T.L., McKay, C.P., 2010. Evidence for Hesperian impact-induced hydrothermalism on Mars. *Icarus.* 208, 667–683.
- McEwen, A.S., Eliason, E.M., Bergstrom, J.W., Bridges, N.T., Hansen, C.J., Delamere, W.A., Grant, J.A., Gulick, V.C., Herkenhoff, K.E., Keszthelyi, L., Kirk, R.L., Mellon, M.T., Squyres, S.W., Thomas, N., Weitz, C.M., 2007. Mars Reconnaissance Orbiter's High Resolution Imaging Science Experiment (HiRISE). *J. Geophys. Res.* 112, 1–40.
- Murchie, S., Arvidson, R., Bedini, P., Beisser, K., Bibring, J.-P., Bishop, J., Boldt, J., Cavender, P., Choo, T., Clancy, R.T., Darlington, E.H., Des Marais, D., Espiritu, R., Fort, D., Green, R., Guinness, E., Hayes, J., Hash, C., Heffernan, K., Hemmler, J., Heyler, G., Humm, D., Hutcheson, J., Izenberg, N., Lee, R., Lees, J., Lohr, D.,

- Malaret, E., Martin, T., McGovern, J.A., McGuire, P., Morris, R., Mustard, J., Pelkey, S., Rhodes, E., Robinson, M., Roush, T., Schaefer, E., Seagrave, G., Seelos, F., Silverglate, P., Slavney, S., Smith, M., Shyong, W.-J., Strohbehn, K., Taylor, H., Thompson, P., Tossman, B., Wirzburger, M., Wolff, M., 2007. Compact Reconnaissance Imaging Spectrometer for Mars (CRISM) on Mars Reconnaissance Orbiter (MRO). *J. Geophys. Res.* 112, 1–57.
- Osinski, G.R., Spray, J.G., 2005. Tectonics of complex crater formation as revealed by the Haughton impact structure, Devon Island, Canadian High Arctic. *Meteorit. Planet. Sci.* 40, 1789–1812.
- Pan, C., Rogers, A.D., Michalski, J.R., 2015. Thermal and near-infrared analyses of central peaks of Martian impact craters: Evidence for a heterogeneous Martian crust. *J. Geophys. Res.* 120, 662–688.
- Skok, J.R., Mustard, J.F., Tornabene, L.L., Pan, C., Rogers, D.A., Murchie, S.L., 2012. A spectroscopic analysis of Martian crater central peaks: Formation of the ancient crust. *J. Geophys. Res.* 117, 1–33.
- Smith, D.E., Zuber, M.T., Frey, H.V., Garvin, J.B., Head, J.W., Muhleman, D.O., Pettengill, G.H., Phillips, R.J., Solomon, S.C., Zwally, H.J., Banerdt, W.B., Duxbury, T.C., Golombek, M.P., Lemoine, F.G., Neumann, G.A., Rowlands, D.D., Aharonson, O., Ford, P.G., Ivanov, A.B., Johnson, C.L., McGovern, P.J., Abshire, J.B., Afzal, R.S., Sun, X., 2001. Mars Orbiter Laser Altimeter: Experiment summary after the first year of global mapping of Mars. *J. Geophys. Res.* 106, 23,689–23,722.
- Sun, V.Z., Milliken, R.E., 2014. The geology and mineralogy of Ritchey crater, Mars: Evidence for post-Noachian clay formation. *J. Geophys. Res. Planets* 119, 810–836.
- Tornabene, L., Osinski, G.R., Barlow, N.G., Bray, V.J., Caudill, C.M., D’Aoust, B., Ding, N., Hopkins, R., Nuhn, A.M., Mayne, A., Mcewen, A.S., 2015. Meter- to decameter-scale characteristics of central uplifts revealed by the Mars Reconnaissance Orbiter. *Bridg. Gap III* 5–6.

- Tornabene, L.L., McEwen, A.S., Caudill, C., Osinski, G.R., Wray, J.J., Marzo, G.A., Mustard, J.F., Skok, J.R., 2010. A Crater-Exposed Bedrock Database for Mars With Applications for Determining the Composition and Structure of the Upper Crust. in 41st Lunar Planet. Sci. Conf. Abstract #1737.
- Tornabene, L.L., Osinski, G.R., McEwen, A.S., Boyce, J.M., Bray, V.J., Caudill, C.M., Grant, J.A., Hamilton, C.W., Mattson, S.S., Mougins-Mark, P.J., 2012. Widespread crater-related pitted materials on Mars: Further evidence for the role of target volatiles during the impact process. *Icarus*. 220, 348–368.

Curriculum Vitae

Name: Bianca D'Aoust

Post-secondary Education and Degrees: University of Ottawa
Ottawa, Ontario, Canada
2009-2013 B.Sc.

The University of Western Ontario
London, Ontario, Canada
2014-2016 M.Sc.

Honours and Awards: Richard J. Schmeelk Canada Fellowship
2014-2015

The Professional Institute of the Public Service of Canada
Paré Scholarship in Technology Studies
First year undergraduate
2009

Johnson Inc.
First year undergraduate
2009

Miller Thomson Foundation
First year undergraduate
2009

Bourse de la Francophonie
First year undergraduate
2009

Renewable Admission Scholarship, University of Ottawa
First year undergraduate
2009

President's Scholarship finalist, 1st year, University of Ottawa
First year undergraduate
2009

**Related Work
Experience**

Teaching Assistant
The University of Western Ontario
2014

Web content specialist
Canadian Geodetic Survey (CGS), NRCan
2013-2014

GEM (Geo-mapping for Energy and Minerals) knowledge
management data support specialist
Geological Survey of Canada (GSC), NRCan
2011-2013

Publications (conference abstracts):

D'Aoust, B., Tornabene, L.L., Osinski, G.R., McEwen, A.S. (2014). Morphological, structural and spectral mapping of the central uplift of Alga crater. LPSC XXXXVI, abstract (#2237).

D'Aoust, B., Tornabene, L.L., Osinski, G.R., McEwen, A.S. (2014). Morphological and structural mapping of massive-fractured bedrock in crater central uplifts on Mars. Eight International Conference on Mars, abstract (#1351).

Co-author

Peterson, T.D., Scott, J.M.J., Lecheminant, A.N., Chorlton, L.B., D'Aoust, B.M.A. (2014). Geology, Tebesjuak Lake, Nunavut. Geological Survey of Canada, Canadian Geoscience Map 158, (ed. prelim.), 1 sheet, doi:10.4095/293892.

Tornabene, L.L., Osinski, G.R., McEwen, A.S., Ling, V., Caudill, C.M., Nuhn, A., Hopkins, R., D'Aoust, B., Kasmai, B., Mattson, S. (2014). A global synthesis of the meter- to decameter-scale morphology and structure of complex crater central uplifts. Eight International Conference on Mars, abstract (#1379).